Achieving High Accuracy with Low Cost: Successful Applications of Auxiliary Field Quantum Monte Carlo to Weakly-Bound Molecules and Strongly Correlated Materials

by

Hongxia Hao

B.Sc., Jilin University, Changchun, P. R. China, 2014

M.Sc., Brown University, Providence, RI, 2016

A dissertation submitted in partial fulfillment of the
requirements for the degree of Doctor of Philosophy
in Department of Chemistry at Brown University

PROVIDENCE, RHODE ISLAND

October 2019

This dissertation by Hongxia Hao is accepted in its present form
by Department of Chemistry as satisfying the
dissertation requirement for the degree of Doctor of Philosophy.

Date_____ _____

Brenda M. Rubenstein, Ph.D., Advisor

Recommended to the Graduate Council

Date_____ _____

Brad Marston, Ph.D., Reader

Date_____ _____

Andrew Peterson, Ph.D., Reader

Approved by the Graduate Council

Date_____ _____

Andrew G. Campbell, Dean of the Graduate School

Vita

Education

- Ph.D. Department of Chemistry, Brown University, expected 2019. Advisor: Prof. Brenda M. Rubenstein
- M.S. Department of Chemistry, Brown University, 2016. Advisor: Prof. Christoph G. Rose-Petruck
- B.S. Department of Chemistry, Jilin University, Changchun, China, 2014. Advisor: Prof. Hao Zhang

Publications

1. **Hongxia Hao**, Antoine Georges, Andrew Millis, Brenda M. Rubenstein, Qiang Han, and Hao Shi*. (2019) Metal-insulator and magnetic phase transitions of Ca_2RuO_4 as revealed by auxiliary field quantum Monte Carlo and dynamical mean field theory in the zero-temperature limit. *To be submitted to Phys. Rev. Lett.*
2. **Hongxia Hao**, Brenda M. Rubenstein and Hao Shi*. (2019) Auxiliary field quantum Monte Carlo for multiband Hubbard models: Controlling the sign and phase problems to capture Hund's physics. *Phys. Rev. B* 99, 235142.
3. **Hongxia Hao**, James Shee, Shiv Upadhyay, Can Ataca, Kenneth D. Jordan and Brenda M. Rubenstein*. (2018) Accurate predictions of electron binding energies of dipole-bound anions via quantum Monte Carlo methods. *J. Phys. Chem. Lett.* 9, 6185.
4. Jeongnim Kim, ...**Hongxia Hao**...*et al* (2018). QMCPACK: an open source ab initio quantum Monte Carlo package for the electronic structure of atoms,

molecules and solids. *J. Phys. Condens. Matter* 30, 195901.

5. Tingting Li, Huanhuan Li, Zhennan Wu, **Hongxia Hao**, Jiale Liu, Tingting Huang, Haizhu Sun, Jingping Zhang, Hao Zhang* and Zuoxing Guo* (2015). Colloidal synthesis of greigite nanoplates with controlled lateral size for electrochemical applications. *Naonoscale* 7, 4147-4148.

6. Xiaohang Du, Zhaolai Chen, Zibo Li, **Hongxia Hao**, Chunwei Dong, Qingsen Zeng and Bai Yang* (2014). Dip-coated gold nanoparticles electrode for aqueous-solution-processed large-area solar cells. *Adv. Energy Mater.* 4, 1400135.

7. Yu Sheng, Min Lin, Xiangwei Li, **Hongxia Hao**, Xiaoying Lin, Hongchen Sun and Hao Zhang* (2014). Enhancement of the 808nm photothermal effect of gold nanorods by thiol-induced self-assembly. *Part. Part. Syst. Charact.* 31, 788-793.

8. Zhennan Wu, Chunwei Dong, Yanchun Li, **Hongxia Hao**, Hao Zhang*, Zhongyuan Lu* and Bai Yang (2013). Self-assembly of Au_{15} into single-cluster-thick sheets at the interface of two miscible high-boiling solvents. *Angew. Chem. Int. Ed.* 52, 9952-9955.

Teaching Experience

- Head Teaching Assistant for Equilibrium, Rate, and Structure lab (CHEM0330). Fall 2016

- Teaching Assistant for Equilibrium, Rate, and Structure lab (CHEM0330). Fall 2014 - Spring 2016

Conferences and Presentations

- Gordon Research Conference (Computational Chemistry) with poster entitled "An auxiliary field quantum Monte Carlo study of the Hubbard Kanamori model" Jul 2018

- The American Physical Society (APS) March Meeting with talk entitled "An auxiliary field quantum Monte Carlo study of the Hubbard Kanamori model" Mar 2018
- The 58th Sanibel Symposium with poster entitled "Accurate determination and prediction of dipole-bound states using QMC" Feb 2018
- Auxiliary-Field Quantum Monte Carlo (AFQMC) Workshop at Simons Foundation with poster entitled "Accurate determination and prediction of dipole-bound states using QMC" Feb 2018
- The 254th American Chemical Society (ACS) National Meetings with poster entitled "Accurate determination and prediction of dipole-bound states using QMC" Aug 2017
- Telluride Science Research Center (TSRC) - Stochastic Approaches to Electronic Structure Calculations with poster entitled "Accurate determination and prediction of dipole-bound states using QMC" Jul 2017
- ARPA-E Energy Innovation Summit Mar 2016
- Gordon Research Conference (Carbon Capture, Utilization & Storage) May 2015

Honors

- ACS The Chemical Computing Group Excellence Award for Graduate Students 2019
- IBM-Zerner Graduate Student Award at 58th Sanibel Symposium 2018
- APS/DCOMP Travel Award 2018
- Joukowsky Summer Research Award 2017
- First prize winner of the International Mathematical Contest in Modeling 2013
- Awarded as "Jilin University Outstanding Graduate" 2014
- National Encouragement Scholarship (Top 5%) 2011-2013
- Social Scholarship from EVONIK 2012

- National Scholarship (Top 2%) 2011-2012
- Social Scholarship from CSPC PHARMA 2011

Community Service

- Volunteer for the Big Bang WaterFire Science Fair Demonstrations organized by Brown University Sep 2018
- Volunteer for STEM I or II Pre-college program, hosted by Brown's School of Professional Studies Jul 2018
- Judge at the Rhode Island Science and Engineering Fair Mar 2018

Acknowledgments

My deepest gratitude is to my advisor Prof. Brenda M. Rubenstein, who gave me the freedom to learn, grow and explore on my own. I came to the group with little theoretical background. Prof. Rubenstein is very supportive and patient which allowed me to find the most suitable way for me to make progress. She inspired me on how best to express ideas professionally, think critically, and question things in a bigger picture. The high standards that she holds towards research are such an inspiration to me and will stay with me throughout my life and career. Beyond research, I will always be grateful for the tremendous freedom and support that she gave me to explore what I really want to choose as a life long career. I am very fortunate to have her as a mentor.

I am also ineffably grateful to Prof. Brad Marston and Prof. Andrew Peterson, who have graciously agreed to serve on my dissertation committee, spent time reading my work, and provided invaluable feedback.

I would like to thank my collaborators, fellow doctoral students, and postdoctral researchers in and outside of our group for friendship, discussions, and collaborations. I especially thank Prof. Kenneth D. Jordan, Prof. Can Ataca, and Dr. Hao Shi for fruitful insights/discussions and their full support of my future plan. I also thank Mr. James Shee, Mr. Yuan Liu, Mr. Shiv Upadhyay, Dr. Ravindra Nanguneri, Dr. Jeong-Pil Song, and Mr. Cancan Huang for peer discussions. I thank Wenze Gu

and Haobo Yang for being my officemates and spending our graduate years together. Lastly, I thank everyone in the group who make up my theoretical family!

I am grateful to the Department of Chemistry and graduate school of Brown University for generous financial support over the past five years. I especially thank the "William R. Potter Chemistry Graduate Student Conference Travel Grants", which provided me many opportunities to attend conferences and develop professional presentation and networking skills.

Last but not least, I am grateful to my husband, my parents, and all my friends, who have encouraged and supported me along the way. I could never finish this dissertation without them.

Abstract of "Achieving High Accuracy with Low Cost: Successful Applications of Auxiliary Field Quantum Monte Carlo to Weakly-Bound Molecules and Strongly Correlated Materials", by Hongxia Hao, Ph.D., Brown University, October 2019

The accurate evaluation of quantum mechanical properties of molecules and materials becomes more challenging when highly accurate descriptions of electron correlation are required. Different flavors of theories have been actively developed and successfully applied to a wide array of physical and chemical problems. However, the curse of dimensionality caused by the exponential increase of the Hilbert space limits the scalability and accuracy of most numerical methods. In this thesis, we provide an alternative to conventional wave function techniques by using Auxiliary Field Quantum Monte Carlo (AFQMC) methods which are highly accurate, yet possess a favorable $O(N^3)$ scaling. This thesis mainly describes the accurate modeling of weakly-bound, yet correlated molecules and strongly-correlated materials in which complicated electron correlations are involved by using AFQMC.

The first part of this thesis presents the simulation of a fascinating class of weakly-bound species known as dipole-bound anions. The theoretical description of weakly-bound anions remains a challenge, due in part to the relatively weak, yet correlated nature of the dipole interaction ($\sim$ tens to hundreds wave numbers). Here, we demonstrate that a new correlated sampling AFQMC scheme can more successfully predict and obtain the electron binding energies for molecular dipole bound anions than standard, uncorrelated Diffusion Monte Carlo and AFQMC simulations. These results pave the way toward using these approaches for the study of weakly-bound species that are too large to model using traditional electronic structure methods.

The second part of this thesis describes the development and application of a theoretical framework for treating the multiband Hubbard Kanamori (HK) model within AFQMC. We elucidate the feasibility and high accuracy of applying AFQMC

to the HK model and study the low temperature phase diagram of Ca_2RuO_4 for a range of layered perovskite structures using AFQMC and DMFT, representing the first application of AFQMC to $4d$ materials and the first rigorous comparison of AFQMC and DMFT phase diagrams. Our many-body simulations explain the electronic origin of the magnetic and metal-insulator transitions in Ca_2RuO_4.

Portions of the work have been published in Hao *et al*, *J. Phys. Chem. Lett.* 9, 6185, 2018 and Hao *et al*, *Phys. Rev. B* 99, 235142, 2019, which are introduced in Chapters 3 and 4. The work in Chapter 5 is currently unpublished, but has been prepared for submission to *Phys. Rev. Lett.*.

Contents

List of Tables

List of Figures

Chapter One

Introduction

The accurate evaluation of quantum mechanical properties of molecules and materials has been a long-standing and central goal of quantum chemistry. One of the major impediments to achieving this goal is the so-called *many-body problem*, *i.e.*, the challenge of accurately describing the electron correlations among many electrons in complex systems in which electron correlations dominate their interesting properties. Such problems include but are not limited to weakly-bound anionic molecules [220, 232], transition metal oxides [119, 120, 134], and high-temperature superconductors [81, 106, 224]. Thus, a lot of effort has been spent over the past decades developing new theoretical methods for the accurate evaluation of electron correlation energies [24, 65, 226, 228, 229], and plenty of advanced theoretical techniques have been applied to a variety of problems of interest helped by the increase of modern computational power.

A fundamental goal of the quantum community, including the fields of quantum chemistry, condensed matter physics, and materials science, is to determine the properties of many interacting electrons and nuclei quantum mechanically by solving the time-independent Schrödinger equation

$$\hat{H}\Psi(\vec{r},\vec{R}) = E\Psi(\vec{r},\vec{R}), \tag{1.1}$$

where $\hat{H}$ is the system Hamiltonian, $\Psi(\vec{r},\vec{R})$ is the many-body wave function of the system, and E is the energy eigenvalue. In atomic units, the Hamiltonian is given by

$$\hat{H} = -\sum_{m}\frac{\nabla^2_{\vec{R}_m}}{2M_m} - \sum_{i}\frac{\nabla^2_{\vec{r}_i}}{2} - \sum_{m,i}\frac{Z_m}{\mid \vec{R}_m - \vec{r}_i \mid} + \sum_{m,n>m}\frac{Z_m Z_n}{\mid \vec{R}_m - \vec{R}_n \mid} + \sum_{i,j>i}\frac{1}{\mid \vec{r}_i - \vec{r}_j \mid}, \tag{1.2}$$

where $\vec{R}_m$ denotes the spatial coordinate of nucleus m, M_m denotes the mass of nucleus m, and Z_m denotes the charge of nucleus m. $\vec{r}_i$ denotes the spatial

coordinates of the electrons.

To obtain the total energy, Hartree-Fock self-consistent-field theory is often used as a mean-field starting point [83], which recovers about $\sim 99\%$ of the total energy of the system. However, in reality, the remaining 1% of the energy is crucial for the accurate and quantitative description of the system. The energy difference between the exact nonrelativistic total energy of the system and the Hartree-Fock energy is defined as the "electron correlation energy" [128].

Explicit calculation of the correlation energy, *i.e.*, the exact solution to the Schrödinger equation, can quickly become computationally prohibitive due to the exponential growth of the size of the many-body wave function with the number of particles [111]. Essentially we are attempting to solve a very high dimensional partial differential equation, and the curse of dimensionality hasn't been resolved in effective ways mathematically. As Paul Dirac said, "The underlying physical laws necessary for a large part of physics and the whole of chemistry are thus completely known, and the difficulty is only that the exact applications of these laws lead to equations much too complicated to be soluble."

Different levels of approximations are applied to simplify the problem to be solvable with polynomial scaling. One of the "exact" theories is Density Functional Theory (DFT), which is based on the Hohenberg-Kohn theorems [92] that the ground state properties of a many-electron system are only a function of the electron density. Any quantity you want to calculate can be re-expressed in terms of the electron density, $n(\vec{r})$, including the many-body ground state wavefunction, $\Psi[n(\vec{r})]$. The Kohn-Sham equations [112] thus map a many-body interacting system to a system of non-interacting particles in an effective potential, which is a good approximation. Unfortunately, the exact form of the exchange-correlation potential, $V_{xc}[n(\vec{r})]$, as it

appears in the Kohn-Sham equations in order to account for many-body effects is in general not known. Even though there has been tremendous success generating approximate forms of the exchange-correlation functional with $O(N^3)$ scaling and these have been applied to a wide range of applications such as large-scale molecules and materials, the approximations can lead to qualitatively incorrect results for strongly-correlated systems for which an improved treatment of electron correlation is needed. Other flavors of theories such as perturbation theories (GW approximation, Møller-Plesset perturbation theory), embedding theories (density matrix embedding theory, self-energy embedding theory) and coupled-cluster theory all aim to provide a better description of the electron correlations and remain under active development. However, most of them are deterministic methods and eventually will encounter computational scaling and memory bottlenecks.

Instead of solving the problem deterministically, quantum Monte Carlo (QMC) methods try to solve the Schrödinger equation in a stochastic way, by using random numbers that sample the necessary probability distributions. The term "Monte Carlo" was first coined by Stanislaw Ulam in 1946, in honor of his uncle who had a gambling addiction [91]. The technique was later developed by Metropolis as well [139]. Since Monte Carlo sampling is relatively insensitive to dimensionality, it shed light on tackling the "dimensionality" problem in an efficient way. Actually, there are several advantages of using QMC methods, such as:

1. QMC methods are highly parallel, allowing them to take advantage of modern computational infrastructure such as supercomputers with little modification. This enables its application to large system sizes.

2. The computational cost for each step of a QMC calculation is small, traditionally scaling as $O(N^3 \sim N^4)$, where N is a measure of system size.

3. The memory cost of QMC methods is small, which enables them to be easily adapted to graphical processing unit (GPU) architectures.

4. In principle, any high statistical precision can be achieved by adjusting the sampling time. The random error of QMC calculations decreases in proportion to the square root of the number of sampling points.

It turns out that QMC methods are able to achieve very high accuracy and have been among the most accurate methods for studying quantum mechanical properties of systems. They can provide "exact" solutions to the Schrödinger's equation for systems of bosons. Since electron correlation is treated explicitly, including a natural treatment of both static and dynamic correlation effects, QMC can achieve an accuracy for fermion systems similar to the gold standard "coupled-cluster with singles, doubles, and perturbative triples (CCSD(T))" method in quantum chemistry, and may even be regarded as the "standard" for studying strongly-correlated materials and large-scale systems.

However, the QMC method also exhibits some disadvantages that make it the subject of continued research:

1. The infamous "sign" problem exists in most fermion systems. Because of the anti-symmetry of the fermion wave function, random walks have an equal probability of sampling the positive or negative portions of the wave function, which causes an exponential decline in the signal to noise ratio with projection time and/or increases in system size because the negative and positive contributions cancel each other.

2. There is a large computational prefactor that accompanies computing observable averages with a targeted small statistical error, which undercuts QMC's

advantages on small- to medium-sized systems that other high-accuracy methods can handle.

3. The accuracy and speed of QMC methods that require trial wave functions to curb the sign problem depend on the quality of the trial wave function used to some extent.

4. It's possible, but challenging to target any excited state in QMC.

To tackle the "sign" problem, approximations such as "fixed-node" approximation [7] in Diffusion Monte Carlo (DMC) and the constrained path approximation [236] in Auxiliary Field Quantum Monte Carlo (AFQMC) have been adopted to constrain the sampling space to only portions that have positive overlaps with the trial wave function. With these approximations, together with other optimization techniques such as importance sampling and background subtraction, these methods typically provide high-quality results that have led to many successful applications in various areas of chemistry, physics, and materials [13, 130, 189].

In this thesis, we will focus on one QMC method - AFQMC. AFQMC is a wave function based QMC technique that reconstructs a system's ground state wave function and related observables through an imaginary time projection that samples the space of non-orthogonal Slater determinants [235, 236] in second quantization notation. The method is theoretically and mathematically exact, but possesses the infamous "sign" problem. Even though the constrained path/phaseless approximations are employed together with importance sampling and background subtraction to curb the sign/phase problem and improve sampling efficiency, AFQMC's accuracy limits are not yet fully mapped out and a more thorough exploration of this method in wide range of fields is needed.

The accurate modeling of weakly-bound, yet correlated molecules and strongly-correlated materials remain two outstanding challenges in quantum chemistry due to the complexity of the electronic interactions involved in these systems. In this thesis, I present the further application-driven development of ground state AFQMC method. The rest of the thesis is organized as follows.

In Chapter 2, I introduce the general theoretical scheme for AFQMC that will be used in the following method extensions and applications.

In Chapter 3, I present an exploration of the AFQMC method for dealing with dipole-bound anions, for which weak and long-range interactions require an explicit description of the many-body effects.

In Chapter 4, I illustrate a detailed theoretical scheme to treat the multiband Hubbard Kanamori model in AFQMC in order to better explore strongly-correlated d- and f- electron materials.

In Chapter 5, I demonstrate one possible application of the Hubbard Kanamori model to the study of $4d$ layered perovskite ruthenate materials which possess a Mott insulator phase transition. The success of studying the microscopic origin of phase transitions at low temperatures using AFQMC opens the door to the study of a much broader range of 4- and $5d$ transition metal oxides with unexpected physics that was not previously possible using less accurate techniques.

Chapter Two

The Preliminaries

In this chapter, we will focus on the ground state AFQMC theory and demonstrate the key features that will be used in the following studies.

2.1 Hamiltonian

In the first quantization, the general formalism of the ground state Hamiltonian for many-electron fermion system can be written as

$$\hat{H} = -\sum_{m} \frac{\nabla^2_{\vec{R}_m}}{2M_m} - \sum_{i} \frac{\nabla^2_{\vec{r}_i}}{2} - \sum_{m,i} \frac{Z_m}{\mid \vec{R}_m - \vec{r}_i \mid} + \sum_{m,n>m} \frac{Z_m Z_n}{\mid \vec{R}_m - \vec{R}_n \mid} + \sum_{i,j>i} \frac{1}{\mid \vec{r}_i - \vec{r}_j \mid} \tag{2.1}$$

Under the Born-Oppenheimer approximation where the mass of the nucleus is much larger than the electron and the motion of the nucleus is much slower than the electron, the kinetic energy of the nucleus (first term in Equation 2.1) can be neglected, the nucleus-nucleus interaction (fourth term in Equation 2.1) can be viewed as a constant. It can be finally divided into the one-body interaction terms that includes the electron kinetic energy and the electron-nucleus interaction, and the two-body interaction terms that come from the electron-electron interactions. The final Hamiltonian under Born-Oppenheimer approximation becomes:

$$\hat{H} = -\sum_{i} \frac{\nabla^2_{\vec{r}_i}}{2} - \sum_{m,i} \frac{Z_m}{\mid \vec{R}_m - \vec{r}_i \mid} + \sum_{i,j>i} \frac{1}{\mid \vec{r}_i - \vec{r}_j \mid} \tag{2.2}$$

To ease the representation in quantum chemistry, many theories including AFQMC work under second quantization notaion using some one-particle basis. An

equivalent form of the *ab initio* Hamiltonian without spin index can be written as,

$$\hat{H} = \hat{H}_1 + \hat{H}_2 = \sum_{ij} T_{ij} \hat{c}_i^\dagger \hat{c}_j + \frac{1}{2} \sum_{ijkl} V_{ijkl} \hat{c}_i^\dagger \hat{c}_j^\dagger \hat{c}_k \hat{c}_l. \tag{2.3}$$

Here, i, j, k, and l denote different molecular orbitals in a specified one-particle basis. V_{ijkl} denotes the two-body and T_{ij} the one-body integrals in this basis. $\hat{c}_i^\dagger$ represents a creation operator that creates an electron in molecular orbital i; $\hat{c}_j$ represents an annihilation operator that annihilates an electron in molecular orbital j [208]. For ease of notation below, we moreover let $\hat{H}_2$ represent the collection of all two-body operators and $\hat{H}_1$ represent the collection of all one-body operators.

2.2 Projection

AFQMC is a projection-based method that extracts the ground-state wave function by propagating the Schrödinger equation in imaginary time. It is rooted from the time dependent Schrödinger equation and its time-independent solution,

$$\frac{\mathrm{d}}{\mathrm{d}t} \Phi(\mathbf{X}, t) = -iH\Phi(\mathbf{X}, t), \tag{2.4}$$

$$\Phi(\mathbf{X}, t) = \mathrm{e}^{-iHt} \Phi(\mathbf{X}, t = 0), \tag{2.5}$$

When the potential energy doesn't change by time, by shifting the Hamiltonian on the exponential by the ground-state energy[1], one can easily obtain the ground state wave function when the imaginary time, $\tau = it$, becomes large:

$$\lim_{\tau \to \infty} \Phi(\mathbf{X}, \tau) = \mathrm{e}^{-\tau(H - E_0)} \Phi(\mathbf{X}, \tau = 0), \tag{2.6}$$

[1] this can guarantee the exponential approaches 1 with relative small imaginary time.

so

$$|\Psi_0\rangle \propto \lim_{n\to\infty} \left(e^{-\Delta\tau \hat{H}}\right)^n |\Psi_I\rangle, \tag{2.7}$$

where $|\Psi_0\rangle$ denotes the ground state wave function, $\Delta\tau$ is an increment of imaginary time, $\hat{H}$ is the system's many-body Hamiltonian, $|\Psi_I\rangle$ is the initial wave function, typically composed of one or more determinants, and n is the number of times the projection operator is applied.

According to the Suzuki-Trotter decomposition [207, 212], the exponential of two arbitrary operators $\hat{A}$ and $\hat{B}$ with some commutation relation $[\hat{A}, \hat{B}] \neq 0$ can be given by:

$$e^{x(\hat{A}+\hat{B})} = e^{x\hat{A}} e^{x\hat{B}} + O(x^2), \tag{2.8}$$

where the product of the exponential operators on the right-hand side can be treated as an approximate decomposition of the exponential operator on the left-hand side with the error scales as the second order of x. A higher order approximation can be

$$e^{x(\hat{A}+\hat{B})} = e^{x\hat{B}/2} e^{x\hat{A}} e^{x\hat{B}/2} + O(x^3), \tag{2.9}$$

Assuming $\Delta\tau$ is small, the projection operator of Equation (2.7) may be factored into

$$e^{-\Delta\tau\hat{H}} \approx e^{-\Delta\tau\hat{H}_1/2} e^{-\Delta\tau\hat{H}_2} e^{-\Delta\tau\hat{H}_1/2}, \tag{2.10}$$

According to Thouless's Theorem [209] that any N-particle Slater determinant Φ can be written in the form

$$
\begin{aligned}
|\Phi\rangle &= [exp(\sum_{i=1}^{N}\sum_{m=N+1}^{\infty} C_{mi}c_m^\dagger c_i)]|\Phi_0\rangle \\
&= e^{\hat{C}}|\Phi_0\rangle
\end{aligned}
\tag{2.11}
$$

where the operator $c_i^\dagger$ creates a particle with orbital ψ_i, and the operator c_i annihilates a particle with orbital ψ_i for a N-particle system, and the coefficients C_{mi} are uniquely determined. The theorem says that the effect of the $e^{\hat{C}}$ operator is to transform any single determinant into any other non-orthogonal single determinant. The action of an exponential of a one-body operator on a determinant results in another determinant, reducing the process of projecting a one-body operator onto the initial wave function into standard matrix multiplication. However, no such theorem applies to exponentials of two-body operators.

As derived in Appendix A and B with/without spin symmetry, the *ab initio* Hamiltonian may always be rewritten as the sum of squares of one-body operators. In particular, the two-body matrix elements, V_{ijkl}, may be expressed in terms of Cholesky vectors as $V_{ijkl} = \sum_\alpha L_{ik}^\alpha L_{jl}^\alpha$ [163]. If each one-body operator is expressed as $\hat{v}_\alpha \equiv i\sum_{ik} L_{ik}^\alpha \sum_\sigma \hat{c}_{i\sigma}^\dagger \hat{c}_{k\sigma}$, then $\hat{V} = -\frac{1}{2}\sum_\alpha \hat{v}_\alpha^2$. The fact that the two-body potential may be written in terms of the squares of one-body operators makes it amenable to a continuous Hubbard-Stratonovich (HS) transformation [146, 235]:

$$
e^{\Delta\tau\hat{v}_\alpha^2/2} = \frac{1}{\sqrt{2\pi}}\int_{-\infty}^{\infty} dx_\alpha e^{-x_\alpha^2/2} e^{x_\alpha\sqrt{\Delta\tau}\hat{v}_\alpha},
\tag{2.12}
$$

where x_α is a scalar quantity known as an auxiliary field corresponding to term α. This transformation is realized by sampling the auxiliary field x_α from a Gaussian distribution and then using that field to construct the one-body operator $e^{x_\alpha\sqrt{\Delta\tau}\hat{v}_\alpha}$.

Combining these transformations for all α and inserting into Equation 2.10 yields the final expression for the propagator

$$e^{-\Delta\tau\hat{H}} \approx e^{-\Delta\tau\hat{K}/2}\Big[\int_{-\infty}^{\infty} P(\vec{x})\hat{B}(\vec{x})d\vec{x}\Big]e^{-\Delta\tau\hat{K}/2}. \tag{2.13}$$

Here, $\vec{x}$ denotes the vector of all α auxiliary fields, $P(\vec{x})$ denotes the Gaussian probability of a given set of fields, and $\hat{B}(\vec{x})$ is a collection of one-body operators. In a typical AFQMC simulation, walkers are first initialized to a trial wave function. Then, randomly-sampled instances of $e^{-\Delta\tau\hat{H}}$ are constructed according to Equation 2.13 and iteratively applied to each walker's trial wave function to realize a random walk through Slater determinant space. Simulations proceed until the stochastic error bars on observables averaged across the ensemble of walkers are small enough to meet a desired target.

Because the $\hat{v}_\alpha$ are typically imaginary, the HS transformation results in complex operators, and by extension, complex walker weights [237]. Averaging observables over these complex weights typically results in a phase problem that makes recovering meaningful observable averages from the noise impossible in a fixed amount of computational time [237]. In order to mitigate the noise incurred during the simulations, we perform background subtraction [164], in which we subtract $\langle\hat{v}_\alpha\rangle$, the expectation value of $\hat{v}_\alpha$ with respect to the trial wave function, from $\hat{v}_\alpha$. We also apply a force bias [146, 164] which minimizes the fluctuations of our walker weights with respect to the selected auxiliary fields by subtracting $\bar{x}_\alpha = -\sqrt{\Delta\tau}[\bar{v}_\alpha - \langle\hat{v}_\alpha\rangle]$, where $\bar{v}_\alpha \equiv \frac{\langle\Psi_T|\hat{v}_\alpha|\Psi\rangle}{\langle\Psi_T|\Psi\rangle}$, from x_α. Combining these modifications, the one-body operator in Equation 2.12 becomes $e^{(x_\alpha-\bar{x}_\alpha)\sqrt{\Delta\tau}(\hat{v}_\alpha-\langle\hat{v}_\alpha\rangle)}$. By reducing the overall magnitude of the exponent in the propagator, the force bias and background subtraction substantially

reduce the phase problem. Nevertheless, AFQMC simulations of molecules also necessitate employing the phaseless approximation. In the phaseless approximation [237], after each propagation step, walker weights are projected back onto the real axis by multiplying them by $\max\{0, \cos(\Delta\theta)\}$, where the phase angle is defined as $\Delta\theta = \Im\{\ln \frac{\langle\Psi_T|\Psi^{(\tau+1)}\rangle}{\langle\Psi_T|\Psi^{(\tau)}\rangle}\}$. Combined with background subtraction and importance sampling, the phaseless approximation has been demonstrated to yield chemically accurate results on a wide range of benchmarks [2, 3, 4, 5, 162, 203]. The techniques mentioned above will be described in detail in the following.

2.3 Walkers

2.3.1 Population Control

Several schemes have been invented to control the fluctuations of the walker population. These population control adjustments changed the walker weights, and hence introduce bias into propagations and observable estimations. Intuitively, if the control magnitude is too small, the population fluctuations will be hard to control, while if the control magnitude is too large, there could be a large bias on the propagation path and estimators. Here we would list a few types of population control schemes that include the dynamical population and fixed population types. These population control bias can be systematically reduced, such as using importance sampling with a better trial wavefunction [22, 215], adjusting the trial energy on the fly [22], and populating with large target population size [215].

2.3.1.1 Branching

The branching scheme is essentially a birth-death algorithm with fluctuating population. Walkers with weight above *max_weight* are split into multiple walkers of weight *reset_weight*. Walkers with weight below *min_weight* are killed with probability (*weight/min_weight*). However, it may cause load balance issue that the number of walkers on each processor will differ a lot which will decrease the computational efficiency.

2.3.1.2 Comb

A better solution to the fluctuating population problem is the fixed-population algorithm. One solution is the "comb" technique. It takes a stochastic procedure for selecting M new walkers from a list of N unevenly weighted walkers from the original list. More specifically, first, we construct the cumulative sums of the original weights $C_j = \sum_{i=1}^{j} \omega_i$ where $j = 0, 1, 2, ..., N$, with $C_0 = 0$ and $C_N = W_T$. Then generate a random number between (0,1) with uniform distribution δ. Finally find the walker index j between 1 and N that satisfies $C_{j-1} < (k - 1 + \xi)\frac{W_T}{M} \leq C_j$. Depending on the weight difference, the walker index j can be selected multiple times. Notice that this approach only requires one random number generator. Another way to do comb is to have a normalized original weight summation that $W'_T = 1$. The space of (0,1) is split into N regions, with N walkers occupied one by one following their index, and the length of each region is denoted by the normalized weight of each walker. Then have M generated random numbers uniformly distributed between (0,1), each of them will correspond to a j that $C'_{j-1} < \delta \leq C'_j$, then the j walker will be in the new list.

2.4 Sampling in AFQMC

2.4.1 The Sampling Process

One of the most computationally efficient ways of evaluating many dimensional integrals such as that given by Equation 2.13 is to use Monte Carlo sampling techniques. As described in more detail in previous publications [89, 234, 235, 236], if $|\Psi_I\rangle$ is represented by a single Slater determinant, after each application of the projection operator, a new Slater determinant will be produced. Thus, if k instances (so-called "walkers") are initialized to $|\Psi_I\rangle$ and the projection operation given by Equation 2.13 is applied to each of them by independently sampling sets of fields, then a random walk through the space of non-orthogonal determinants is realized in which the overall wave function at time slice n, $|\Psi^{(n)}\rangle$, is represented by an ensemble of k wave functions $|\psi_k^{(n)}\rangle$ with weights $w_k^{(n)}$

$$|\Psi^{(n)}\rangle = \sum_k w_k^{(n)} |\psi_k^{(n)}\rangle. \tag{2.14}$$

Here, the $w_k^{(n)}$ consist of the products of scalars accumulated over all time slices by walker k, which can be complex.

Ground state observables at each time slice, such as the energies reported below, may then be computed by evaluating the mixed estimator [50] over the ensemble

$$\begin{aligned} \langle \hat{A} \rangle_{mix} &= \frac{\langle \Psi_T | \hat{A} | \Psi^{(n)} \rangle}{\langle \Psi_T | \Psi^{(n)} \rangle} \\ &= \frac{\sum_k w_k^{(n)} \langle \Psi_T | \hat{A} | \psi_k^{(n)} \rangle}{\sum_k w_k^{(n)} \langle \Psi_T | \psi_k^{(n)} \rangle}, \end{aligned} \tag{2.15}$$

where $|\Psi_T\rangle$ denotes a trial wave function that approximates the true ground state

wave function. To facilitate the evaluation of the mixed estimator, it is common to introduce the local energy

$$E_L[\Psi_T, \Phi] \equiv \frac{\langle \Psi_T | \hat{H} | \Phi \rangle}{\langle \Psi_T | \Phi \rangle}, \tag{2.16}$$

such that Equation 2.15 may be simplified to

$$\langle \hat{A} \rangle_{mix} = \frac{\sum_k w_k^{(n)} \langle \Psi_T | \psi_k^{(n)} \rangle E_L[\Psi_T, \psi_k^{(n)}]}{\sum_k w_k^{(n)} \langle \Psi_T | \psi_k^{(n)} \rangle}. \tag{2.17}$$

After a sufficiently large number of time slices such that $|\Psi^{(n)}\rangle$ approaches the ground state, final estimates of $\langle \hat{A} \rangle$ may be obtained by averaging over each time slice expectation value.

A population control procedure [18] is needed during the random walk. During this procedure, walkers with larger weights are replicated and those with smaller weights are eliminated probabilistically. The weight used in population control is

$$W_k^{(n)} = w_k^{(n)} \langle \Psi_T | \psi_k^{(n)} \rangle. \tag{2.18}$$

When there is a sign or phase problem, $W_k^{(n)}$ may become negative or complex. As described in Section 2.4.2.3 and Section 2.4.2.4, $W_k^{(n)}$ is always positive or zero if the constrained path or phaseless approximations are employed.

2.4.2 The Sign and Phase Problems

Unfortunately, the "free" projection process just described is typically beset by either the sign [23, 127] or phase problems [237]. These problems fundamentally stem from the fact that observables computed using a single Slater determinant,

$|\Psi\rangle$, remain invariant to arbitrary rotations, $e^{i\theta}|\Psi\rangle$, of that determinant, where θ is a phase angle. Consequently, during the course of an AFQMC simulation involving complex propagators, walkers may accumulate infinitely many possible phases (as there are infinitely many possible phase angles, $\theta \in [0, 2\pi)$), resulting in infinitely many possible determinants. Since these phases are directly multiplied into the walker weights of Equations 2.15 and 2.17, after many iterations, the walker weights end up populating the entire complex plane and many of the terms summed to compute weighted averages of observables cancel one another out. This cancellation leads to an exponential decline in observable signal to noise ratios that manifests as infinite variances [192] called the phase problem. If transformations that preclude propagators from becoming complex are employed as described above, positive and negative versions of each determinant may still be generated, resulting in a somewhat less pernicious cancellation of positive and negative weights termed the sign problem. If left unchecked, the sign and phase problems render obtaining meaningful observable averages nearly impossible, thwarting AFQMC simulations. We therefore mitigate these problems using a combination of background subtraction, importance sampling, and either the constrained path (for the sign problem) or phaseless (for the phase problem) approximations.

2.4.2.1 Background Subtraction

One of the simplest ways of reducing variances within AFQMC is via background subtraction [165]. As part of background subtraction, the two-body portion of a Hamiltonian is rewritten so that a mean field average is subtracted from each one-body operator. Thus, if the original two-body operator may be written as a square such that $\hat{V} = -\frac{1}{2}\sum_i \hat{v}_i^2$ to make it amenable to a HS transformation, as part of

background subtraction, it would be re-expressed as

$$\hat{V} = -\frac{1}{2}\sum_i (\hat{v}_i - \langle \hat{v}_i \rangle)^2 - \sum_i \hat{v}_i \langle \hat{v}_i \rangle + \frac{1}{2}\sum_i \langle \hat{v}_i \rangle^2, \tag{2.19}$$

where $\langle \hat{v}_i \rangle$ denotes the mean field average of the operator $\hat{v}_i$. Because the modified $\hat{v}_i - \langle \hat{v}_i \rangle$ operator will be smaller in magnitude than the bare $\hat{v}_i$ operator, background subtraction reduces the variance involved in AFQMC simulations.

2.4.2.2 Importance Sampling

To further reduce the variance of walker weights and to make our simulations more amenable to the constrained path and phaseless approximations, we additionally perform importance sampling, which aims to shift the center of the distribution from which we sample our auxiliary fields so that the most important fields are sampled more frequently. The conventional way of performing importance sampling in AFQMC simulations is by introducing a force bias that shifts each sampled field by an amount dependent upon the operator being transformed and the current walker wave function [164, 171, 191, 237]. Because we later will use a mixture of discrete and continuous transformations and force bias importance sampling is only applicable to continuous transformations, I present a formally equivalent strategy in which we shift *the propagators instead of the auxiliary fields.*

For continuous HS transformations, this may be accomplished by shifting the operator $\hat{A}$ by $\langle \hat{A} \rangle$ in Equation 2.12

$$\begin{aligned} e^{-\Delta\tau \hat{A}^2/2} &= \int dx \frac{1}{\sqrt{2\pi}} e^{-x^2/2} e^{x\sqrt{-\Delta\tau}\hat{A}} \\ &= \int dx \frac{1}{\sqrt{2\pi}} e^{-x^2/2} e^{x\sqrt{-\Delta\tau}\langle \hat{A} \rangle} e^{x\sqrt{-\Delta\tau}(\hat{A} - \langle \hat{A} \rangle)}, \end{aligned} \tag{2.20}$$

where x is each auxiliary field and $\langle \hat{A} \rangle$ is the mixed estimator of $\hat{A}$

$$\langle \hat{A} \rangle \equiv \frac{\langle \Psi_T | \hat{A} | \psi_k^{(n)} \rangle}{\langle \Psi_T | \psi_k^{(n)} \rangle}. \tag{2.21}$$

If we define the dynamic force as $F \equiv \sqrt{-\Delta\tau}\langle \hat{A} \rangle$, then Equation 2.20 may be re-expressed as

$$\begin{aligned} e^{-\Delta\tau \hat{A}^2/2} &= \int dx \frac{1}{\sqrt{2\pi}} e^{-x^2/2} e^{xF} e^{x\sqrt{-\Delta\tau}\hat{A} - xF} \\ &= \int dx \frac{1}{\sqrt{2\pi}} e^{-(x-F)^2/2} e^{\frac{1}{2}F^2} e^{x\sqrt{-\Delta\tau}\hat{A} - xF} \\ &= \int dx \frac{1}{\sqrt{2\pi}} e^{-(x-F)^2/2} e^{\frac{1}{2}F^2 - xF} e^{x\sqrt{-\Delta\tau}\hat{A}}. \end{aligned} \tag{2.22}$$

To realize this transformation, fields are sampled from the shifted Gaussian probability density function, $\frac{1}{\sqrt{2\pi}} e^{-(x-F)^2/2}$, and the propagator $e^{x\sqrt{-\Delta\tau}\hat{A}}$ is applied with weight $e^{\frac{1}{2}F^2 - xF}$. The field distributions are now centered around the dynamic force, which can be shown to minimize the variance. If the dynamic force F is complex, our auxiliary fields will have the same imaginary part to ensure $x - F$ is real. Then, the probability function $\frac{1}{\sqrt{2\pi}} e^{-(x-F)^2/2}$ will remain real and therefore amenable to sampling.

2.4.2.3 Constrained Path Approximation

To address the sign problem that may emerge when our propagators, $\hat{B}(\vec{x})$, are real, we employ the constrained path approximation [236]. Here, we impose this approximation by requiring that all walkers maintain a positive overlap with the trial wave function after each propagation step

$$w_k^{(n)} \langle \Psi_T | \psi_k^{(n)} \rangle > 0. \tag{2.23}$$

As in typical constrained path implementations, walkers with negative overlaps with the trial wave function will be killed (have their weights set equal to zero), preventing them from being propagated further. This condition will select for only walkers with positive determinants, eliminating the sign problem. It can be shown that if the trial wave function is the exact ground state wave function, this condition will be exact [21]; however, since the trial wave function is typically unknown, constraining the propagation path in this way results in a small, but consequential approximation [25, 192].

2.4.2.4 Phaseless Approximation

In cases in which our propagators are complex, instead of employing the constrained path approximation, we employ the more general phaseless approximation [165, 237]. The phaseless approximation controls the phase problem by projecting complex walker weights onto the positive real axis according to the equation

$$W_k^{(n)} = |W_k^{(n)}| \times \max(0, \cos(\Delta\theta)), \tag{2.24}$$

where $W_k^{(n)}$ is defined in Equation 2.18 and $\Delta\theta$, the phase angle, is defined as

$$\Delta\theta = Arg\left[\frac{\langle\Psi_T|\hat{B}(x)|\psi_k^{(n)}\rangle}{\langle\Psi_T|\psi_k^{(n)}\rangle}\right] \approx O(Im(xF)). \tag{2.25}$$

The use of the cosine function to project also ensures that the density of the walkers will vanish at the origin. Because this cosine projection does not affect walkers with real weights, in practical implementations, we apply Equation 2.24 to realize both the constrained path and phaseless approximations.

Combined with background subtraction and importance sampling, the constrained path/phaseless approximation has been demonstrated to yield chemically accurate results on a wide range of benchmarks [2, 3, 4, 5, 162, 203].

Chapter Three

The Modeling of Dipole-Bound Anion using Quantum Monte Carlo

3.1 Introduction

Dipole-bound anions are an intriguing class of molecules that bind electrons not via their nuclear charge, but via their dipole moments [103, 195]. As the charge-dipole attraction is governed by a long-range potential that scales as $1/r^2$, dipole-bound electrons are typically delicately bound in diffuse orbitals far (one to even hundreds of angstroms [11, 70, 102]) from the centers of their parent molecules. Within the Born-Oppenheimer approximation, the critical dipole moment necessary for binding electrons is 1.625 D [30, 46, 214]. However, when corrections are made to the Born-Oppenheimer approximation and repulsive effects are included, the critical dipole moment for binding an electron grows to 2.5 D or larger [35, 56, 57, 129]. Aside from being the conceptually intriguing counterparts to usual valence-bound anions, it has been proposed that dipole-bound anions may be key contributors to the diffuse interstellar bands, a set of absorption peaks emanating from the interstellar medium whose source has yet to be conclusively identified [49, 69, 121, 135, 138, 182, 183]. Dipole-bound anions may also play a prominent role in radiation-induced mutagenesis, as nucleotides such as uracil and adenine have been observed to bind electrons through their dipoles [38, 85, 86, 93]. Interestingly, dipole-bound anions have been observed to transform into valence-bound anions and have therefore been termed the "doorway" to valence-bound molecules [29, 36, 39, 85]. The importance of dipole-bound anions in these settings, combined with the sheer experimental challenge of resolving the exceedingly small binding energies of such short-lived states, has motivated experimentalists to produce dipole-bound species via electron attachment [17, 86] and Rydberg electron transfer [35, 37, 75], and study them via field detachment and photoelectron spectroscopy [223]. These experiments have recently led to the discovery of such chemically-fascinating dipole-bound species as silatrane molecular cages that undergo substantial intramolecular distortions upon

binding an excess electron [12] and the resolution of the rich vibrational spectra of the dehydrogenated uracil radical [93] and 2-hydrophenoxide [94]. Moreover, dipole-bound anions are representative of a much larger class of nonvalence anionic species [220], including quadrupole-bound [28, 40, 41, 72, 198, 240] and polarization-bound [1, 48, 218] anions, and dipole-bound dianions [181, 196, 197], that manifest even more intricate and therefore intriguing binding.

From the theoretical perspective, dipole-bound anions are of particular interest because they pose a formidable challenge for *ab initio* methods – only high levels of theory are capable of accurately predicting dipole-bound anion electron binding energies [70, 71, 103]. Non-Born-Oppenheimer effects aside[1], the energy differences that discriminate between an anion that binds an electron and one that does not are often exceedingly small, on the level of tens to hundreds of wave numbers. Moreover, the magnitude of contributions that difficult-to-model dispersion interactions make to the binding energy can be comparable or even exceed the magnitude of the binding energies predicted by a mean field treatment alone [70, 71]. Indeed, a direct application of Koopman's Theorem at the Hartree-Fock level of theory can underestimate the binding energies of species like CH_3CN, C_3H_2, and $(H_2O)_2$ by 50% or more [70, 103] and the straightforward application of density functional theory can fail to predict binding whatsoever [238]. Past work has demonstrated that inclusion of high-order correlation effects is often required to obtain quantitative predictions of electron binding energies [70, 71, 73, 158], however methods that capture such effects typically scale steeply with system size. For example, one of the most frequently used such methods for dipole-bound anions is CCSD(T), which is limited to only small-to-medium-sized molecules containing on the order of 20 atoms or less because it

[1]Non-Born-Oppenheimer effects are most significant for anions like HCN^- whose rotational energy level spacings are similar in magnitude to their electron binding energies [10], but play less of a role in the species we focus on here [57, 58].

scales as N^7, where N is the number of electrons [169][2].

An attractive set of methods to treat such systems that promises accuracy on par with that offered by coupled cluster techniques are quantum Monte Carlo (QMC) methods [50, 146]. The primary advantage of QMC methods is that they scale as only $O(N^3) - O(N^4)$. The main disadvantage of QMC methods is that they all suffer from the fermion sign problem – an exponential decline in the signal to noise ratio with projection time and/or increases in system size. Different QMC methods work in different representations and therefore employ different approaches to curb the sign problem. Despite their sign-constraining approximations, QMC methods have proven to be remarkably successful at achieving chemical accuracy for a variety of molecules [2, 3, 4, 143, 161, 167, 203], including many non-covalently-bound species [44, 217, 232]. Even so, QMC has yet to be employed to study molecular dipole-bound anions.

In this work, we explore the accuracy with which Diffusion Monte Carlo (DMC) and Auxiliary Field Quantum Monte Carlo (AFQMC) can model dipole-bound species, with the aim of uncovering a new set of approaches for modeling large polarization-bound molecules. Interestingly, despite the different approximations they employ, we find that both methods can reproduce experimental results and distinguish molecules that bind an extra electron from those that do not. Furthermore, we find that a newly-developed correlated sampling AFQMC (C-AFQMC) approach [190] is particularly suited for the task of studying energy differences involving weakly-bound species, and for the species studied in this work, converges binding energies orders of magnitude faster than DMC and AFQMC

[2]Linear scaling techniques have recently emerged [170, 178] that dramatically reduce the cost of coupled cluster calculations. These techniques cannot be applied to dipole-bound anions, however, because they rely upon orbital localization schemes that cannot be applied to the diffuse orbitals that characterize dipole-bound species.

calculations that do not employ such sampling. This brings the modeling of the larger polarization-bound species to which we aspire tantalizingly into reach.

In the following sections, we will first summarize the methods we have employed in Section 3.2. We will then present and contextualize the binding energies and charge densities we have obtained for a variety of dipole-bound (and unbound) species in Section 3.3. Lastly, in Section 3.4, we will discuss the broader significance of our findings.

3.2 Methods: Calculation of Electron Binding Energies via Quantum Monte Carlo

In this work, we are primarily concerned with computing vertical electron affinities for several systems known to form dipole-bound anions. The vertical electron affinities of a molecule is defined as the difference between the energies of the neutral and anionic species in the neutral geometry. However, since the dipole-bound excess electron makes almost no impact on the geometry of the molecule, we can equate these electron affinities to the electron binding energies (EBEs), which are typically defined using the geometry of the anion. Computing binding energies via projector quantum Monte Carlo techniques, such as DMC or AFQMC, is a three step process: first, molecular geometries are optimized; next, trial wave functions, which provide the necessary constraints for sign/phase problem-free quantum Monte Carlo calculations, are generated using either variational Monte Carlo (VMC) or conventional quantum chemistry methods; and lastly, projector quantum Monte Carlo calculations are performed. We describe each of these steps and the related methods in more detail below.

3.2.1 Molecular Geometry Optimization

Vertical electron affinities are obtained by taking the difference between the energies of the neutral and anionic species both calculated at the neutral geometry. However, since the dipole-bound excess electron makes almost no impact on the geometry of the molecule, we equate these electron affinities to the electron binding energies (EBEs), which are typically defined using the geometry of the anion. Previous experimental [42, 76] and theoretical [74] investigations demonstrate that this approximation leads to errors of, at most, a few wave numbers, which validates our approach. That said, the geometries of the neutral molecules were first optimized using the MP2 method [141] together with the aug-cc-pVDZ basis set [45, 108] in Gaussian 09 [53, 54, 82, 177]. Even though zero-point energy differences may be as large as 10 cm^{-1} for some of the species studied, we did not include these contributions in our calculations because they were also not included in the coupled cluster calculations to which we compare and do not significantly alter our conclusions regarding the viability of using QMC methods to model dipole-bound anions.

3.2.2 Trial Wave Function Generation and Basis Sets Employed

Hartree-Fock (HF) wave functions generated in Gaussian 09 [82], GAMESS [187, 61], and NWChem [216] were used as trial wave functions in the DMC and AFQMC calculations. Spin-restricted Hartree Fock (RHF) wave functions were used for the neutral species, whereas spin-unrestricted Hartree Fock (UHF) wave functions were used for all of the anions except for C_3H_2, which necessitated the use of a Restricted Open-Shell Hartree Fock (ROHF) wave function. To obtain stable dipole-bound

anions, it is essential to use flexible basis sets with very diffuse basis functions. Here, we used the aug-cc-pVDZ basis set [45, 108] augmented with a set of diffuse s and p functions, and in one case, also d functions [70]. This basis set was employed to facilitate comparisons with previous coupled cluster results performed using the same basis set. With the exception of $C_3H_2O_3$, the diffuse functions were centered on an atom at the positive end of the molecular dipole, *i.e.*, on the S atom in SO, on the H atom in HCN, and on the most positive C atom in CH_3CN and C_3H_2. The exponents of the supplemental s, p and d functions form an even-tempered sequence, with the ratio between consecutive exponents being 3.2 and the smallest exponent being 2.2x10^{-5} a_0^{-2} for each angular momentum. Diffuse functions were added until electron binding energies were observed to converge at the Hartree Fock level of theory (similar convergence was observed using coupled cluster theory). A $6s6p$ set of supplemental diffuse functions was used for HCN and $C_3H_2O_3$, a $7s7p$ set was used for SO, CH_3CN, and CH_2CHCN, and a $7s7p7d$ set was used for C_3H_2. For $C_3H_2O_3$, the diffuse functions were located at a point on the molecule's twofold rotational symmetry axis, but outside of the molecular ring. The location of this point was determined by scanning the line 60 degrees from both carbon atoms for the location that maximized the electron affinity according to Hartree Fock calculations (see Figure 3.1).

3.2.3 Diffusion Monte Carlo

DMC is a real-space projector quantum Monte Carlo method that has found great success in modeling a wide range of molecules and solids, and has therefore been extensively reviewed in the literature [50, 153, 210]. Here, we summarize the algorithm for completeness. In DMC, a walker (sample) population representative

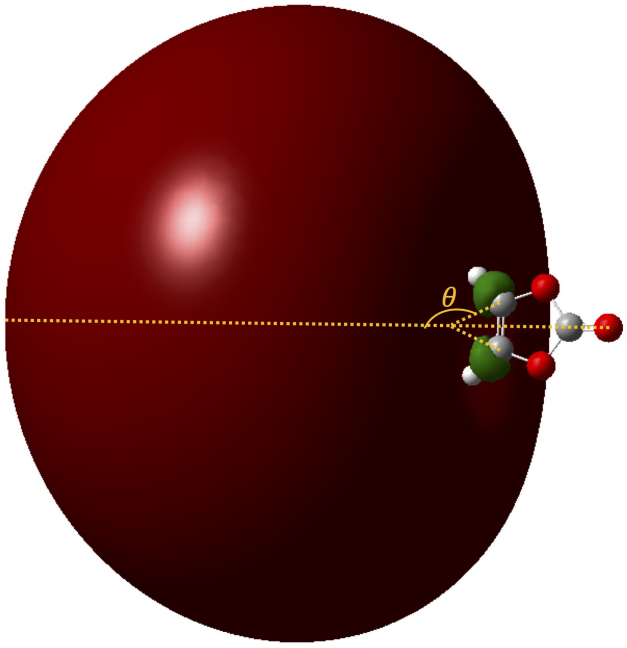

Figure 3.1: Visualization of the singly-occupied orbital of the $C_3H_2O_3$ anion as described by a UHF wave function. The isosurface value is taken as 0.003 e/Å^3.

of a trial wave function is propagated according to the imaginary time-dependent Schrödinger Equation

$$-\frac{\partial}{\partial\tau}\Psi(\vec{R},\tau) \quad = \quad \left(\hat{H}(\vec{R}) - E_T\right)\Psi(\vec{R},\tau) \tag{3.1}$$

where $\vec{R}$ denotes the real space coordinates of the system's electrons, τ denotes an imaginary time, $\Psi(\vec{R},\tau)$ denotes the time-dependent wave function, $\hat{H}$ is the real space Hamiltonian, and E_T is an arbitrary offset known as the reference energy. Solving this equation for large τ produces a distribution of walkers representative of the boson ground state wave function. To determine the fermion ground state wave function, the fixed-node approximation [7, 23] must be employed. Equation 3.1 is first recast into an integral equation that makes it amenable to Monte Carlo sampling

$$f(\vec{R},\tau) = \int G(\vec{R} \leftarrow \vec{R}', \tau - \tau') f(\vec{R}', \tau') d\vec{R}'. \tag{3.2}$$

Here, $f(\vec{R},\tau) = \Psi_T(\vec{R})\Psi(\vec{R},\tau)$ is the product of a trial wave function, $\Psi_T(\vec{R})$, and the sampled wave function, and $G(\vec{R} \leftarrow \vec{R}', \tau - \tau')$ is a Green's function describing the probability of moving from configuration $\vec{R}$ at time τ to a new configuration $\vec{R}'$ at time τ'. In the short-time approximation, the Green's function may be broken into

$$\begin{aligned} G(\vec{R} \leftarrow \vec{R}', \tau - \tau') &\approx \frac{1}{(2\pi\Delta\tau)^{3N/2}} e^{-\frac{[\vec{R}-\vec{R}'-\Delta\tau v(\vec{R}')]^2}{2\Delta\tau}} \\ &\times e^{-\frac{\Delta\tau}{2}[E_L(\vec{R})+E_L(\vec{R}')-2E_T]}, \end{aligned} \tag{3.3}$$

where $\Delta\tau \equiv \tau - \tau'$ and E_L is the local energy. The first exponential is the drift-diffusion Green's function, while the second exponential is the branching factor. In a typical DMC simulation, walkers sample the drift-diffusion Green's function for a new configuration and are then weighted by the branching term. In order to obtain a fermion ground state while preventing the walker weights from becoming negative and producing a sign problem, the fixed node approximation is invoked which precludes any walkers from crossing the nodal surface imposed by Ψ_T. Initial walker configurations are normally taken from VMC simulations [153, 175, 210].

All VMC and DMC simulations in this work were conducted using the CASINO

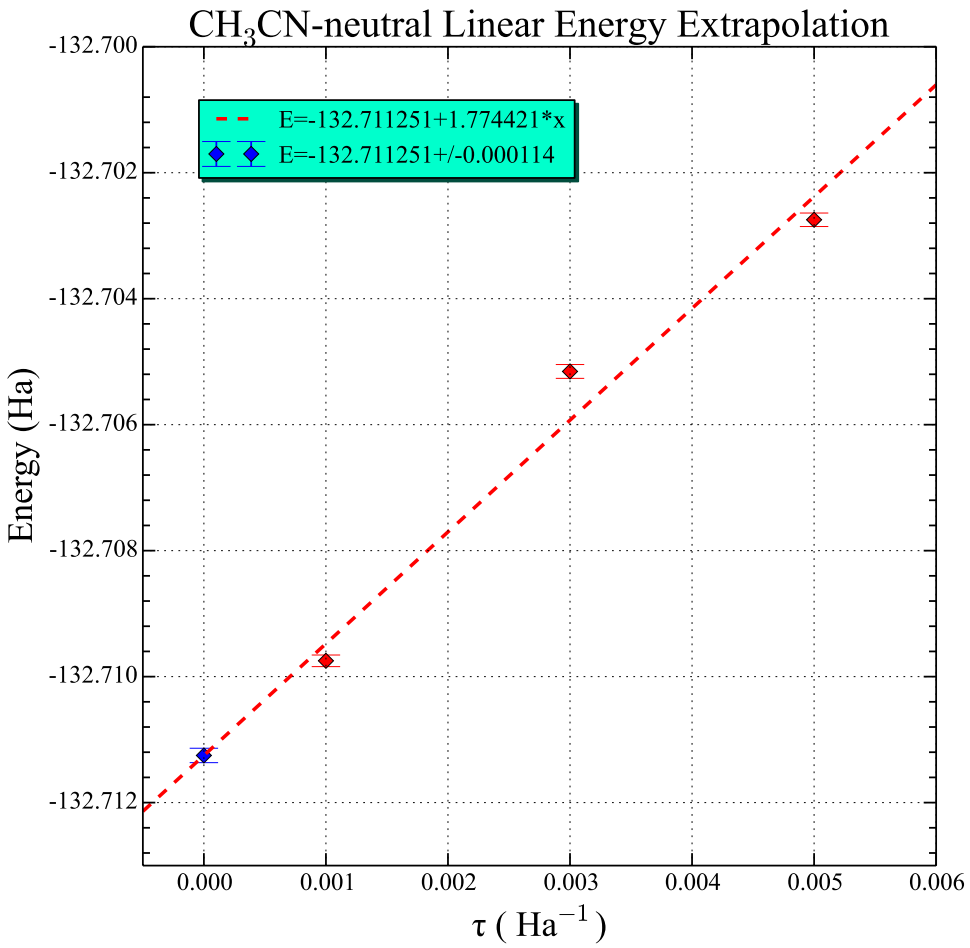

Figure 3.2: Extrapolation to zero time step of the DMC energy of CH_3CN. The calculations were preformed using an aug-cc-pvdz basis supplemented with diffuse $7s7p$ orbitals. RHF wave functions were provided as input into VMC calculations whose resulting Slater-Jastrow wave functions were employed as trial wave functions in the DMC calculations of the energies presented here.

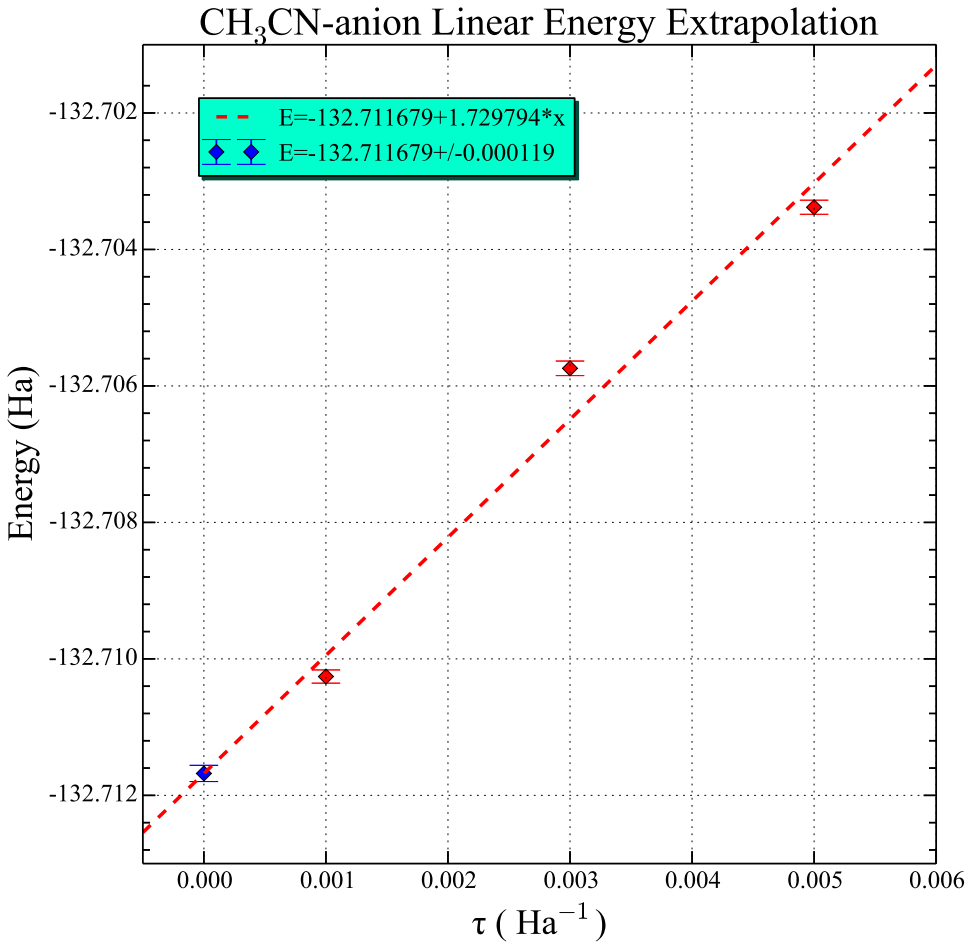

Figure 3.3: Extrapolation to zero time step of the DMC energy of CH_3CN anion. The calculations were preformed using an aug-cc-pvdz basis supplemented with diffuse $7s7p$ orbitals. UHF wave functions were provided as input into VMC calculations whose resulting Slater-Jastrow wave functions were employed as trial wave functions in the DMC calculations of the energies presented here.

Table 3.1: DMC values of the ground state energies (Hartree) of the neutral species at different time steps sizes (Hartree^{-1}) used in the energy extrapolation.

	$\Delta\tau = 0.005$	$\Delta\tau = 0.003$	$\Delta\tau = 0.001$
CH_2CHCN	-170.761627+/-0.000099	-170.764939+/-0.000090	-170.770537+/-0.000192
CH_3CN	-132.702747+/-0.000107	-132.705155+/-0.000110	-132.709749+/-0.000092
C_3H_2	-115.272672+/-0.000187	-115.275085+/-0.000178	-115.278096+/-0.000169
$C_3H_2O_3$	-341.056016+/-0.000241	-341.059574+/-0.000249	-341.071200+/-0.000328
	$\Delta\tau = 0.005$	$\Delta\tau = 0.001$	$\Delta\tau = 0.0007$
HCN	-93.395107+/-0.000093	-93.399181+/-0.000173	-93.399520+/-0.000180
	$\Delta\tau = 0.01$	$\Delta\tau = 0.005$	$\Delta\tau = 0.003$
SO	-473.365793+/-0.000113	-473.321900+/-0.000123	-473.302764+/-0.000309

package [153]. VMC calculations were performed in four sequential steps [43]. During the first step, the electron-electron (U) Jastrow parameters and cutoffs were optimized via variance minimization holding all electron-nuclear (X) terms constant. In the second step, X parameters and cutoffs were optimized holding the optimal U parameters and cutoffs from the previous step constant. The electron-nuclear and electron-electron parameters were then optimized simultaneously using variance minimization. Lastly, during the fourth and final step, the linear (i.e., not cutoffs) electron-nucleus and electron-electron parameters were optimized using energy-minimization. All VMC Jastrow optimization simulations were run for at least 240,000 time steps with 2350 walkers. For the DMC simulations, averages were obtained by sampling the configurations of 4650 walkers for 500,000 or more production steps, depending upon the magnitude of the error bars we aimed to achieve. In order to obtain DMC energies in the $\Delta\tau \to 0$ limit, DMC simulations were conducted with three different time step sizes (see Tables 3.1 and 3.2 for exact values) and then linearly extrapolated to yield the final values reported (see Figure 3.2 and 3.3 as an example). Charge density plots, as in Figure 3.4, were constructed from samples taken from the smallest time slice simulations of each species and visualized using the VESTA package [142].

Table 3.2: DMC values of the ground state energies (Hartree) of the anions (or neutral species plus an electron in the case of SO) at different time steps sizes (Hartree^{-1}) used in the energy extrapolation.

	$\Delta\tau = 0.005$	$\Delta\tau = 0.003$	$\Delta\tau = 0.001$
CH_2CHCN	-170.762150+/-0.000093	-170.765430+/-0.000118	-170.770631+/-0.000180
CH_3CN	-132.703381+/-0.000103	-132.705742+/-0.000107	-132.710259+/-0.000097
C_3H_2	-115.274067+/-0.000193	-115.276134+/-0.000172	-115.278942+/-0.000168
$C_3H_2O_3$	-341.057406+/-0.000248	-341.061047+/-0.000267	-341.071938+/-0.000332

	$\Delta\tau = 0.005$	$\Delta\tau = 0.001$	$\Delta\tau = 0.0007$
HCN	-93.395480+/-0.000084	-93.399462+/-0.000144	-93.399702+/-0.000188

	$\Delta\tau = 0.01$	$\Delta\tau = 0.005$	$\Delta\tau = 0.003$
SO	-473.373628+/-0.000093	-473.325033+/-0.000119	-473.304499+/-0.000287

3.2.4 Auxiliary Field Quantum Monte Carlo

Like DMC, AFQMC is a projector quantum Monte Carlo technique that applies a projection operator onto a trial wave function to obtain an approximation to the ground state wave function. What fundamentally distinguishes AFQMC from DMC is the fact that its imaginary time projection results in a random walk through a space of non-orthogonal Slater determinants [146, 235]. Because of its reliance upon Slater determinants, AFQMC shares many commonalities with conventional quantum chemistry methods, such as configuration interaction and coupled cluster methods, in many ways making it easier to apply to chemical systems. In particular, AFQMC trial wave functions may readily be constructed from Hartree Fock and Multiconfigurational Self-Consistent Field wave functions and makes use of the same one- and two-body integrals produced by standard quantum chemistry software packages [2, 3, 4, 5]. These benefits have made AFQMC an increasingly popular approach for modeling the electronic structure of a variety of atoms and molecules [2, 3, 4, 5, 104, 167, 203]. Because the details that underlie AFQMC have been presented mainly in Chapter 2, here we will only outline the *ab initio* Hamiltonian

we used for molecules.

$$
\begin{aligned}
\hat{H} &= \hat{T} + \hat{V} \\
&= \sum_{\alpha} \sum_{ij}^{N} t_{ij} \hat{c}_{i\alpha}^{\dagger} \hat{c}_{j\alpha} + \frac{1}{2} \sum_{\alpha,\beta} \sum_{i,j,k,l}^{N} V_{ijkl} \hat{c}_{i\alpha}^{\dagger} \hat{c}_{j\beta}^{\dagger} \hat{c}_{k\beta} \hat{c}_{l\alpha} \\
&= \sum_{\alpha} \sum_{ij}^{N} t_{ij} \hat{c}_{i\alpha}^{\dagger} \hat{c}_{j\alpha} - \frac{1}{2} \sum_{\alpha,\beta} \sum_{i,j,k,l}^{N} V_{ijkl} \hat{c}_{i\alpha}^{\dagger} \hat{c}_{j\beta}^{\dagger} \hat{c}_{l\alpha} \hat{c}_{k\beta} \\
&= \sum_{\alpha} \sum_{ij}^{N} t_{ij} \hat{c}_{i\alpha}^{\dagger} \hat{c}_{j\alpha} - \frac{1}{2} \sum_{\alpha,\beta} \sum_{i,j,k,l}^{N} V_{ijkl} \hat{c}_{i\alpha}^{\dagger} (\delta_{jl}\delta_{\alpha\beta} - \hat{c}_{l\alpha} \hat{c}_{j\beta}^{\dagger}) \hat{c}_{k\beta} \\
&= \sum_{\alpha} \sum_{ij}^{N} t_{ij} \hat{c}_{i\alpha}^{\dagger} \hat{c}_{j\alpha} - \frac{1}{2} \sum_{\alpha} \sum_{i,j,k}^{N} V_{ijkj} \hat{c}_{i\alpha}^{\dagger} \hat{c}_{k\alpha} + \frac{1}{2} \sum_{\alpha,\beta} \sum_{i,j,k,l}^{N} V_{ijkl} \hat{c}_{i\alpha}^{\dagger} \hat{c}_{l\alpha} \hat{c}_{j\beta}^{\dagger} \hat{c}_{k\beta},
\end{aligned}
\tag{3.4}
$$

where N is the number of the one-particle basis functions. As we can see here, spin symmetries were adopted when constructing the Hamiltonian and later we can break this symmetry by using trial wave functions. More detailes about how this Hamiltonian can be transformed to carry out the Hubbard-Stratonovich transformation can be found in Appendix A.

3.2.5 Correlated Sampling Auxiliary Field Quantum Monte Carlo

Correlated sampling has long been used in Variational, Diffusion, and Green's Function Monte Carlo methods [47, 55, 211, 221]. In all of these approaches, differences between two quantities normally computed separately using independently generated configurations are instead computed using the same set of configurations. For sufficiently similar systems, this can result in a systematic cancellation of error, which markedly reduces the variance associated with measured observables. The calculation of dipole-bound anion vertical binding energies involves energy differences

between two species with identical molecular geometries, and thus is an ideal chemical application for correlated sampling.

In AFQMC, the sampling recovers integrals over gaussian-type distributed auxiliary fields which are the source of statistical fluctuation. Thus correlated sampling in the context of AFQMC involves using the same set of auxiliary fields to propagate both the neutral and anionic species, while each species' respective trial wave function is utilized to independently implement the phaseless constraint. That said, the auxiliary fields x_α in Equation 2.12 will be generated for system one for each walker at each time step independently, but they will be copied to the paired walkers in system two at each time step. The two similar systems become correlated through this way, which preserves the similarity of sampling paths for two similar systems.

To preserve the maximal correlation between the walkers of the two species, we do not employ any standard population control techniques. And if the weight of one walker in system one becomes zero or negative, this walker and its paired walker in system two will both be killed to keep the optimal pairing between the two systems. Due to the statistical noise induced by the divergent walkers through propagation, simulations with a shorter propagation time but more simulation repeats are conducted to accumulate the observable averages. This eliminates another possible source of bias due to a finite walker population, and is feasible when sufficiently small statistical error bars can be achieved at short imaginary times. Correlated sampling will be most efficient when the Hamiltonian between two systems are the same. More detailed discussions of the method and treatments for various situations can be found in Reference [190].

In this work, auxiliary fields are correlated from the start of the simulations, and

measurements are performed following the protocol detailed in Reference [190]. In brief, a set of independent simulations are initialized, each with a unique random number seed, and after an initial equilibration period, the mean and standard error of the cumulative averages are computed among the repeats. Convergence is attained when this mean is visually observed to plateau, and when the statistical error falls below a target threshold. The $\Delta\tau \to 0$ limit is estimated via linear extrapolations using simulations performed at $\Delta\tau = .01$ and $\Delta\tau = .005$.

3.3 Results and Discussion

3.3.1 DMC Binding Energies

While DMC has been successfully employed to obtain valence and a handful of cluster [222, 227] dipole binding energies[3], here we analyze its performance on much more weakly-bound dipole-bound molecular anions. As an initial test, we examined whether DMC could faithfully predict whether a given species binds an extra electron or not. To this end, in addition to considering several species known to form dipole-bound anions, we also consider SO, a molecule with a dipole moment of 1.55 D, which is below the threshold required for binding. Our primary results are summarized in Table 3.3. Indeed, DMC calculations correctly predicted that all of the species studied, except SO, would form dipole-bound anions.

[3]The binding energies of the clusters previously studied were over an order of magnitude larger than those of the species analyzed in this work.

Table 3.3: EBEs and dipole moments of selected species from experiment and Self-Consistent Field [HF], Coupled Cluster [CCSD(T)], DMC, and C-AFQMC simulations.

normalsize

	Dipole Moment (D)	Electron Binding Energy (cm^{-1})				
		Experiment	ΔSCF[a]	CCSD(T)[a]	DMC[b]	C-AFQMC[c]
SO	1.55 [154]	NOT-BOUND	-3.84	-4.13	-308.20 ±70.82	-4.54 ± 0.64
HCN	2.98 [154]	13 [10]	11.00	7.44	46.17 ± 45.30	10.80 ± 2.95
CH_2CHCN	3.87 [154]	56 - 87 [35, 34]	43.30	61.87	106.63 ± 58.12	65.70 ± 11.03
CH_3CN	3.92 [154]	93 - 145 [35, 34]	50.83	103.00	93.83 ± 36.21	95.85 ± 9.73
C_3H_2	4.14 [63]	170 ± 50 [231]	54.61	162.08	151.22±64.25[d]	132.45 ± 9.43[e]
$C_3H_2O_3$	4.55 [154]	194 ± 24 [76]	103.13	163.31	213.98 ± 116.15	157.70 ± 17.96

[a] HF and CCSD(T) calculations were preformed using Gaussian09. [b] DMC calculations are based on UHF trial wave functions obtained from Gaussian 09 or GAMESS. [c] AFQMC calculations were based on UHF trial wave functions obtained from NWChem. [d] The DMC calculations on the C_3H_2 dipole-bound anion used a restricted open-shell Hartree Fock (ROHF) trial wave function. [e] To be consistent, the C-AFQMC calculations on the C_3H_2 dipole-bound anion were also based on an ROHF trial wave function.

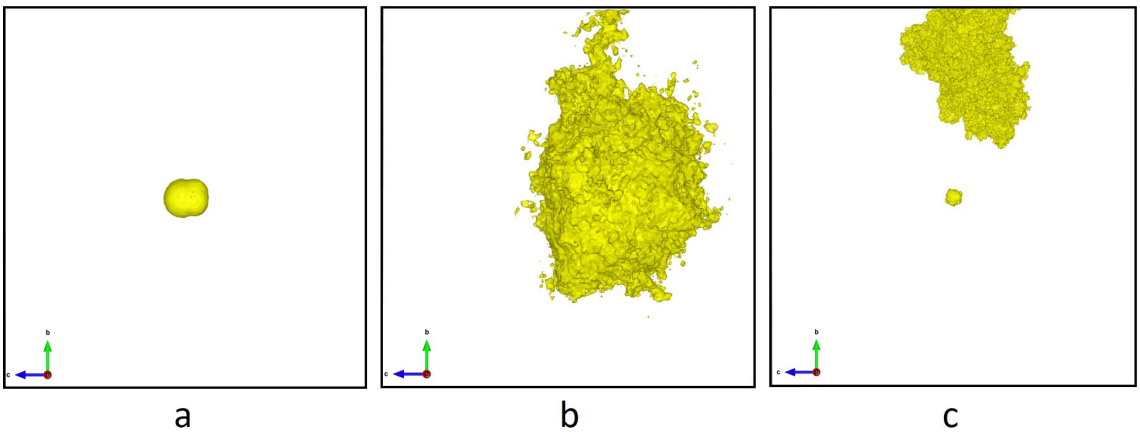

Figure 3.4: DMC charge densities of (a) neutral CH_3CN, (b) the CH_3CN anion, and (c) SO plus an extra electron. The isosurface values taken for each of these plots are 4×10^{-14} e/Å^3, 4×10^{-14} e/Å^3, and 1×10^{-20} e/Å^3, respectively. While the charge distribution of CH_3CN plus an excess electron given in (b) is characteristic of a dipole-bound anion, the distribution for SO plus its excess electron given in (c) is consistent with a neutral molecule and an unbound electron.

This is also borne out by DMC charge density plots. In Figure 3.4, the charge densities of neutral CH_3CN, the CH_3CN anion, and the SO molecule plus an extra electron are compared. While the DMC charge density for the neutral CH_3CN

molecule is highly localized in the molecular region, that of the anion is far more diffuse and protrudes out from the positive side of the dipole without any significant discontinuities, as expected for a dipole-bound species. The charge density plots of the other dipole-bound anions considered in this work manifest similar features and here I showed another example of $C_3H_2O_3$ in Figure 3.5. In stark contrast, the charge density of SO plus an extra electron consists of two disjoint contributions – one associated with the neutral molecule and a second representative of an additional unbound electron positioned more than 50 $\mathring{A}$ from the nucleus. These charge densities require roughly an order of magnitude less time to converge than the corresponding energies with error bars of the size given in Table 3.3.

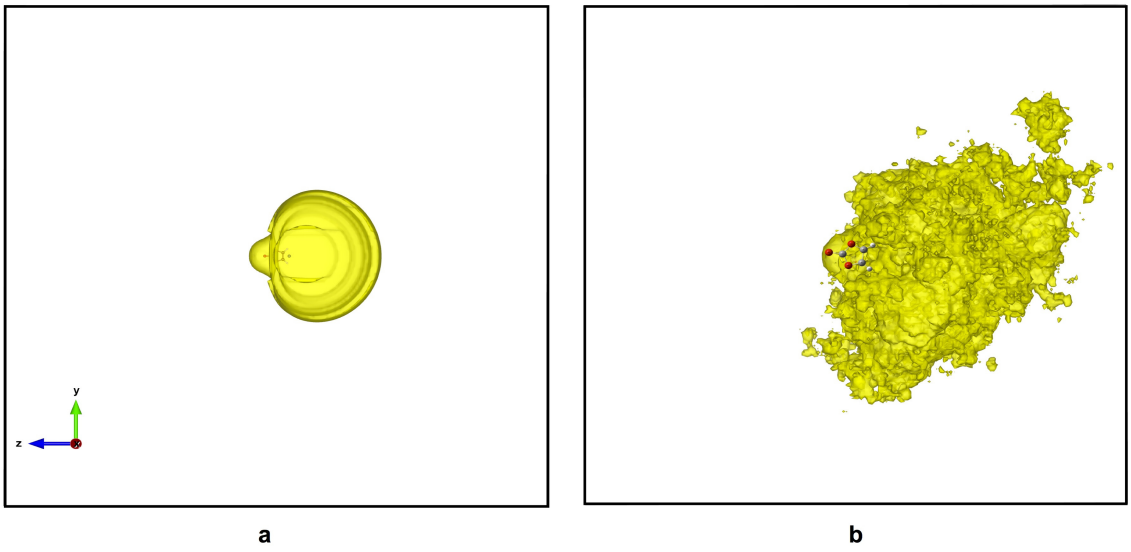

Figure 3.5: Charge density plots of the $C_3H_2O_3$ anion calculated using the (a) HF and (b) DMC methodologies. The isosurface value is taken as 3×10^{-6} e/Å^3 for HF and 1×10^{-13} e/Å^3 for DMC. Both methods showed a continuous and diffuse extra electron distribution.

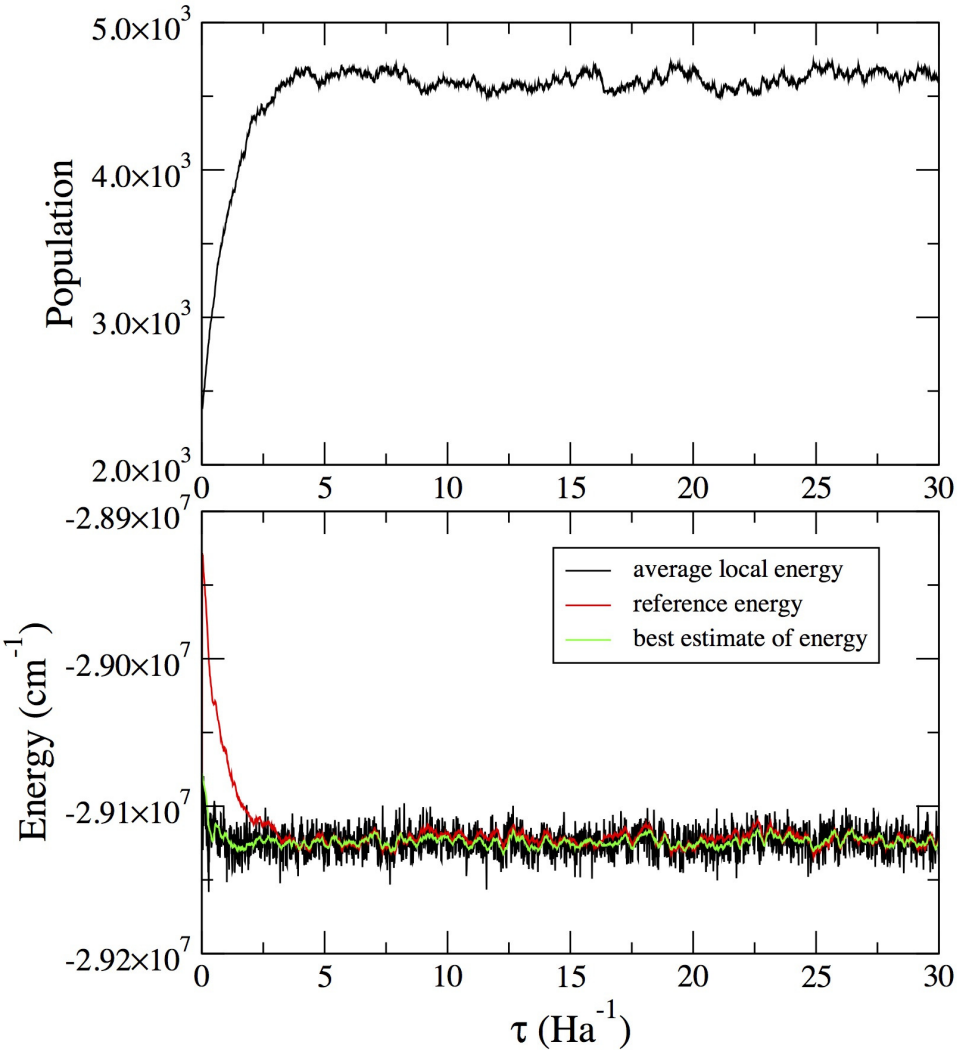

Figure 3.6: The time evolution of the DMC energy and walker population for the CH_3CN anion using $\tau = 0.01$ with 4650 walkers. Walkers were initialized with a UHF/aug-cc-pVDZ trial wave function with extra $7s7p$ orbitals. In the Figure, reference energy refers to E_T in Equation 3.1, the average local energy refers to the local energy averaged over walkers at a given imaginary time, and best estimate of the energy refers to the energy averaged over all equilibrium samples taken up to a certain imaginary time. The dramatic population increase at the beginning of the DMC calculations can be attributed to the difference between the VMC and DMC results. Note that, to achieve the error bars given in Table 3.3, the projection process continued for hundreds of thousands of iterations beyond the maximum imaginary time depicted here.

Interestingly, even though the fixed node error in the energies of the neutral and anion are greater in magnitude than the binding energy itself, DMC calculations using a single Slater determinant trial wave function appear to be able to provide semi-qualitatively accurate EBEs of dipole-bound anions. Obtaining quantitatively accurate EBEs with the DMC approach employed here would be too computationally demanding to be practical. As presented in Table 3.3, achieving DMC statistical error bars smaller than the binding energies can require hundreds of thousands to millions of DMC iterations, even starting from a well-optimized variational wave function. For example, as depicted in Figure 3.6, statistical fluctuations in the energy of the CH_3CN anion simulated with 4650 walkers hover around .3 Ha, or 65000 cm^{-1}, meaning that over 500,000 samples must be taken to achieve on the order of 100 cm^{-1} error bars. Thus, while DMC EBEs that agree with experimental and CCSD(T) calculations[4] can be retrieved from the noise, it is only with error bars that are still too large to make definitive statements and at great expense. More accurate trial wave functions [143, 161] and more efficient sampling would certainly improve matters, however, this inherent noise motivated us to consider other less noisy approaches.

3.3.2 Correlated Sampling AFQMC Binding Energies

One stochastic technique capable of not only scaling to the large dipole-bound anions to which we aspire, but doing so with a substantial reduction in statistical noise is correlated-sampling AFQMC. Given its success predicting atomization, ionization, and other differential energies, we applied C-AFQMC to each of the species studied using DMC.

[4]Here, we deem coupled cluster theory to be sufficiently accurate to serve as a benchmark against which we can compare our results.

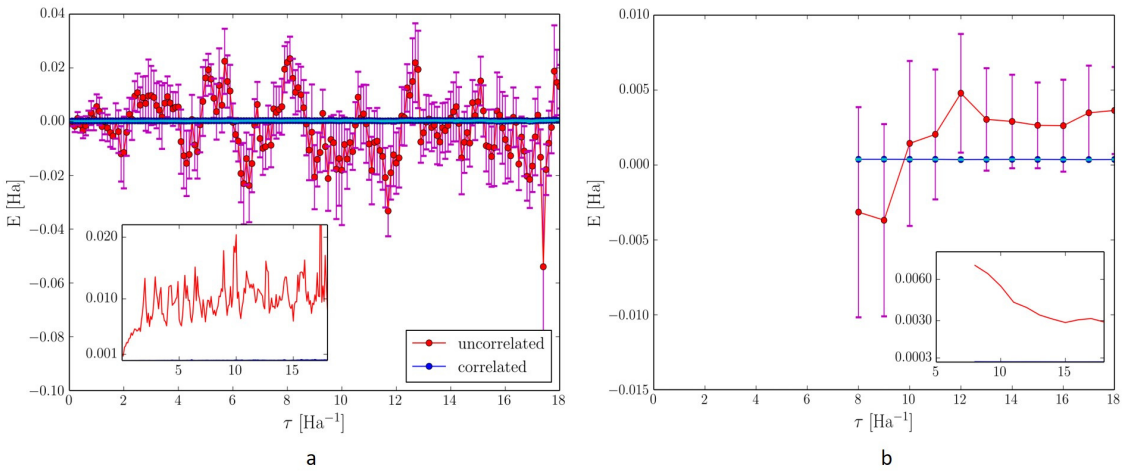

Figure 3.7: Comparison of C-AFQMC with a calculation in which the auxiliary fields are uncorrelated, for CH_3CN in the aug-cc-pvdz+$7s7p$ basis. We use an HF reference wave function, $\Delta\tau = 0.01$, 384 walkers per simulation and 17 repeated simulations. (a) Mean values of the electron binding energies (circles) among the repeats at each τ along the imaginary-time propagation; (b) Mean values of the cumulative averages taken for $\tau > 8$. The error bars give the corresponding standard errors (the standard deviation times $\frac{1}{\sqrt{N_r}}$, where N_r is the number of simulation repeats), and are plotted in the insets for clarity.

As shown in Table 3.3, C-AFQMC error bars are at least an order of magnitude smaller than DMC error bars using a similar number of samples (4650 walkers were used to obtain CH_3CN results in DMC and 384 walkers with 17 repeats were used in C-AFQMC), but using two orders of magnitude shorter projection time (2000 a.u. was used to obtain most of the DMC results presented, while only 20 a.u. was used to obtain the C-AFQMC results). The C-AFQMC results presented were moreover obtained starting from just Hartree Fock wave functions. One might question whether the source of this improvement stems from the AFQMC algorithm, given its high accuracy for other systems [3, 5, 203], or from the use of correlated sampling. Figure 3.7, which depicts the energy as a function of imaginary projection time for the CH_3CN molecule, demonstrates that the improvement may be

attributed to *both* sources. The uncorrelated AFQMC simulations are accompanied by statistical fluctuations on the order of 10^4 cm^{-1}, which are smaller than the 10^5 cm^{-1} fluctuations that accompany DMC (see Figure 3.6). Better yet, C-AFQMC calculations are accompanied by almost imperceptible statistical fluctuations on the order of 10^{-4} Ha (22 cm^{-1}). Thus, AFQMC's sampling innovations within the space of Slater determinants yield meaningful gains above DMC, yet it is the use of correlated sampling that yields, *by far*, the most significant improvements.

As shown in Table 3.3, C-AFQMC yields energies with sufficiently small error bars that meaningful comparisons can now be made against coupled cluster calculations and experiment. In general, the EBEs predicted by C-AFQMC are within error bars of both experimental and previous coupled cluster singles, doubles, and perturbative triples (CCSD(T)) calculations. This demonstrates that phaseless approximation errors are mild and that for dipole-bound anions AFQMC is as accurate as CCSD(T). The C_3H_2 anion, however, stands as one cautionary tale. For the C_3H_2 anion, we located two different UHF solutions as illustrated in Figure 3.8, neither of which proved suitable for trial functions in QMC calculations. For the two UHF solutions, one of which had sizable spin contamination, and the other of which, while displaying no spin contamination, had an unphysical charge distribution, with the charge density of the neutral core shifting in an unphysical manner in response to the excess electron. DMC calculations using the unphysical UHF trial wave function (*i.e.*, that without spin contamination) encountered convergence issues. Using the same trial wave function, C-AFQMC calculations converged, but gave an EBE of 113.31 $\pm$ 16.76 cm^{-1}, significantly smaller than the CCSD(T) value of 162 cm^{-1}. For this reason, we employed a spin-restricted HF trial function for the anion (Figure 3.8).

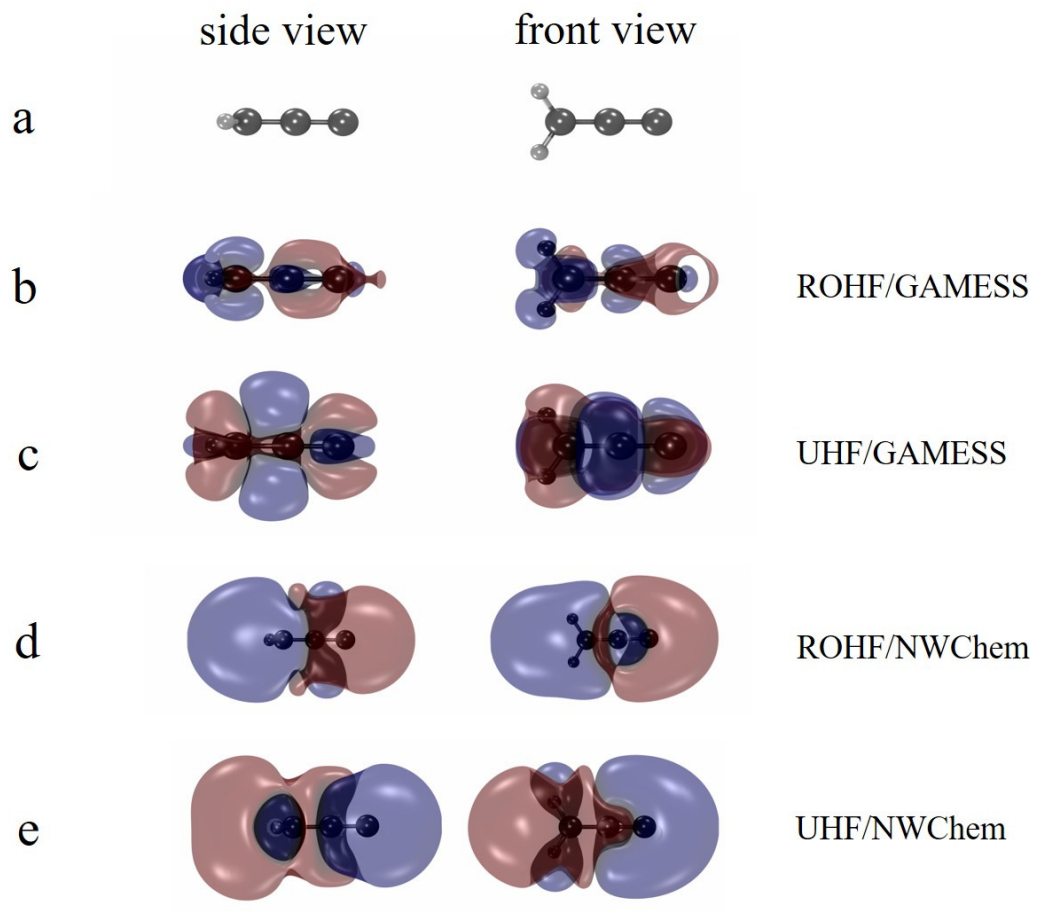

Figure 3.8: Change density differences between the C_3H_2 anion and the neutral excluding charge density representative of the excess electron from UHF and ROHF calculations performed in GAMESS and NWChem. Molecules in the left column are depicted from a side view; those in the right column are depicted from a front view. (a) Molecular geometries. Charge density differences between: (b) ROHF wave functions computed in GAMESS, (c) UHF wave functions computed in GAMESS, (d) ROHF wave functions computed in NWChem, and (e) UHF wave functions computed in NWChem. The isosurface value used in all cases is 0.0001 e/Å^3. Images are plotted using ORBKIT [87], cclib [159], and VMD [97].

These calculations gave a DMC EBE of 151.22 ± 64.25 cm^{-1} and a C-AFQMC EBE of 132.45 ± 9.43 cm^{-1}, in closer agreement with the CCSD(T) value. This example suggests that care must be taken when selecting trial wave functions for and ultimately simulating larger molecules that may have many competing low-lying states. It should also be noted that our simulations could do a better job of capturing dynamic correlation. While we currently use carefully selected diffuse functions tailored to describe the extended orbitals of the dipole-bound anions, a more accurate description of the electron cusp regions can be attained through the use of larger basis sets which contain functions of higher angular momentum. For small molecules, one could also use explicitly correlated methods like R12/F12 [14] and canonical transcorrelation [155] techniques.

3.4 Conclusions

In this work, we have demonstrated that low-scaling QMC methods, and in particular, C-AFQMC, are capable of resolving the fine energy differences required to accurately predict electron binding energies of dipole-bound anions. Electron binding energies within wave numbers of previous coupled cluster and experimental results were obtained for the HCN, CH_2CHCN, CH_3CN, C_3H_2, and $C_3H_2O_3$ molecules studied here. Given these methods' inherent approximations for controlling the sign problem, the calculations performed in this work lie just within the realm of applicability of QMC methods, and therefore attest to the fundamental accuracies attainable using modern stochastic approaches. Our results demonstrate that while uncorrelated DMC and AFQMC methods can *qualitatively* describe dipole-bound species, only correlated sampling techniques such as C-AFQMC are capable of achieving *quantitative* accuracy.

These findings moreover pave the way toward using stochastic methods to study the much larger polycyclic aromatic hydrocarbons (PAH) [219] and carbon chain anions [213] thought to contribute to the diffuse interstellar bands, as well as other weakly-bound species, including correlation-bound anions [218, 220] and weakly bound clusters [232], whose size puts them beyond reach of most high accuracy methods. These larger species may contain a mixture of valence- and dipole-bound states of different symmetries, which posed problems for this initial work. However, both recent DMC and AFQMC studies have suggested paths forward based upon incorporating key symmetries into the trial wave function [166, 185, 186], the propagators [192], or both. These techniques may also enable studies of excited electronic and vibrational states of similar species, which are of central importance to experimental explorations that typically obtain full spectra, not just single energy differences [240].

The success of C-AFQMC in this work [190] along with the many possibilities our efforts open up beckons for the further development of correlated DMC methods capable of resolving the molecular energy differences that lie at the heart of all chemical processes within modern DMC packages. If stochastic methods are to truly attain their long aspirational and recently more practicable goal of making meaningful chemical predictions, correlated sampling should be high on the list of development priorities.

Chapter Four

Auxiliary Field Quantum Monte Carlo for Multiband Hubbard Kanamori Model

4.1 Introduction

Since the unanticipated discovery of high-temperature superconductivity in the cuprates, the single-band Hubbard model [96] has been the focus of an unparalleled level of theoretical scrutiny and associated algorithmic development [67, 122, 124, 184]. Nevertheless, most materials exhibiting strong correlation, including most transition metal oxides [119, 120, 134] as well as the pnictides [81, 194, 230], fullerides [156, 157], and chalcogenides [194, 205, 230] possess multiple bands that cross their Fermi levels and are therefore fundamentally multi-band in nature [60]. In recent years, it has become increasingly evident that some of the most significant effects in such multi-band materials stem from Hund's coupling [81, 101, 230]. According to Hund's rules, electrons favor maximizing their total spin by first occupying different, degenerate orbitals with parallel spins; only after the parallel spins fill all available orbitals do electrons then begin to doubly occupy the same orbitals [60]. As such, the effective Coulomb repulsion among electrons in a half-filled shell is increased due to Hund's rules, while that at any other filling is decreased. Hund's effects therefore drive half-filled d- and f-electron materials closer to a Mott transition for a given Coulomb repulsion, yet drive non-half-filled materials away from a Mott transition while also increasing the correlation within their metallic phases. The consequences of these effects are perhaps best illustrated in $4d$ transition metal oxides that have more than a single electron or hole in their $4d$ shells [33, 51, 78, 113]. Unlike their rhodate counterparts, which possess a single hole in their shells, many ruthenates and molybdenates exhibit substantial mass enhancements [98], unexpected Mott Insulator transitions [62, 125, 206], novel quantum phase transitions [64], and even superconducting phases [132] – all of which may be attributed to Hund's physics.

Despite both the prevalence and importance of Hund's effects, they remain

a challenge to model. Most analytical and numerical treatments revolve around solving a multi-band Hubbard model, most often the Hubbard-Kanamori (HK) model [107], containing a mixture of kinetic, Coulomb U, and Hund's J terms. Although analytical studies have been performed [100, 109, 110, 131, 174], just as in the case of the single-band Hubbard model containing a repulsive U term [122, 239], accurate treatments of these models necessitate methods capable of treating strong correlation non-perturbatively. However, because these models possess significantly larger state spaces and involve additional pair-hopping and Hund's exchange terms, they are often even more difficult to treat than the Hubbard model.

Due to the complicated interactions involved, there is no general analytical solution for these problems. Thus, numerical treatments are in high demand. To date, most numerical studies of multi-band models have employed Dynamical Mean Field Theory (DMFT) [59, 140] either on its own or in combination with Density Functional Theory (DFT) [8] because of DMFT's ability to treat band and atomic effects on equal footing by self-consistently solving an impurity problem within a larger bath. DMFT has been very successful at mapping out multi-band phase diagrams at finite temperatures [32, 33, 62, 78, 79, 99, 225]. Nevertheless, DMFT is fundamentally limited by the accuracy and scaling of its impurity model solver. Some DMFT studies rely upon exact diagonalization (ED) to solve their impurity models, yet the computational cost of ED grows exponentially with the number of bands involved, thus thwarting its application to many-band models. Some DMFT algorithms employ continuous-time quantum Monte Carlo (CTQMC) [176] to solve their impurity models. CTQMC can solve larger impurity models than ED, but is still hampered by the sign problem, an exponential decrease in the signal to noise ratio observed in stochastic simulations [127], in certain parameter regimes and low temperature calculations remain difficult [68]. A method that can accurately

simulate larger system sizes at lower temperatures is thus in need.

One suite of techniques particularly well-suited for studying the large state spaces inherent to multi-band models are quantum Monte Carlo (QMC) techniques [50, 146]. Both finite temperature QMC methods, including the CTQMC [68] and Hirsch-Fye QMC [90] algorithms that have been employed as impurity solvers within DMFT, and ground state [144, 145] QMC algorithms have been developed and applied to the multi-band Hubbard model. Nonetheless, the Hund's terms of the HK Hamiltonian have posed challenges for all of these methods. This is because Hund's terms are not readily expressed as products of density operators and are therefore not readily amenable to standard QMC transformations. Straightforward decoupling of the exchange and pair hopping terms leads to a severe sign problem [84]. Attempts have therefore been made to simplify the Hund's contribution to the Hamiltonian to make it more palatable to QMC methods by constraining its direction to the z-axis [77, 84], but such treatments often fail to properly capture the model's expected physics. Several Hund's-specific transformations have been proposed, including a discrete transformation by Aoki [179, 180] and a continuous transformation by Imada [144, 145]. Nevertheless, these transformations ultimately do not eliminate the sign problem and are limited to parameter regimes with only high signal to noise ratios. These algorithmic constraints obscure our fundamental understanding of multi-band physics.

In this paper, we present an Auxiliary Field Quantum Monte Carlo (AFQMC) framework especially suited for the study of ground state multi-band Hubbard models and demonstrate its accuracy over a range of realistic parameters using different signal-preserving approximations and trial wave functions. Key to our approach is the strategic use of two forms of both the continuous and discrete Hubbard-Stratonovich (HS) Transformations to decouple the Hund's term: a charge

decomposition for negative values of the Hund's coupling parameter, and a spin decomposition for positive values of the Hund's coupling parameter. We also employ an unconventional form of importance sampling in which we shift propagators instead of auxiliary fields so as to enable importance sampling of discrete transformed propagators. This enables us to combine importance sampling with *both* discrete and continuously transformed propagators. Unlike previous works, we furthermore utilize flexible Generalized Hartree-Fock (GHF) trial wave functions which enable us to calculate highly accurate background subtraction terms and apply highly accurate sign/phase constraints. Altogether, we find that these improvements yield promising results for a variety of HK model benchmarks. Although the algorithm presented is designed for the ground state, it can easily be adapted for use in finite temperature methods [126, 233]. Our algorithm therefore paves the way to high accuracy modeling of the low temperature physics of a wide range of multi-band models and materials over a dramatically larger portion of the phase diagram.

The remainder of the paper is organized as follows. In Section 4.2, we outline the HK model, summarize the key features of the AFQMC method, and describe how the conventional AFQMC technique may be modified to best treat the HK Hamiltonian. In Section 4.3, we then present benchmarks of our method's performance within different parameter regimes, using different trial wave functions and employing different approximations on two- and three-band HK models for which ED results may be obtained. Towards the end of this section, we also demonstrate the accuracy with which our techniques can predict the charge gaps and magnetic ordering of two-dimensional lattice models beyond the reach of most other techniques. We conclude with a discussion of the broader implications of this work and future directions in Section 4.4.

4.2 Methods

4.2.1 Hubbard Kanamori Model Hamiltonian

The HK model is a multi-band version of the Hubbard model designed to account for the competition between the spin and orbital degrees of freedom observed in the physics of d- and f- electron material [60, 107]. In order to accomplish this, the model includes not only standard Hubbard on-site density-density interactions, but also inter-orbital (band) density, exchange, and pair hopping terms. The full HK Hamiltonian, written as generally as possible, reads

$$\hat{H}_{HK} \equiv \hat{H}_1 + \hat{H}_2 \equiv \hat{H}_1 + \hat{H}_U + \hat{H}_J, \tag{4.1}$$

where

$$\hat{H}_1 = \sum_{im\sigma} \sum_{jm'\sigma'} t^{\sigma\sigma'}_{im,jm'} \hat{c}^\dagger_{im\sigma} \hat{c}_{jm'\sigma'}, \tag{4.2}$$

$$\begin{aligned} \hat{H}_U &= \sum_{i,m} U_{im} \hat{n}_{im\uparrow} \hat{n}_{im\downarrow} + \sum_{i,m\neq m'} U'_{imm'} \hat{n}_{im\uparrow} \hat{n}_{im'\downarrow} \\ &+ \sum_{i,m<m',\sigma} (U'_{imm'} - J_{imm'}) \hat{n}_{im\sigma} \hat{n}_{im'\sigma}, \end{aligned} \tag{4.3}$$

and

$$\begin{aligned} \hat{H}_J = \sum_{i,m\neq m'} J_{imm'} (&\hat{c}^\dagger_{im\uparrow} \hat{c}^\dagger_{im'\downarrow} \hat{c}_{im\downarrow} \hat{c}_{im'\uparrow} \\ &+ \hat{c}^\dagger_{im\uparrow} \hat{c}^\dagger_{im\downarrow} \hat{c}_{im'\downarrow} \hat{c}_{im'\uparrow} + H.c.). \end{aligned} \tag{4.4}$$

In the above, $\hat{c}^\dagger_{im\sigma}(\hat{c}_{im\sigma})$ creates (annihilates) an electron with spin σ in band m at site i. $\hat{n}$ denotes the number operator and $\hat{n}_{im\uparrow}$, for example, represents the number

of spin-up electrons at site i in band m. $\hat{H}_1$ contains all one-body contributions to the Hamiltonian, including terms parameterized by the constants $t^{\sigma\sigma'}_{im,jm'}$ that describe the hopping of electrons in different bands between sites i and j and the spin-orbit coupling common within realistic materials. $\hat{H}_2$ denotes the collection of all two-body operators. $\hat{H}_U$ contains all density-density interactions, including the intraband (U) and interband (U') Coulomb interactions, and the z- (or Ising) component of the Hund's coupling. In contrast, $\hat{H}_J$ contains all of the terms that cannot be written as density-density interactions, which consist of the x- and y-components (spin-exchange) of the Hund's coupling, $(\hat{c}^\dagger_{im\uparrow}\hat{c}^\dagger_{im'\downarrow}\hat{c}_{im\downarrow}\hat{c}_{im'\uparrow} + H.c.)$, as well as the pair-hopping interaction $(\hat{c}^\dagger_{im\uparrow}\hat{c}^\dagger_{im\downarrow}\hat{c}_{im'\downarrow}\hat{c}_{im'\uparrow} + H.c.)$, in which two electrons in a given band transfer as a pair to another band. J denotes the Hund's coupling constant. Note that our formalism is general and allows for band- and site-dependent U, U', and J constants.

4.2.2 Modified Hubbard Kanamori Model Hamiltonian

In order to facilitate programming and the generalization of this HK Hamiltonian into a form in which all coupling constants are independent, we map the Hamiltonian given by Equations 4.1 - 4.4 into a one-band model whose terms only depend upon their band indices. If we now let i and j denote superindices that combine both

lattice site and band information, then

$$\begin{aligned}\hat{H} &= \hat{H}_1 + \hat{H}_2 \\ &= \sum_{ij,\sigma\sigma'} t_{ij}^{\sigma\sigma'} \hat{c}_{i\sigma}^{\dagger} \hat{c}_{j\sigma'} \\ &+ \sum_{i} U^{i} \hat{n}_{i\uparrow} \hat{n}_{i\downarrow} \\ &+ \sum_{i<j} U_1^{ij} (\hat{n}_{i\uparrow} \hat{n}_{j\downarrow} + \hat{n}_{i\downarrow} \hat{n}_{j\uparrow}) \\ &+ \sum_{i<j} U_2^{ij} (\hat{n}_{i\uparrow} \hat{n}_{j\uparrow} + \hat{n}_{i\downarrow} \hat{n}_{j\downarrow}) \\ &+ \sum_{i<j} J^{ij} (\hat{c}_{i\uparrow}^{\dagger} \hat{c}_{j\downarrow}^{\dagger} \hat{c}_{i\downarrow} \hat{c}_{j\uparrow} + \hat{c}_{i\uparrow}^{\dagger} \hat{c}_{i\downarrow}^{\dagger} \hat{c}_{j\downarrow} \hat{c}_{j\uparrow} \\ &+ \hat{c}_{j\uparrow}^{\dagger} \hat{c}_{i\downarrow}^{\dagger} \hat{c}_{j\downarrow} \hat{c}_{i\uparrow} + \hat{c}_{j\uparrow}^{\dagger} \hat{c}_{j\downarrow}^{\dagger} \hat{c}_{i\downarrow} \hat{c}_{i\uparrow}).\end{aligned} \tag{4.5}$$

$t_{ij}^{\sigma\sigma'}$ describes the hopping and spin-orbit coupling between different sites and bands. In keeping with the $\sum_{i,m<m'}$ and $\sum_{i,m\neq m'}$ summations in Equations 4.3 and 4.4, $\sum_{i<j}$ only sums over index combinations that reference different bands on the same site. In this modified HK Model, the U term describes density-density interactions only between electrons with opposite spins in the same band, the U_1 term describes interactions between electrons with opposite spins in different bands on the same site, the U_2 term describes interactions between electrons with parallel spins in different bands on the same site, and the J term describes spin-exchange and pair hopping interactions on the same site. Thus, in going from Equations 4.3 and 4.4 to Equation 4.5, the original U' term has become the U_1 term, the original $(U' - J)$ term has become the U_2 term, and the J term has been re-expressed. Using Equation 4.5, we map a multi-band model into a single-band model in which the number of lattice sites has been enlarged into the number of bands. Since there is no explicit band index in our model, we can deal with any number of bands as long as the mapping is done correctly.

4.2.3 Overview of AFQMC

In the remainder of this work, AFQMC will be employed to obtain accurate numerical solutions to the HK Model. AFQMC is a quantum many-body method that solves the ground state Schrodinger Equation by randomly sampling an overcomplete space of non-orthogonal Slater determinants [234, 235, 236] and has consistently been demonstrated to be among the most accurate of modern many-body methods for modeling the Hubbard model over a wide range of parameter regimes [26, 27, 122, 192, 239]. At its heart, AFQMC is an imaginary-time projection quantum Monte Carlo technique that applies a projection operator, $e^{-\beta\hat{H}}$, onto an initial wave function, $|\Psi_I\rangle$,

$$|\Psi_0\rangle \propto \lim_{\beta\to\infty}\left(e^{-\beta\hat{H}}\right)|\Psi_I\rangle. \tag{4.6}$$

In the limit of infinite imaginary projection time ($\beta \to \infty$), it converges to the ground state wave function, $|\Psi_0\rangle$, as long as the initial wave function is not orthogonal to the ground state wave function. Because the projection operator cannot be evaluated for large values of β, it is discretized into $n = \beta/\Delta\tau$ smaller time slices for which it can be evaluated

$$|\Psi_0\rangle \propto \lim_{n\to\infty}\left(e^{-\Delta\tau\hat{H}}\right)^n|\Psi_I\rangle, \tag{4.7}$$

and the projection is carried out iteratively as follows

$$|\Psi^{(n+1)}\rangle = e^{-\Delta\tau\hat{H}}|\Psi^{(n)}\rangle. \tag{4.8}$$

For sufficiently small $\Delta\tau$, the projection operator may be factored into one- and two-body pieces via Suzuki-Trotter Factorization [207, 212]

$$e^{-\Delta\tau\hat{H}} \approx e^{-\Delta\tau\hat{H}_1/2} e^{-\Delta\tau\hat{H}_2} e^{-\Delta\tau\hat{H}_1/2}. \tag{4.9}$$

The two-body propagator may be further decomposed into the four terms given in Equation 4.5

$$\begin{aligned} e^{-\Delta\tau\hat{H}_2} &\approx e^{-\Delta\tau\hat{H}_U} e^{-\Delta\tau\hat{H}_{U_1}} e^{-\Delta\tau\hat{H}_{U_2}} e^{-\Delta\tau\hat{H}_J} \\ &= e^{-\Delta\tau\sum_i U^i \hat{n}_{i\uparrow}\hat{n}_{i\downarrow}} e^{-\Delta\tau\sum_{i<j} U_1^{ij}(\hat{n}_{i\uparrow}\hat{n}_{j\downarrow}+\hat{n}_{i\downarrow}\hat{n}_{j\uparrow})} \\ &\quad e^{-\Delta\tau\sum_{i<j} U_2^{ij}(\hat{n}_{i\uparrow}\hat{n}_{j\uparrow}+\hat{n}_{i\downarrow}\hat{n}_{j\downarrow})} \\ &\quad e^{-\Delta\tau\sum_{i<j} J^{ij}(\hat{c}^\dagger_{i\uparrow}\hat{c}^\dagger_{j\downarrow}\hat{c}_{i\downarrow}\hat{c}_{j\uparrow}+\hat{c}^\dagger_{i\uparrow}\hat{c}^\dagger_{i\downarrow}\hat{c}_{j\downarrow}\hat{c}_{j\uparrow}+H.c.)}. \end{aligned} \tag{4.10}$$

A time step extrapolation is needed to make sure the Trotter error is negligible in the Monte Carlo simulation.

4.2.4 Hubbard-Stratonovich Transformation of the Modified Hubbard Kanamori Hamiltonian

According to Thouless's Theorem [209], acting the exponential of a one-body operator on a determinant results in another determinant, reducing the process of projecting a one-body operator onto the wave function into standard matrix multiplication. Nevertheless, no such theorem applies to exponentials of two-body operators, which necessitates re-expressing these operators into integrals over one-body operators using the so-called Hubbard-Stratonovich transformation [95].

In order to transform the two-body propagator given by Equation 4.10, both

discrete [66, 88] and continuous [16] HS transformations need to be performed. The U, U_1, and U_2 terms are products of density operators, much like the single-band Hubbard model U term, and may therefore be decomposed using discrete transformations. For $\alpha < 0$, where α may denote U, U_1, or U_2, it is usually better to use the discrete charge decomposition

$$e^{-\Delta\tau\alpha\hat{n}_1\hat{n}_2} = e^{-\Delta\tau\alpha(\hat{n}_1+\hat{n}_2-1)/2} \sum_{x=\pm1} \frac{1}{2} e^{\gamma x(\hat{n}_1+\hat{n}_2-1)}, \tag{4.11}$$

where $\cosh(\gamma) = e^{-\Delta\tau\alpha/2}$, while for $\alpha > 0$, it is usually better to use the spin decomposition

$$e^{-\Delta\tau\alpha\hat{n}_1\hat{n}_2} = e^{-\Delta\tau\alpha(\hat{n}_1+\hat{n}_2)/2} \sum_{x=\pm1} \frac{1}{2} e^{\gamma x(\hat{n}_1-\hat{n}_2)}, \tag{4.12}$$

where $\cosh(\gamma) = e^{\Delta\tau\alpha/2}$. In both Equations 4.11 and 4.12, x represents the namesake auxiliary field that may assume the discrete values of $+1$ or -1. For the subsequent discussion, note that the charge decomposition is so named because it produces a one-body propagator involving the sum of $\hat{n}_1 + \hat{n}_2$, which would be equivalent to the charge on a site if 1 represented an up and 2 a down spin on that site. Along similar lines, the spin decomposition is so named because it involves the difference between $\hat{n}_1$ and $\hat{n}_2$, which would represent the spin on a site under the same assumptions.

Because $\hat{H}_J$ contains terms that are not simple products of density operators, decomposing it is a much more challenging task. Past attempts have either neglected or simplified $\hat{H}_J$ [77, 84]. Several techniques have employed exact decompositions [144, 179, 180], but all such decompositions are accompanied by a sign problem that thwarts explorations of wide swaths of the phase diagram. Unlike these past attempts, in the following, we define a unique decomposition that can be employed in both continuous and discrete transformations, and accompany it by importance sampling that first mitigates and the constrained path and phaseless

approximations that subsequently eliminate the sign and phase problems. As part of our decomposition of $e^{-\Delta\tau\hat{H}_J}$, we first re-expressed $\hat{H}_J$ in terms of squares of one-body operators. Let

$$\hat{\rho}_{ij} \equiv \sum_{\sigma} (\hat{c}^{\dagger}_{i\sigma}\hat{c}_{j\sigma} + \hat{c}^{\dagger}_{j\sigma}\hat{c}_{i\sigma}). \tag{4.13}$$

Then,

$$\hat{\rho}^2_{ij} = \sum_{\sigma\sigma'} (\hat{c}^{\dagger}_{i\sigma}\hat{c}_{j\sigma} + \hat{c}^{\dagger}_{j\sigma}\hat{c}_{i\sigma})(\hat{c}^{\dagger}_{i\sigma'}\hat{c}_{j\sigma'} + \hat{c}^{\dagger}_{j\sigma'}\hat{c}_{i\sigma'}), \tag{4.14}$$

and $\hat{H}_J$ may be re-expressed as (see Supplemental Materials Section at IA for more details about the deduction)

$$\begin{aligned}
\hat{H}_J &= \sum_{i<j} J^{ij} (\hat{c}^{\dagger}_{i\uparrow}\hat{c}^{\dagger}_{j\downarrow}\hat{c}_{i\downarrow}\hat{c}_{j\uparrow} + \hat{c}^{\dagger}_{i\uparrow}\hat{c}^{\dagger}_{i\downarrow}\hat{c}_{j\downarrow}\hat{c}_{j\uparrow} + H.c.) \\
&= \sum_{i<j} \frac{J^{ij}}{2} [\hat{\rho}^2_{ij} - \sum_{\sigma} (\hat{n}_{i\sigma} + \hat{n}_{j\sigma} - \hat{n}_{i\sigma}\hat{n}_{j\sigma} - \hat{n}_{j\sigma}\hat{n}_{i\sigma})] \\
&= \sum_{i<j} \frac{J^{ij}}{2} \hat{\rho}^2_{ij} - \sum_{i<j,\sigma} \frac{J^{ij}}{2} (\hat{n}_{i\sigma} + \hat{n}_{j\sigma}) + \sum_{i<j,\sigma} J^{ij} \hat{n}_{i\sigma}\hat{n}_{j\sigma}.
\end{aligned} \tag{4.15}$$

The second term of Equation 4.15 consists of one-body operators and can be combined with the other one-body operators into $\hat{H}_1$. The third term consists of a product of density operators and can therefore be transformed according to either Equations 4.11 or 4.12. The first term, however, consists of a square that cannot be resolved into products of density operators. In general, the two-body term can be decoupled via either a discrete [173] or a continuous [95] Hubbard Stratonovich transformation. A continuous HS transformation was employed based on previous experience [192] that the statistical errors that accompany transformations with near optimal background subtraction terms have substantially smaller slopes as a function of projection time than the errors that accompany discrete transformations without any background subtraction. In general, the continuous HS transformation may be

written as

$$e^{-\Delta\tau\hat{A}^2/2} = \int dx \frac{1}{\sqrt{2\pi}} e^{-x^2/2} e^{x\sqrt{-\Delta\tau}\hat{A}}, \tag{4.16}$$

where $\hat{A}$ represents any one-body operator and x denotes an auxiliary field, as before. Letting $\hat{A} \equiv \hat{\rho}_{ij}$, it follows that the most obvious way to transform the exponential formed from the first term of Equation 4.15 is using the charge decomposition

$$\begin{aligned} & e^{-\Delta\tau \sum\limits_{i<j} \frac{J^{ij}}{2} [\sum\limits_{\sigma} (\hat{c}^{\dagger}_{i\sigma}\hat{c}_{j\sigma} + \hat{c}^{\dagger}_{j\sigma}\hat{c}_{i\sigma})]^2} \\ & = \prod_{i<j} \int dx_{ij} \frac{1}{\sqrt{2\pi}} e^{-x_{ij}^2/2} e^{x_{ij}\sqrt{-\Delta\tau J^{ij}} [\sum\limits_{\sigma} (\hat{c}^{\dagger}_{i\sigma}\hat{c}_{j\sigma} + \hat{c}^{\dagger}_{j\sigma}\hat{c}_{i\sigma})]}. \end{aligned} \tag{4.17}$$

As long as $J^{ij} < 0$ for all i, j, all of the propagators produced by this transformation will be real, as is desirable within AFQMC simulations. However, if any of the J^{ij} are greater than 0, $\sqrt{-\Delta\tau J^{ij}}$ will be complex resulting in a complex propagator that immediately introduces a complex phase into simulations. To prevent complexity from being introduced into the operators, in certain cases, we take a cue from the discrete case and define a continuous spin decomposition that involves the difference between spin up and down operators. Let

$$\hat{\rho}_{ij} = \sum_{\sigma} \delta_{\sigma} (\hat{c}^{\dagger}_{i\sigma}\hat{c}_{j\sigma} + \hat{c}^{\dagger}_{j\sigma}\hat{c}_{i\sigma}), \tag{4.18}$$

where $\delta_{\uparrow} = 1$ and $\delta_{\downarrow} = -1$, then (see Supplemental Materials at Section IA for further details)

$$\hat{\rho}^2_{ij} = \sum_{\sigma\sigma'} \delta_{\sigma}\delta_{\sigma'} (\hat{c}^{\dagger}_{i\sigma}\hat{c}_{j\sigma} + \hat{c}^{\dagger}_{j\sigma}\hat{c}_{i\sigma})(\hat{c}^{\dagger}_{i\sigma'}\hat{c}_{j\sigma'} + \hat{c}^{\dagger}_{j\sigma'}\hat{c}_{i\sigma'}). \tag{4.19}$$

Using this to re-express $\hat{H}_J$, we have

$$\begin{aligned}\hat{H}_J &= \sum_{i<j} J^{ij}(\hat{c}^\dagger_{i\uparrow}\hat{c}^\dagger_{j\downarrow}\hat{c}_{i\downarrow}\hat{c}_{j\uparrow} + \hat{c}^\dagger_{i\uparrow}\hat{c}^\dagger_{i\downarrow}\hat{c}_{j\downarrow}\hat{c}_{j\uparrow} + H.c.) \\ &= \sum_{i<j} -\frac{J^{ij}}{2}[\hat{\rho}^2_{ij} - \sum_\sigma (\hat{n}_{i\sigma} + \hat{n}_{j\sigma} - \hat{n}_{i\sigma}\hat{n}_{j\sigma} - \hat{n}_{j\sigma}\hat{n}_{i\sigma})] \\ &= \sum_{i<j} -\frac{J^{ij}}{2}\hat{\rho}^2_{ij} + \sum_{i<j,\sigma}\frac{J^{ij}}{2}(\hat{n}_{i\sigma} + \hat{n}_{j\sigma}) - \sum_{i<j,\sigma} J^{ij}\hat{n}_{i\sigma}\hat{n}_{j\sigma}.\end{aligned} \tag{4.20}$$

Employing this form for the decomposition, the exponential that stems from the first term of Equation 4.20 may now be transformed to yield

$$\begin{aligned}&e^{\Delta\tau \sum\limits_{i<j} \frac{J^{ij}}{2}[\sum\limits_\sigma \delta_\sigma(\hat{c}^\dagger_{i\sigma}\hat{c}_{j\sigma} + \hat{c}^\dagger_{j\sigma}\hat{c}_{i\sigma})]^2} \\ &= \prod_{i<j}\int dx_{ij}\frac{1}{\sqrt{2\pi}}e^{-x^2_{ij}/2}e^{x_{ij}\sqrt{\Delta\tau J^{ij}}[\sum\limits_\sigma \delta_\sigma(\hat{c}^\dagger_{i\sigma}\hat{c}_{j\sigma} + \hat{c}^\dagger_{j\sigma}\hat{c}_{i\sigma})]},\end{aligned} \tag{4.21}$$

which is real for $J^{ij} > 0$. Using the charge decomposition (Equation 4.44) when $J^{ij} < 0$ and the spin decomposition (Equation 4.43) when $J^{ij} > 0$ thus completely eliminates complex propagators, easing simulation. In Section 4.3.1, we compare the merits of using this mixed decomposition approach to exclusively relying upon the complex charge decomposition on the accuracy of our overall results.

Inserting the HS transformations defined by Equations 4.11, 4.12, 4.44, and 4.43 into Equations 4.9 and 4.10 and combining terms, one arrives at the final AFQMC expression for the projection operator

$$e^{-\Delta\tau\hat{H}} = \int d\mathbf{x} p(\mathbf{x})\hat{B}(\mathbf{x}), \tag{4.22}$$

where $\mathbf{x} = \{x_1, x_2, ..., x_{N_F}\}$ denotes the set of N_F total normally distributed auxiliary fields sampled at a given time slice, $\hat{B}(\mathbf{x})$ represents the amalgamation of all one-body operators, and $p(\mathbf{x})$ is a combination of all scalar functions of the fields. Example

expressions for $\hat{B}(\mathbf{x})$ and $p(\mathbf{x})$ are given in the Supplemental Material at Section IB. As is clear from Equation 4.22, the series of HS transformations described ultimately maps the original two-body propagator into a weighted integral over one-body propagators that are functions of external auxiliary fields.

4.2.5 Sampling in AFQMC

The sampling process together with the constrained path/phaseless approximations that are used to control the sign/phase problem in this work are introduced in Chapter 2 and won't be discussed here. Within the HK Hamiltonian framework, we here present the more detailed implementation of the background subtraction which is a static force and importance sampling where a dynamic force is conducted and show a clearer picture how these two techiniques are combined.

4.2.5.1 Background Subtraction

One of the simplest ways of reducing variances within AFQMC is via background subtraction [165]. As mentioned before, the two-body portion of a Hamiltonian is rewritten so that a mean field average is subtracted from each one-body operator. With a two-body operator written in the form of $\hat{V} = -\frac{1}{2}\sum_i \hat{v}_i^2$, together with background subtraction, it would be re-expressed as

$$\hat{V} = -\frac{1}{2}\sum_i \left(\hat{v}_i - \langle \hat{v}_i \rangle\right)^2 - \sum_i \hat{v}_i \langle \hat{v}_i \rangle + \frac{1}{2}\sum_i \langle \hat{v}_i \rangle^2, \tag{4.23}$$

where $\langle \hat{v}_i \rangle$ denotes the mean field average of the operator $\hat{v}_i$ (see Supplemental Materials at Section II for more details on how this mean field average is obtained).

Because the modified $\hat{v}_i - \langle \hat{v}_i \rangle$ operator will be smaller in magnitude than the bare $\hat{v}_i$ operator, background subtraction reduces the variance involved in AFQMC simulations. In this work, we perform background subtraction on the only term in the Hamiltonian that is not a product of on-site densities, the $\frac{J^{ij}}{2}\hat{\rho}_{ij}^2$ term of Equation 4.15 or the $-\frac{J^{ij}}{2}\hat{\rho}_{ij}^2$ term of Equation 4.20, yielding

$$\begin{aligned} \sum_{i<j} \frac{J^{ij}}{2}\hat{\rho}_{ij}^2 &= \sum_{i<j} \frac{J^{ij}}{2}(\hat{\rho}_{ij} - \langle \hat{\rho}_{ij} \rangle)^2 - \sum_{i<j} \frac{J^{ij}}{2}\langle \hat{\rho}_{ij} \rangle^2 \\ &+ \sum_{i<j} J^{ij}\langle \hat{\rho}_{ij} \rangle \hat{\rho}_{ij} \end{aligned} \tag{4.24}$$

and

$$\begin{aligned} \sum_{i<j} -\frac{J^{ij}}{2}\hat{\rho}_{ij}^2 &= \sum_{i<j} -\frac{J^{ij}}{2}(\hat{\rho}_{ij} - \langle \hat{\rho}_{ij} \rangle)^2 + \sum_{i<j} \frac{J^{ij}}{2}\langle \hat{\rho}_{ij} \rangle^2 \\ &- \sum_{i<j} J^{ij}\langle \hat{\rho}_{ij} \rangle \hat{\rho}_{ij}, \end{aligned} \tag{4.25}$$

respectively.

4.2.5.2 Importance Sampling

In order to further reduce the variance of walker weights and to make our simulations more amenable to the constrained path and phaseless approximations, here perform importance sampling, which aims to shift the center of the distribution from which we sample our auxiliary fields so that the most important fields are sampled more frequently. Because we utilize a mixture of discrete and continuous transformations and force bias importance sampling is only applicable to continuous transformations, in this work, we employ a formally equivalent strategy in which we shift *the propagators instead of the auxiliary fields*.

For continuous HS transformations, the details have been introduces in Chapter 2. Shifting the propagator within a discrete transformation proceeds in exactly the same fashion. Comparing Equations 4.16 and 4.12, the dynamic force needed to shift the propagator in Equation 4.12, for example, would be $F \equiv \gamma(\langle \hat{n}_1 \rangle - \langle \hat{n}_2 \rangle)$, resulting in the transformation

$$\begin{aligned} & e^{-\Delta\tau\alpha\hat{n}_1\hat{n}_2} e^{-\Delta\tau\alpha(\hat{n}_1+\hat{n}_2)/2} \sum_{x=\pm 1} \frac{1}{2} e^{\gamma x(\hat{n}_1-\hat{n}_2)} \\ & = e^{-\Delta\tau\alpha(\hat{n}_1+\hat{n}_2)/2} \sum_{x=\pm 1} \frac{1}{2} \left(\frac{e^{xF}}{W}\right) W e^{\gamma x(\hat{n}_1-\hat{n}_2)-xF}. \end{aligned} \tag{4.26}$$

As in the continuous case, in order to realize this transformation, fields are now sampled from a shifted probability density function, e^{xF}/W, where W is the normalization factor, $W = e^{xF} + e^{-xF}$, and the propagator $e^{(-\Delta\tau\alpha/2+\gamma x)\hat{n}_1} e^{(-\Delta\tau\alpha/2-\gamma x)\hat{n}_2}$ is applied with weight $\frac{1}{2} W e^{-xF}$. A shifted transformation may similarly be constructed for the discrete charge decomposition given by Equation 4.11. Propagators that include background subtraction may be shifted by simply replacing $\hat{A}$ with $\hat{A} - \langle \hat{A} \rangle$ in Equations 2.20 and 2.22 above (see the Supplemental Materials Section III for detailed formula).

It can readily be proven that shifting auxiliary fields is equivalent to shifting propagators [171, 172, 191]. Shifting propagators therefore entails a convenient way of combining importance sampling with discrete transformations, whose discrete fields cannot be shifted by the continuous force bias terms of conventional importance sampling techniques. Overall, the importance sampled propagation produces the same observable averages as free propagation, but favors the sampling of determinants with larger overlaps with the trial wave function and suppresses the sampling of determinants with no overlap.

4.2.6 Trial and Initial Wave Functions

Although AFQMC can readily accommodate multi-determinant trial wave functions, we restrict ourselves to employing single determinant trial wave functions that satisfy certain symmetries [192] such as the free electron (FE), restricted Hartree-Fock (RHF), unrestricted Hartree-Fock (UHF), and generalized Hartree-Fock (GHF) wave functions. RHF wave functions preserve spin symmetry. While RHF and UHF wave functions separately conserve the number of spin up and down electrons, GHF wave functions only conserve the total number of electrons. See Supplemental Materials at Section IV for details about how these wave functions are generated.

As illustrated in what follows, because GHF wave functions do not impose any spin symmetries and are therefore the most flexible of these wave function ansatzes, they enable the fastest AFQMC wave function relaxation to the global energy minimum. Nevertheless, when the number of up and down electrons must be fixed, UHF/RHF wave functions were employed instead. Even though our formalism permits our initial wave functions to differ from our trial wave functions, we take our initial and trial wave functions to be the same, except where otherwise noted.

4.3 Results and Discussion

4.3.1 Two-Band Hubbard Kanamori Model Benchmarks

In order to test the accuracy of our theoretical framework, we began by benchmarking our method against ED results for the one-dimensional, two-band HK

Table 4.1: The ground state energy of the two-band, 6×1 HK model with $N_\uparrow = N_\downarrow = 6$ over a range of parameters using ED and AFQMC. All energies and parameters are reported in units of t.

U	U_1	U_2	J	ED	AFQMC
2.0	1.5	1.0	0.5	-3.773268	-3.774(3)
2.0	1.5	1.0	1.0	-4.234037	-4.230(6)
2.0	1.5	3.0	0.5	0.758540	0.755(4)
3.0	5.0	1.0	0.5	2.460374	2.466(5)
6.0	1.5	1.0	0.5	1.496509	1.503(6)

Model on 5×1 and 6×1 lattices with periodic boundary conditions small enough to diagonalize. For these benchmarks, we simplify the Hamiltonian given by Equations 4.1 and 4.2 so that hopping can only occur between adjacent sites within the same bands and may be described by a single site- and spin-invariant constant t, such that

$$\hat{H}_1' = -t \sum_{\langle ij \rangle, \sigma} \sum_{m=1}^{2} \hat{c}_{im\sigma}^\dagger \hat{c}_{jm\sigma}. \tag{4.27}$$

We moreover assume that the parameters are site-invariant, such that $U^i = U$, $U_1^{ij} = U_1$, $U_2^{ij} = U_2$, and $J^{ij} = J$.

Table 4.1 presents our results for a 6×1 HK model over a representative set of parameters at half filling. All of the calculations presented were initialized using 560 walkers and employed FE trial and initial wave functions, except for the U=3.0, U_1=5.0, U_2=1.0, J=0.5 case. In this case, it was found that an RHF trial wave function yielded a lower trial energy and manifested a different spin order (antiferromagnetic (AFM) order between two bands) than the FE solution. Thus, an RHF trial wave function was employed instead. This demonstrates that trial wave functions should first be analyzed to determine whether their global minima exhibit the correct order before using them to guide propagation within AFQMC. Unless otherwise noted, all of the results presented in this section were obtained using a charge decomposition for J and the phaseless approximation to tame the related

phase problem that emerges.

As is clear from the table, AFQMC results are within $0.01t$ or less of the exact results, with the smallest discrepancy occurring for the $U = 2.0$, $U_1 = 1.5$ case and the largest occurring for the $U = 6.0$ case. In all of these cases, exact results are within two standard derivations of the Monte Carlo results, despite the use of the phaseless approximation.

To pinpoint AFQMC's systematic bias, as well as to better understand which regions of the phase diagram are the most challenging for AFQMC, we independently scanned through each of the U, U_1, U_2, and J parameters holding the others fixed for a 5×1 HK model. In Figures 4.1 and 4.2, we present our scans over U and J; See Supplemental Materials at Section V for figures of our U_1 and U_2 scans.

As shown in Figure 4.1, although the magnitude of the error bars on our energies grows with U, the relative error remains within 0.1% to 1% throughout this range. Similar trends are observed for U_1 and U_2, and using RHF, UHF, or GHF wave functions. This gives us reason to believe that our method can readily accommodate some of the even larger U values used in studies of strongly correlated materials. Nevertheless, much larger relative errors are observed as J is varied, as depicted in Figure 4.2. This is consistent with previous work, which also implicates the J terms as being most conducive to QMC errors [84]. Fortunately, for most real materials, J is usually a small fraction of U. For small J values, the relative errors are observed to remain less than 1% and are therefore controllable.

What may also be gleaned from Figure 4.2 is that the quality of the $J > 1.5$ energies depends upon the type of trial wave function employed. While free propagation calculations yield results that are independent of the trial wave function,

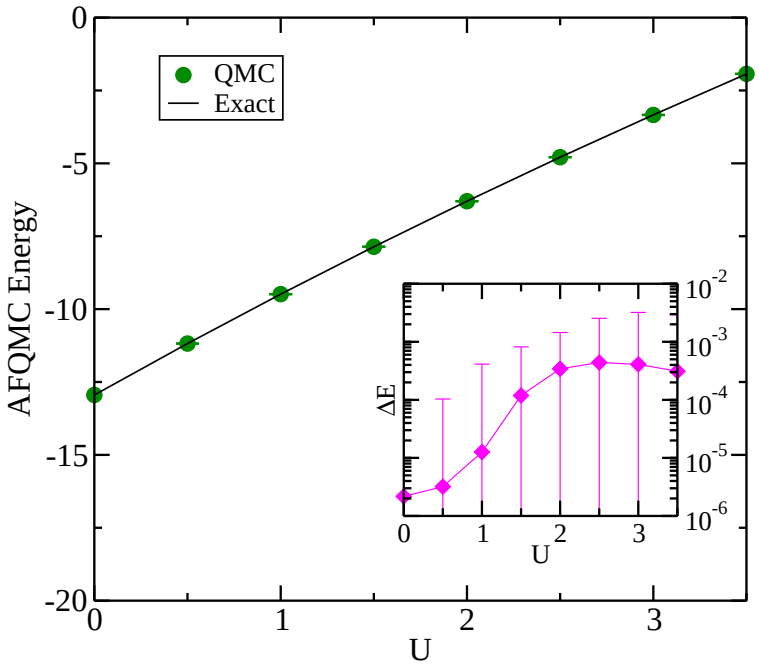

Figure 4.1: AFQMC ground state energy vs. the density-density parameter U for the two-band, 5×1 HK model using the charge decomposition and FE trial wave functions. Here, all of the other Hamiltonian parameters are held fixed at $t = 1$, U_1=0, U_2=0, and $J = 0$ with $N_\uparrow = N_\downarrow = 6$. Relative errors, ΔE, taken with respect to ED results are plotted in the inset for clarity.

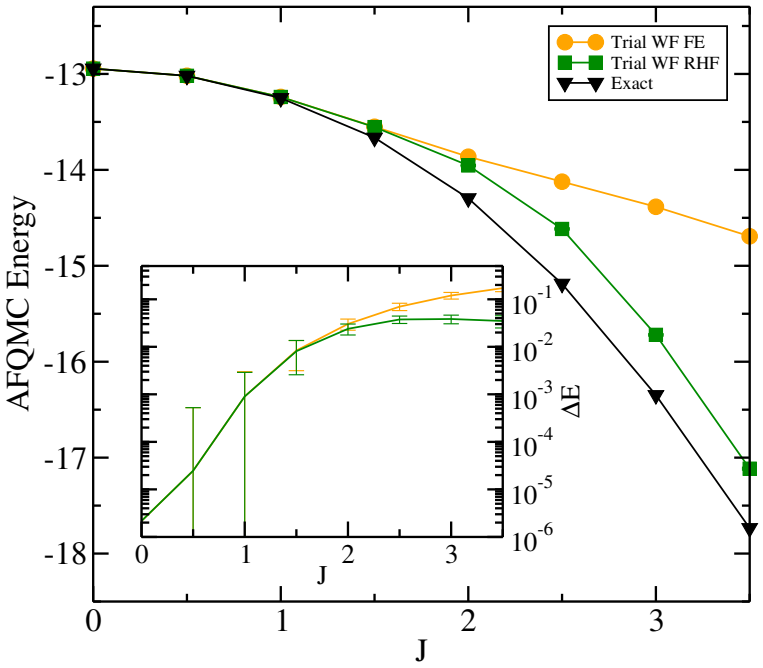

Figure 4.2: AFQMC ground state energy vs. the Hund's coupling parameter J for the two-band, 5×1 HK model using the charge decomposition and FE/RHF trial wave functions (WF). Here, all of the other Hamiltonian parameters are held fixed at $t = 1$, $U = 0$, U_1=0, and U_2=0 with $N_\uparrow = N_\downarrow = 6$. Relative errors, ΔE, taken with respect to ED results are plotted in the inset for clarity.

the quality of the constrained path and phaseless approximations fundamentally depend on the accuracy of the trial wave function. As depicted in Figure 4.2, the relative errors in the energies produced by FE trial wave functions surpass 10% and increase with increasing J; in contrast, the relative errors produced by RHF trial wave functions not only remain less than 10%, but plateau as a function of J. As J increases, the RHF electron density becomes non-uniform, yielding a lower variational energy than the FE wave function. Figure 4.2 thus demonstrates that AFQMC becomes more accurate as trial wave functions better describe the ground state. Note that we also tested UHF and GHF wave functions, which all converged to the same states as RHF wave functions.

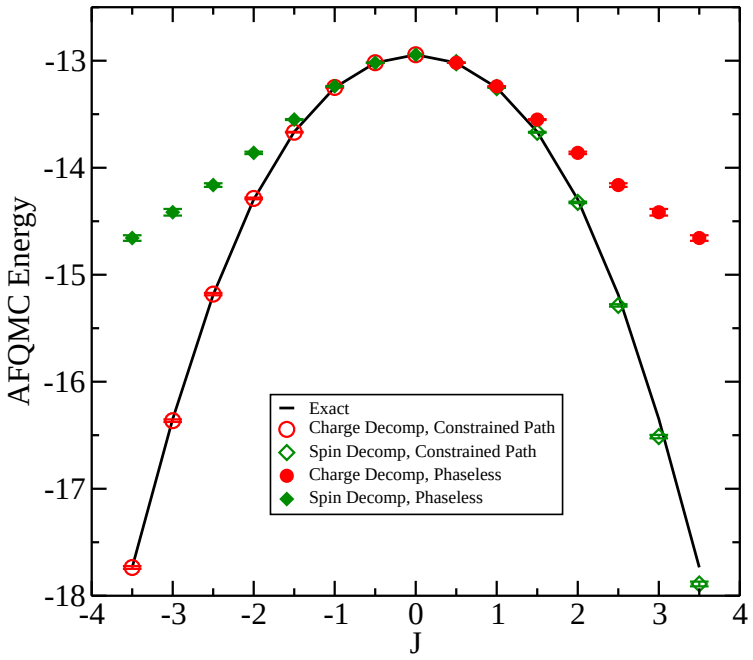

Figure 4.3: Comparison of phaseless and constrained path AFQMC energy errors as a function of J for a two-band, 5×1 HK model. Open circles denote parameters at which the constrained path approximation was employed, while closed circles denote parameters at which the phaseless approximation was employed. Here, we set $N_\uparrow = N_\downarrow = 6$, $t = 1$, $U = 0$, $U_1 = 0$, and $U_2 = 0$. FE trial wave functions were used for both the initial and trial wave functions, and 560 walkers were employed in each calculation.

The accuracy of AFQMC predictions are also influenced by the constrained path and phaseless approximations employed. In Figure 4.3, we compare the errors produced by these approximations. As discussed in Section 4.2.4, for $J > 0$, the spin decomposition will yield real propagators that we constrain using the constrained path approximation, while for $J < 0$, the spin decomposition will yield complex propagators that we constrain using the phaseless approximation. The charge decomposition behaves in the opposite fashion with respect to J. As shown in Figure 4.3, the constrained path approximation behaves significantly better than the phaseless approximation, which appreciably differs from the exact results for $|J| > 1.5$. Indeed, the constrained path approximation nearly reproduces the exact results for $J < 0$, only manifesting a slight deviation for larger positive values of J. These results attest to the fact that using the transformations we describe to prevent the phase problem from emerging is key to maintaining AFQMC accuracy. They also underscore that our method is capable of simulating -J values, which have been unattainable in previous QMC simulations. We expect these trends in accuracy to generalize to models with more bands and higher dimensionality.

4.3.2 Application to Three-Band Hubbard Kanamori Models

In order to understand how our techniques generalize to models that approximate more realistic materials and their magnetic phase transitions, we constructed a three-band model with an adjustable band gap. As illustrated in Figure 4.4, in this model, three bands are located at each site, one band of which is lower in energy by a 'band gap' parameter, Δ, than the other two degenerate bands. When $\Delta = 0$, all three bands are completely degenerate. Similar to the two-band model, the hopping occurs between adjacent sites within the same bands, with hopping constant $t_{ij} = 1$. While

the band gap would be fixed in any given material, creating a separate Δ parameter enables us to sample a range of band gaps and, by extension, to drive magnetic ordering transitions. We moreover assume that $U^i = U$ and $J^{ij} = J = 0.15U$ with $U_1^{ij} = U_1 = U - 2J$ and $U_2^{ij} = U_2 = U - 3J$, which are appropriate for the description of transition-metal oxides with a partially occupied t_{2g} shell [204]. In the following discussion, we fix our filling such that an average of four electrons occupy the three bands at each lattice site.

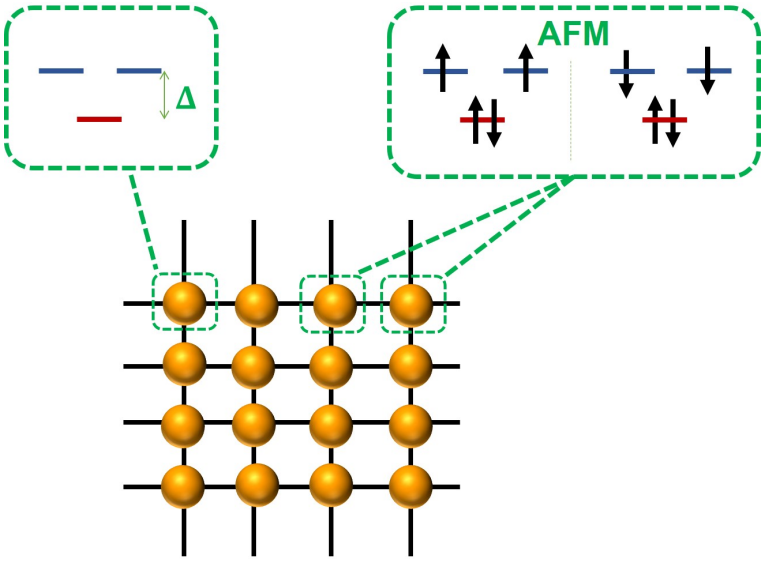

Figure 4.4: Schematic of our three-band model on a 4x4 lattice. At each site, there is one atom with three bands, one of which is lower in energy by Δ than the other two degenerate bands. The top right box illustrates a situation in which AFM order is present between adjacent lattice sites.

As an initial step, we benchmarked our AFQMC method against ED results. Diverging from our previous two-band analysis, as part of our three-band benchmarks, we studied our model on two-dimensional lattices with periodic boundary conditions, only varying Δ and U while keeping the other parameter relationships fixed in order to preserve realism. Our simulations were initialized with 560 walkers and GHF initial and trial wave functions for all of the benchmarks described below. The charge decomposition with the phaseless approximation was employed throughout this section.

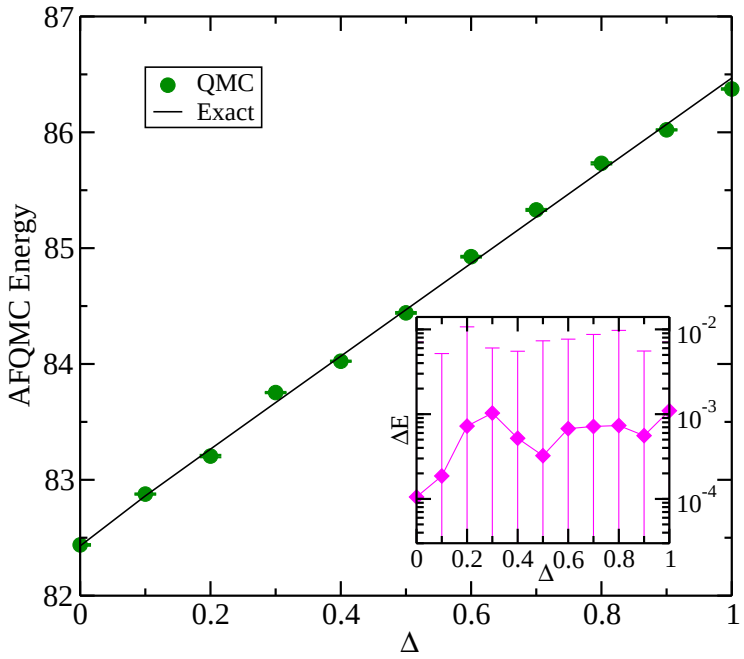

Figure 4.5: AFQMC ground state energy as a function of the band gap magnitude, Δ, for the three-band, 2×2 HK model using the charge decomposition and GHF trial wave functions. Here, all of the other Hamiltonian parameters are held fixed at $t = 1$, $U = 6$, $U_1 = U - 2J$, $U_2 = U - 3J$, and $J = 0.15U$ with $N_\uparrow = N_\downarrow = 8$. Relative errors, ΔE, taken with respect to ED results are plotted in the inset for clarity.

In Figure 4.5, we illustrate how the energy and relative errors change as Δ is varied from 0 to 1 with $U = 6$ on a 2×2 lattice. At fixed U, the relative error remains fairly stable and less than 0.1% throughout this range. This may be anticipated since the band gap only modifies the magnitude of the one-body terms and does not change the phase of the model, which do not directly contribute to our method's stochastic errors.

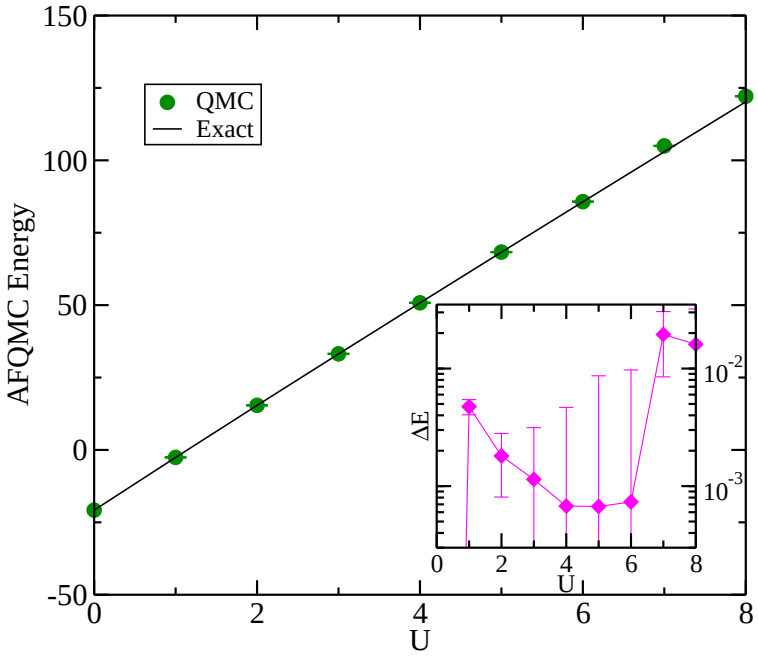

Figure 4.6: AFQMC ground state energy vs. U for the three-band, 2×2 HK model using the charge decomposition and GHF trial wave functions. Here, all of the other Hamiltonian parameters are held fixed at $t = 1$, $\Delta = 0.8$, $U_1 = U - 2J$, $U_2 = U - 3J$, and $J = 0.15U$ with $N_\uparrow = N_\downarrow = 8$. Relative errors, ΔE, are taken with respect to ED results are plotted in the inset for clarity.

In Figure 4.6, instead of scanning Δ, we scan U with $\Delta = 0.8$. As shown in Figure 4.6, the relative errors are larger in this case, but still range from 0.1% for $U < 6$ to 1% for $U > 6$. Errors would be expected to grow in this manner as the system becomes more correlated. Overall, the magnitudes of these relative errors suggest that AFQMC's performance is promising.

The rationale for introducing the band gap Δ parameter is to enable tuning of the magnetic order of the model system. Intuitively, when the band gap is small, the three bands are nearly degenerate and the four electrons have the largest freedom to move among the bands. Such a situation would favor ferromagnetic (FM) order. However, when the band gap becomes sufficiently large, two electrons will populate the lower band, forcing the other two electrons to reside among the higher energy bands. Such a situation would favor AFM order.

This intuition was confirmed by comparing the AFQMC energies attained using trial wave functions with FM and AFM order, respectively (see Figure 4.7). Typically, GHF calculations converge to the lowest state with the same magnetic order as the initial state. Thus, in order to construct wave functions with FM order, a randomly initialized density matrix was supplied to the GHF self-consistent equations; to construct wave functions with AFM order, an AFM-ordered initial density matrix was supplied. Several independent GHF calculations were conducted for each system studied to guarantee that the final GHF wave functions produced attained their global minima. For large Δ ($\Delta \gtrsim 1.1$) values at which ferromagnetic order is disfavored, GHF calculations initialized with random density matrices often developed order. In these situations, FM wave functions produced at smaller values of Δ were used as trial wave functions in "FM" AFQMC calculations performed at larger Δ values. Figure 4.7 depicts the energies of AFQMC simulations performed with AFM and FM trial wave functions, respectively, as a function of band gap. All of the AFQMC energies presented here are the lowest energies we can obtain at each Δ. At smaller Δs, trial wave functions with FM order led to the lowest AFQMC energies, while at larger Δs, AFM trial wave functions did so. This confirms that our model undergoes a ferromagnetic to antiferromagnetic transition at roughly $\Delta = 1.15$. In contrast, Hartree-Fock theory predicts the transition to occur at $\Delta = 0.5$, which is

reasonable since Hartree-Fock theory tends to favor AFM order. An illustration of the AFM order exhibited by our model is depicted in Figure 4.4.

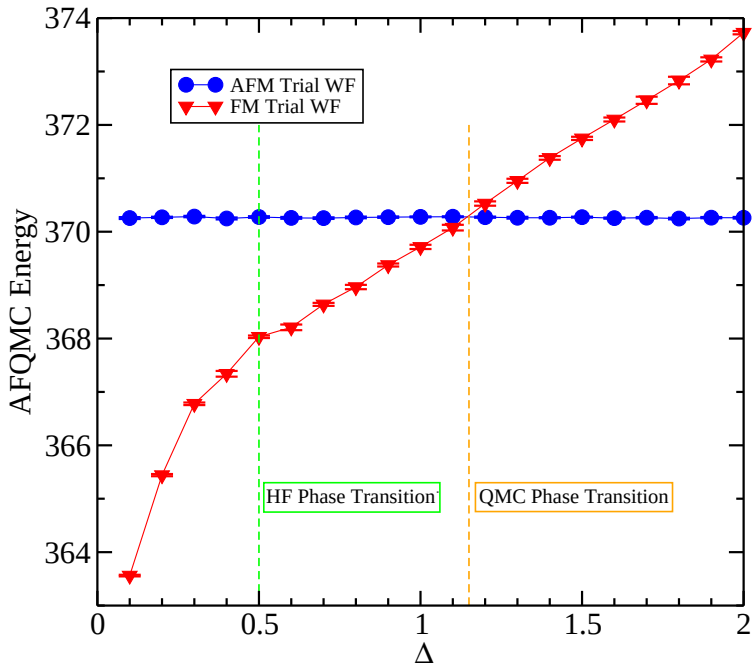

Figure 4.7: AFQMC ground state energy vs. band gap magnitude, Δ, for the three-band, 4×4 HK model using the charge decomposition. GHF trial wave functions with both FM order and AFM order are used. QMC predicted a phase transition to occur at around $\Delta = 1.15$, as illustrated by the orange dotted line. Hartree-Fock predicted a phase transition to occur at $\Delta = 0.5$, as illustrated by the green dotted line. Here, all of the other Hamiltonian parameters are held fixed at $t = 1$, $U = 6$, $U_1 = U - 2J$, $U_2 = U - 3J$, and $J = 0.15\ U$ with $N_\uparrow = N_\downarrow = 32$.

To further corroborate the phase transition we observe, we estimated the magnitude of the charge gap at $\Delta = 0.2$ and $\Delta = 1.5$. To do so, we computed the ground state AFQMC energies of 4×4, 6×6, and 8×8-site systems, with three bands occupied by four electrons situated at each site. The charge gap may be determined by computing $E_{N-1} + E_{N+1} - 2E_N$, where N denotes the total number of electrons in the system. To determine the charge gap in the thermodynamic limit, we fit a $1/L$ form, where L denotes the total number of lattice sites, to the energies and extrapolated to the infinite L limit (see Supplemental Materials at Section V for details about the extrapolation). The energies produced using FM initial trial wave

functions were used to ascertain the $\Delta = 0.2$ charge gap, while those produced using AFM wave functions were employed to ascertain the $\Delta = 1.5$ charge gap. The charge gaps obtained are presented in Table 4.2. After extrapolations, the $\Delta = 0.2$ charge gap converged to -0.006(47) and the $\Delta = 1.5$ charge gap converged to 1.201(41). As one would expect antiferromagnetic, not ferromagnetic, order to be accompanied by a charge gap, these extrapolations support our previous conclusions.

Table 4.2: The charge gaps of the three-band model at $\Delta = 0.2$ and $\Delta = 1.5$ for different system sizes calculated using AFQMC. GHF trial wave functions with FM order and AFM order are used at $\Delta = 0.2$ and $\Delta = 1.5$, respectively. All of the other Hamiltonian parameters are held fixed at $t = 1$, $U = 6$, $U_1 = U - 2J$, $U_2 = U - 3J$, and $J = 0.15U$. The electron density per band is 4/3.

# of bands	Charge Gap ($\Delta = 0.2$)	Charge Gap ($\Delta = 1.5$)
4x4x3	0.222(29)	1.311(32)
6x6x3	0.103(27)	1.268(35)
8x8x3	0.015(72)	1.225(36)
∞	-0.006(47)	1.201(41)

The successful determination of the magnetic order and charge gaps in this model system illustrate our method's promise for accurately modeling realistic materials.

4.4 Conclusions

In summary, we have presented a ground state AFQMC framework suited for the study of the HK model, a multi-band model designed to capture the Hund's physics of many d- and f-electron materials. Diverging with past QMC studies of the HK model, we employ a novel set of HS transformations to decouple the Hund's coupling terms while preserving the terms' essential physics. We find that by carefully combining these transformations with a form of importance sampling that shifts our propagators, well-optimized GHF wave functions, and the constrained path

and phaseless approximations, we can accurately predict the energetics of benchmark lattice models and the magnetic order of much larger models that approximate realistic materials. Overall, we find that the phaseless version of our method produces nearly exact energies for small models for $-3 < J < 3$, a range of J values which contains those commonly observed in experiment. This bodes well for the generalization of our method to other systems.

Our method may readily be extended to include spin-orbit coupling effects and negative J values, which opens the doors to the highly accurate study of exotic, -J fulleride physics [156, 157]. In order to describe superconducting physics, our method can be adapted to use superconducting trial wave function forms, including Bardeen-Cooper-Schrieffer [20, 191] and Hartree-Fock-Bogoliubov [193] wave functions. We foresee our method having the most immediate impact as a way to delineate low-temperature phase diagrams currently beyond the reach of DMFT methods. As the same transformations and importance sampling techniques may readily be adapted into finite temperature AFQMC formalisms [90, 126, 233], the same methods may be used to develop low scaling, sign and phase problem free impurity solvers. We look forward to employing our methods to more accurately elucidate the complex many body physics of $4d$ transition metal oxides such as the ruthenates, rhodates, and molybedenates in the near future.

4.5 Supplemental Materials

4.5.1 Hubbard-Stratonovich Transformation Details

4.5.1.1 Decomposition of Hund's Terms

In the following, we more clearly derive the decomposition of the Hund's contribution to the Hamiltonian given by Equation (15). Taking the charge decomposition as an example, as was mentioned in Equations (13) and (14) in the main text, we first let

$$\hat{\rho}_{ij} = \sum_{\sigma} (\hat{c}^{\dagger}_{i\sigma}\hat{c}_{j\sigma} + \hat{c}^{\dagger}_{j\sigma}\hat{c}_{i\sigma}). \tag{4.28}$$

It therefore follows that

$$\hat{\rho}^2_{ij} = \sum_{\sigma\sigma'} (\hat{c}^{\dagger}_{i\sigma}\hat{c}_{j\sigma} + \hat{c}^{\dagger}_{j\sigma}\hat{c}_{i\sigma})(\hat{c}^{\dagger}_{i\sigma'}\hat{c}_{j\sigma'} + \hat{c}^{\dagger}_{j\sigma'}\hat{c}_{i\sigma'}). \tag{4.29}$$

This sum consists of three distinct cases:

1. $\sigma{=}\uparrow$, $\sigma'{=}\downarrow$:

   $\hat{c}^{\dagger}_{i\uparrow}\hat{c}_{j\uparrow}\hat{c}^{\dagger}_{i\downarrow}\hat{c}_{j\downarrow} + \hat{c}^{\dagger}_{i\uparrow}\hat{c}_{j\uparrow}\hat{c}^{\dagger}_{j\downarrow}\hat{c}_{i\downarrow} + \hat{c}^{\dagger}_{j\uparrow}\hat{c}_{i\uparrow}\hat{c}^{\dagger}_{i\downarrow}\hat{c}_{j\downarrow} + \hat{c}^{\dagger}_{j\uparrow}\hat{c}_{i\uparrow}\hat{c}^{\dagger}_{j\downarrow}\hat{c}_{i\downarrow} = \hat{c}^{\dagger}_{i\uparrow}\hat{c}^{\dagger}_{i\downarrow}\hat{c}_{j\downarrow}\hat{c}_{j\uparrow} + \hat{c}^{\dagger}_{i\uparrow}\hat{c}^{\dagger}_{j\downarrow}\hat{c}_{i\downarrow}\hat{c}_{j\uparrow} + \hat{c}^{\dagger}_{j\uparrow}\hat{c}^{\dagger}_{i\downarrow}\hat{c}_{j\downarrow}\hat{c}_{i\uparrow} + \hat{c}^{\dagger}_{j\uparrow}\hat{c}^{\dagger}_{j\downarrow}\hat{c}_{i\downarrow}\hat{c}_{j\downarrow}$

2. $\sigma{=}\downarrow$, $\sigma'{=}\uparrow$:

   $\hat{c}^{\dagger}_{i\downarrow}\hat{c}_{j\downarrow}\hat{c}^{\dagger}_{i\uparrow}\hat{c}_{j\uparrow} + \hat{c}^{\dagger}_{i\downarrow}\hat{c}_{j\downarrow}\hat{c}^{\dagger}_{j\uparrow}\hat{c}_{i\uparrow} + \hat{c}^{\dagger}_{j\downarrow}\hat{c}_{i\downarrow}\hat{c}^{\dagger}_{i\uparrow}\hat{c}_{j\uparrow} + \hat{c}^{\dagger}_{j\downarrow}\hat{c}_{i\downarrow}\hat{c}^{\dagger}_{j\uparrow}\hat{c}_{i\uparrow} = \hat{c}^{\dagger}_{i\uparrow}\hat{c}^{\dagger}_{i\downarrow}\hat{c}_{j\downarrow}\hat{c}_{j\uparrow} + \hat{c}^{\dagger}_{j\uparrow}\hat{c}^{\dagger}_{i\downarrow}\hat{c}_{j\downarrow}\hat{c}_{i\uparrow} + \hat{c}^{\dagger}_{i\uparrow}\hat{c}^{\dagger}_{j\downarrow}\hat{c}_{i\downarrow}\hat{c}_{j\uparrow} + \hat{c}^{\dagger}_{j\uparrow}\hat{c}^{\dagger}_{j\downarrow}\hat{c}_{i\downarrow}\hat{c}_{i\uparrow}$

3. $\sigma{=}\sigma'$:

   $\sum_{\sigma}(\hat{c}^{\dagger}_{i\sigma}\hat{c}_{j\sigma} + \hat{c}^{\dagger}_{j\sigma}\hat{c}_{i\sigma})^2$, the terms of which simplify to:

(a) $\hat{c}^{\dagger}_{i\sigma}\hat{c}_{j\sigma}\hat{c}^{\dagger}_{i\sigma}\hat{c}_{j\sigma} = \hat{c}^{\dagger}_{i\sigma}(\delta_{ij} - \hat{c}^{\dagger}_{i\sigma}\hat{c}_{j\sigma})\hat{c}_{j\sigma} = \delta_{ij}\hat{c}^{\dagger}_{i\sigma}\hat{c}_{j\sigma} = 0 (i \neq j)$

(b) $\hat{c}^{\dagger}_{j\sigma}\hat{c}_{i\sigma}\hat{c}^{\dagger}_{j\sigma}\hat{c}_{i\sigma} = \hat{c}^{\dagger}_{j\sigma}(\delta_{ij} - \hat{c}^{\dagger}_{j\sigma}\hat{c}_{i\sigma})\hat{c}_{i\sigma} = \delta_{ij}\hat{c}^{\dagger}_{j\sigma}\hat{c}_{i\sigma} = 0 (i \neq j)$

(c) $\hat{c}^{\dagger}_{i\sigma}\hat{c}_{j\sigma}\hat{c}^{\dagger}_{j\sigma}\hat{c}_{i\sigma} = \hat{c}^{\dagger}_{i\sigma}(1 - \hat{c}^{\dagger}_{j\sigma}\hat{c}_{j\sigma})\hat{c}_{i\sigma} = \hat{n}_{i\sigma}(1 - \hat{n}_{j\sigma}) = \hat{n}_{i\sigma} - \hat{n}_{i\sigma}\hat{n}_{j\sigma}$

(d) $\hat{c}^{\dagger}_{j\sigma}\hat{c}_{i\sigma}\hat{c}^{\dagger}_{i\sigma}\hat{c}_{j\sigma} = \hat{n}_{j\sigma}(1 - \hat{n}_{i\sigma}) = \hat{n}_{j\sigma} - \hat{n}_{j\sigma}\hat{n}_{i\sigma}$

Note that cases 1 and 2 yield the same result. Thus,

$$\begin{aligned} \hat{\rho}^2_{ij} &= 2(\hat{c}^{\dagger}_{i\uparrow}\hat{c}^{\dagger}_{i\downarrow}\hat{c}_{j\downarrow}\hat{c}_{j\uparrow} + \hat{c}^{\dagger}_{i\uparrow}\hat{c}^{\dagger}_{j\downarrow}\hat{c}_{i\downarrow}\hat{c}_{j\uparrow} + \hat{c}^{\dagger}_{j\uparrow}\hat{c}^{\dagger}_{i\downarrow}\hat{c}_{j\downarrow}\hat{c}_{i\uparrow} + \hat{c}^{\dagger}_{j\uparrow}\hat{c}^{\dagger}_{j\downarrow}\hat{c}_{i\downarrow}\hat{c}_{j\downarrow}) \\ &+ \hat{n}_{i\sigma} - \hat{n}_{i\sigma}\hat{n}_{j\sigma} + \hat{n}_{j\sigma} - \hat{n}_{j\sigma}\hat{n}_{i\sigma}. \end{aligned} \tag{4.30}$$

As such,

$$\begin{aligned} \sum_{i<j} J^{ij}(\hat{c}^{\dagger}_{i\uparrow}\hat{c}^{\dagger}_{j\downarrow}\hat{c}_{i\downarrow}\hat{c}_{j\uparrow} + \hat{c}^{\dagger}_{i\uparrow}\hat{c}^{\dagger}_{i\downarrow}\hat{c}_{j\downarrow}\hat{c}_{j\uparrow} + h.c.) &= \sum_{i<j}\frac{J^{ij}}{2}[\hat{\rho}^2_{ij} - \sum_{\sigma}(\hat{n}_{i\sigma} + \hat{n}_{j\sigma} - \hat{n}_{i\sigma}\hat{n}_{j\sigma} - \hat{n}_{j\sigma}\hat{n}_{i\sigma})] \\ &= \sum_{i<j}\frac{J^{ij}}{2}\hat{\rho}^2_{ij} - \sum_{i<j,\sigma}\frac{J^{ij}}{2}(\hat{n}_{i\sigma} + \hat{n}_{j\sigma} - 2\hat{n}_{i\sigma}\hat{n}_{j\sigma}), \end{aligned} \tag{4.31}$$

which is consistent with Equation (15). With this in hand, the overall Hamiltonian may be re-expressed as

$$\begin{aligned}\hat{H} = &\sum_{ij,\sigma\sigma\prime} t_{ij}^{\sigma\sigma\prime} \hat{c}_{i\sigma}^{\dagger} \hat{c}_{j\sigma\prime} \\ &+ \sum_{i} U^{i} \hat{n}_{i\uparrow} \hat{n}_{i\downarrow} \\ &+ \sum_{i<j} U_{1}^{ij} (\hat{n}_{i\uparrow} \hat{n}_{j\downarrow} + \hat{n}_{i\downarrow} \hat{n}_{j\uparrow}) \\ &+ \sum_{i<j} (U_{2}^{ij} + J^{ij}) (\hat{n}_{i\uparrow} \hat{n}_{j\uparrow} + \hat{n}_{i\downarrow} \hat{n}_{j\downarrow}) \\ &+ \sum_{i<j} -\frac{J^{ij}}{2} (\hat{n}_{i\uparrow} + \hat{n}_{j\uparrow} + \hat{n}_{i\downarrow} + \hat{n}_{j\downarrow}) \\ &+ \sum_{i<j} \frac{J^{ij}}{2} (\sum_{\sigma} \hat{c}_{i\sigma}^{\dagger} \hat{c}_{j\sigma} + \hat{c}_{j\sigma}^{\dagger} \hat{c}_{i\sigma})^{2}.\end{aligned} \tag{4.32}$$

The derivation of Equation (20) follows similarly with Equation (13) simply replaced by Equation (18).

4.5.1.2 Full Final Propagators

As described in Section IID of the manuscript, after a number of Hubbard-Stratonovich (HS) transformations, the projection operator may be re-expressed as an integral over all auxiliary fields, $\mathbf{x} = \{\mathbf{x}^{U}, \mathbf{x}_{1}^{U_1}, \mathbf{x}_{2}^{U_1}, \mathbf{x}_{1}^{U_2+J}, \mathbf{x}_{2}^{U_2+J}, \mathbf{x}^{J}\}$, of the product of the operators $\hat{B}(\mathbf{x})$ and constants $p(\mathbf{x})$ as given in Equation (22). If only charge decompositions are employed,

$$p(\mathbf{x}) = \left(\frac{1}{2}\right)^{(N_U + 2N_{U_1} + 2N_{U_2+J})} (2\pi)^{-\frac{N_J}{2}} \prod_{i<j}^{N_J} e^{-x_{ij}^{2}/2} \tag{4.33}$$

and

$$\hat{B}(\mathbf{x}) = e^{-\Delta\tau\hat{H}_1'/2}\left[\prod_i \hat{b}_i^U(x_i^U)\right]\left[\prod_{i<j}\hat{b}_{1,ij}^{U_1}(x_{1,ij}^{U_1})\hat{b}_{2,ij}^{U_1}(x_{2,ij}^{U_1})\hat{b}_{1,ij}^{U_2+J}(x_{1,ij}^{U_2+J})\hat{b}_{2,ij}^{U_2+J}(x_{2,ij}^{U_2+J})\hat{b}_{ij}^{J}(x_{ij}^{J})\right] e^{-\Delta\tau\hat{H}_1'/2} \tag{4.34}$$

where N_U is the number of U transforms and N_{U_1}=N_{U_2}=N_J is the number of U_1, U_2, and J transforms. Moreover,

$$\hat{b}_i^U(x_i^U) = e^{(\gamma x_i^U - \Delta\tau U/2)(\hat{n}_{i\uparrow}+\hat{n}_{i\downarrow}-1)}, \tag{4.35}$$

$$\hat{b}_{1,ij}^{U_1}(x_{1,ij}^{U_1}) = e^{(\gamma x_{1,ij}^{U_1} - \Delta\tau U_1/2)(\hat{n}_{i\uparrow}+\hat{n}_{j\downarrow}-1)}, \tag{4.36}$$

$$\hat{b}_{2,ij}^{U_1}(x_{2,ij}^{U_1}) = e^{(\gamma x_{2,ij}^{U_1} - \Delta\tau U_1/2)(\hat{n}_{i\downarrow}+\hat{n}_{j\uparrow}-1)}, \tag{4.37}$$

$$\hat{b}_{1,ij}^{U_2+J}(x_{1,ij}^{U_2+J}) = e^{(\gamma x_{1,ij}^{U_2+J} - \Delta\tau((U_2+J)/2)(\hat{n}_{i\uparrow}+\hat{n}_{j\uparrow}-1)}, \tag{4.38}$$

$$\hat{b}_{2,ij}^{U_2+J}(x_{2,ij}^{U_2+J}) = e^{(\gamma x_{2,ij}^{U_2+J} - \Delta\tau((U_2+J)/2)(\hat{n}_{i\downarrow}+\hat{n}_{j\downarrow}-1)}, \tag{4.39}$$

and

$$\hat{b}_{ij}^{J}(x_{ij}^{J}) = e^{\sqrt{-\Delta\tau J^{ij}}x_{ij}^J\sum_\sigma(\hat{c}_{i\sigma}^\dagger\hat{c}_{j\sigma}+\hat{c}_{j\sigma}^\dagger\hat{c}_{i\sigma})}. \tag{4.40}$$

Note that there are two U_1 and two $U_2 + J$ propagators since there are two U_1 and two $U_2 + J$ two-body terms in Equation 5. As described in the text, i denotes the superindices that combine band and lattice sites, while $i < j$ denotes the possible set of i,j combinations between different pairs of bands on the same lattice site. $\hat{H}_1'$ consists of $\hat{H}_1$ and all one-body terms that stem from the J transform given by Equations (15) and (20) of the manuscript.

4.5.2 Background Subtraction Details

It has been shown that the sign and phase problems may be dramatically reduced if the Hamiltonian prior to an HS decomposition is rewritten such that an estimate of the ground state expectation value is subtracted from each squared operator [164, 165, 172]. As an illustration, here, we demonstrate how background subtraction may be performed on the squared term of the Hund's coupling portion of the Hamiltonian. If the spin decomposition is used for the Hund's coupling contribution as in Equation (20), the squared term to consider is $\sum_{i<j}(-\frac{J^{ij}}{2})\hat{\rho}_{ij}^2$, where $\hat{\rho}_{ij} = \sum_\sigma \delta_\sigma(\hat{c}_{i\sigma}^\dagger \hat{c}_{j\sigma} + \hat{c}_{j\sigma}^\dagger \hat{c}_{i\sigma})$. In background subtraction, this term is re-expressed as

$$\sum_{i<j} -\frac{J^{ij}}{2}\hat{\rho}_{ij}^2 = \sum_{i<j} -\frac{J^{ij}}{2}(\hat{\rho}_{ij} - \langle\hat{\rho}_{ij}\rangle)^2 + \sum_{i<j}\frac{J^{ij}}{2}\langle\hat{\rho}_{ij}\rangle^2 - \sum_{i<j} J^{ij}\langle\hat{\rho}_{ij}\rangle\hat{\rho}_{ij}, \tag{4.41}$$

where $\langle\hat{\rho}_{ij}\rangle$ is the mean field expectation value of $\hat{\rho}_{ij}$. By re-expressing $\hat{\rho}_{ij}^2$ in this fashion, the resulting squared term is smaller in magnitude than the original. The first term of this equation is decomposed via an HS decomposition, the second term is a constant that can be added to the energy at the end of a calculation, and the third term can be added to the one-body operator.

Similarly for the charge decomposition, the squared J term of the Hamiltonian is $\sum_{i<j}(\frac{J^{ij}}{2})\hat{\rho}_{ij}^2$, where $\hat{\rho}_{ij} = \sum_\sigma(\hat{c}_{i\sigma}^\dagger \hat{c}_{j\sigma} + \hat{c}_{j\sigma}^\dagger \hat{c}_{i\sigma})$. $\langle\hat{\rho}_{ij}\rangle$ is the mean field term, which we denote as b_{ij} to distinguish it from the mean field term in Equation (14) in the following. In this case, the Hamiltonian may be written as

$$\sum_{i<j}\frac{J^{ij}}{2}\hat{\rho}_{ij}^2 = \sum_{i<j}\frac{J^{ij}}{2}(\hat{\rho}_{ij} - b_{ij})^2 - \sum_{i<j}\frac{J^{ij}}{2}b_{ij}^2 + \sum_{i<j} J^{ij}b_{ij}\hat{\rho}_{ij}. \tag{4.42}$$

The squared term in Equation (15) may be transformed using the spin decomposition

to yield

$$e^{\Delta\tau \sum\limits_{i<j} \frac{J^{ij}}{2}[\sum\limits_{\sigma} \delta_\sigma(\hat{c}^\dagger_{i\sigma}\hat{c}_{j\sigma}+\hat{c}^\dagger_{j\sigma}\hat{c}_{i\sigma})-b_{ij}]^2} = \int dx \frac{1}{\sqrt{2\pi}} e^{-x^2/2} e^{x\sqrt{\Delta\tau J^{ij}}[\sum\limits_{\sigma} \delta_\sigma(\hat{c}^\dagger_{i\sigma}\hat{c}_{j\sigma}+\hat{c}^\dagger_{j\sigma}\hat{c}_{i\sigma})-b_{ij}]}. \tag{4.43}$$

The squared term in Equation (14) may be decomposed using the charge decomposition to obtain

$$e^{-\Delta\tau \sum\limits_{i<j} \frac{J^{ij}}{2}[\sum\limits_{\sigma} (\hat{c}^\dagger_{i\sigma}\hat{c}_{j\sigma}+\hat{c}^\dagger_{j\sigma}\hat{c}_{i\sigma})-b_{ij}]^2} = \int dx \frac{1}{\sqrt{2\pi}} e^{-x^2/2} e^{x\sqrt{-\Delta\tau J^{ij}}[\sum\limits_{\sigma} (\hat{c}^\dagger_{i\sigma}\hat{c}_{j\sigma}+\hat{c}^\dagger_{j\sigma}\hat{c}_{i\sigma})-b_{ij}]} \tag{4.44}$$

Note that the formula for the "mean field" value b_{ij} is very similar to the average operator $\langle \hat{A} \rangle$ introduced in the main text. The difference is that the "mean field" is a constant, which can be evaluated at the very outset of a simulation. The average operator $\langle \hat{A} \rangle$ is a dynamic value which is calculated at every step on the fly.

4.5.3 Background Subtraction with a Dynamic Force

As described in the main text, the dynamic force is the expectation value of the operator that is squared in the propagator. Including the background subtraction described above, the operator becomes $[\sum\limits_{\sigma} \delta_\sigma(\hat{c}^\dagger_{i\sigma}\hat{c}_{j\sigma} + \hat{c}^\dagger_{j\sigma}\hat{c}_{i\sigma}) - b_{ij}]$ when the spin decomposition is applied and $[\sum\limits_{\sigma} (\hat{c}^\dagger_{i\sigma}\hat{c}_{j\sigma}+\hat{c}^\dagger_{j\sigma}\hat{c}_{i\sigma})-b_{ij}]$ when the charge decomposition is applied. After combining the HS transformation with importance sampling, the $\hat{H}_J$ propagator transformed using the spin decomposition may be rewritten as

$$\begin{aligned} & e^{\Delta\tau \sum\limits_{i<j} \frac{J^{ij}}{2}[\sum\limits_{\sigma} \delta_\sigma(\hat{c}^\dagger_{i\sigma}\hat{c}_{j\sigma}+\hat{c}^\dagger_{j\sigma}\hat{c}_{i\sigma})-b_{ij}]^2} \\ &= \int dx \frac{1}{\sqrt{2\pi}} e^{-x^2/2} e^{x\sqrt{\Delta\tau J^{ij}}[\sum\limits_{\sigma} \delta_\sigma(\hat{c}^\dagger_{i\sigma}\hat{c}_{j\sigma}+\hat{c}^\dagger_{j\sigma}\hat{c}_{i\sigma})-b_{ij}]} \\ &= \int dx \frac{1}{\sqrt{2\pi}} e^{-(x-F')^2/2} e^{\frac{1}{2}F'^2 - xF'} e^{x\sqrt{\Delta\tau J^{ij}}[\sum\limits_{\sigma} \delta_\sigma(\hat{c}^\dagger_{i\sigma}\hat{c}_{j\sigma}+\hat{c}^\dagger_{j\sigma}\hat{c}_{i\sigma})-b_{ij}]}, \end{aligned} \tag{4.45}$$

where F' denotes the dynamic force and becomes $\sqrt{\Delta\tau J^{ij}}\langle\sum_{\sigma}\delta_{\sigma}(\hat{c}^{\dagger}_{i\sigma}\hat{c}_{j\sigma}+\hat{c}^{\dagger}_{j\sigma}\hat{c}_{i\sigma})-b_{ij}\rangle$. A similar transform may be constructed when the charge decomposition is employed with $F' = \sqrt{-\Delta\tau J^{ij}}\langle\sum_{\sigma}(\hat{c}^{\dagger}_{i\sigma}\hat{c}_{j\sigma} + \hat{c}^{\dagger}_{j\sigma}\hat{c}_{i\sigma}) - b_{ij}\rangle$.

4.5.4 Supplemental Data and Figures

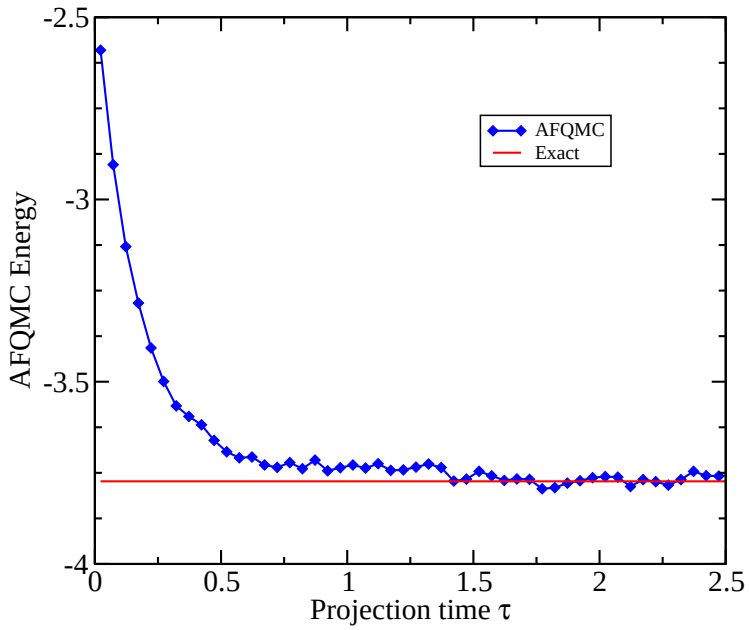

Figure 4.8: The time evolution of the total AFQMC energy using $\Delta\tau$=0.005 with 560 walkers for a two-band, 6×1 Hubbard Kanamori model. $N_{\uparrow}$= $N_{\downarrow}$=6, $t = 1$, $U = 2$, $U_1 = 1.5$, $U_2 = 1.0$, and $J = 0.5$. For this case, a free electron (FE) wave function was employed as both the trial and initial wave functions.

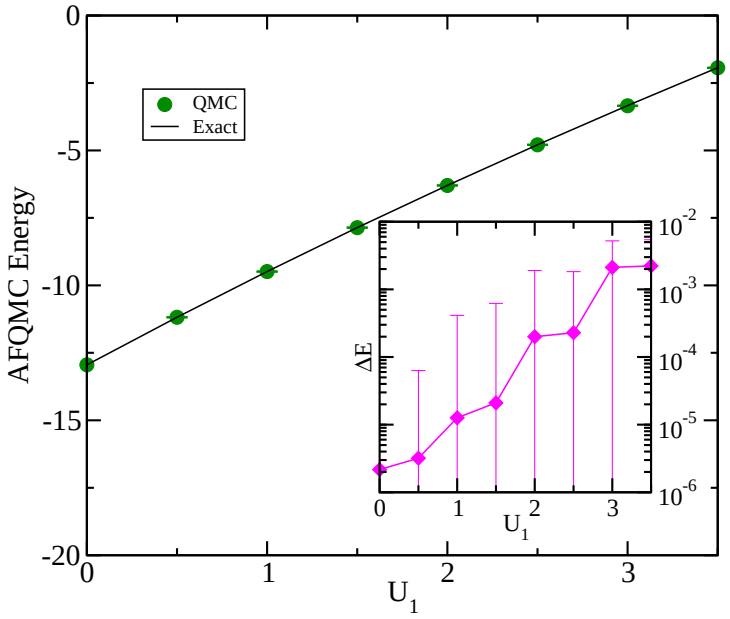

Figure 4.9: AFQMC ground state energy vs. the density-density parameter U_1 for the two-band, 5×1 Hubbard Kanamori model using the charge decomposition and FE trial wave functions. Here, all of the other Hamiltonian parameters are held fixed at $t = 1$, U=0, U_2=0, and $J = 0$ with $N_\uparrow = N_\downarrow = 6$. Relative errors, ΔE, taken with respect to Exact Diagonalization (ED) results are plotted in the inset for clarity.

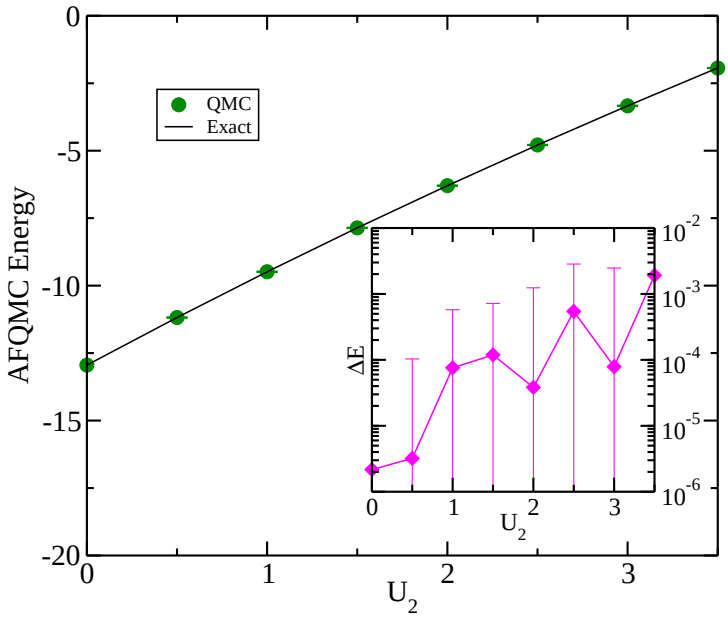

Figure 4.10: AFQMC ground state energy vs. the density-density parameter U_2 for the two-band, 5×1 Hubbard Kanamori model using the charge decomposition and FE trial wave functions. Here, all of the other Hamiltonian parameters are held fixed at $t = 1$, U=0, U_1=0, and $J = 0$ with $N_\uparrow = N_\downarrow = 6$. Relative errors, ΔE, taken with respect to ED results are plotted in the inset for clarity.

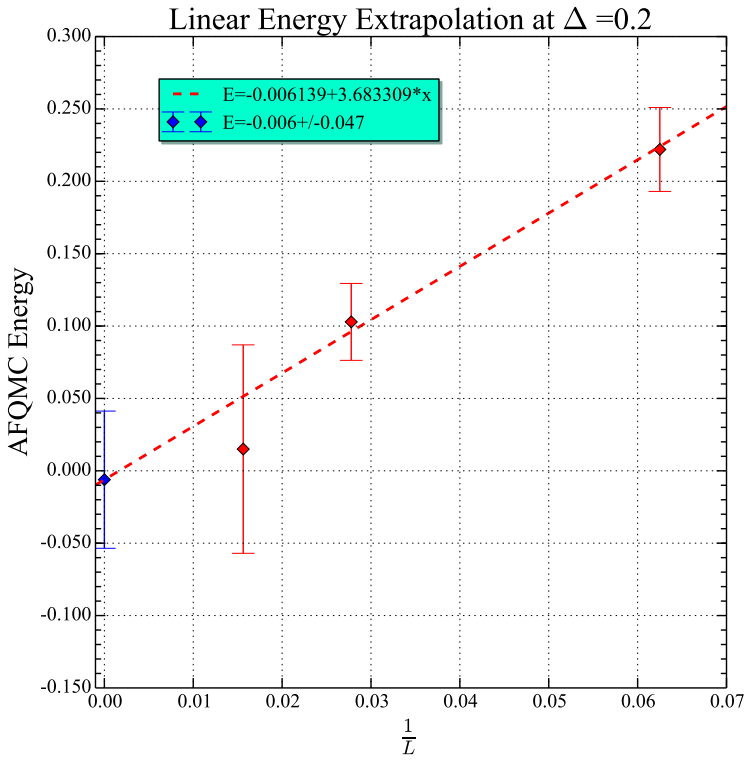

Figure 4.11: Charge gap extrapolation for the three-band Hubbard Kanamori model at $\Delta = 0.2$, $t = 1$, $U = 6$, $U_1 = U - 2J$, $U_2 = U - 3J$, and $J = 0.15U$ with an electron density of 4/3. 4×4, 6×6 and 8×8 lattices are used for extrapolation. L denotes the total number of sites. The charge decomposition and GHF trial/initial wave functions are used in the AFQMC calculations.

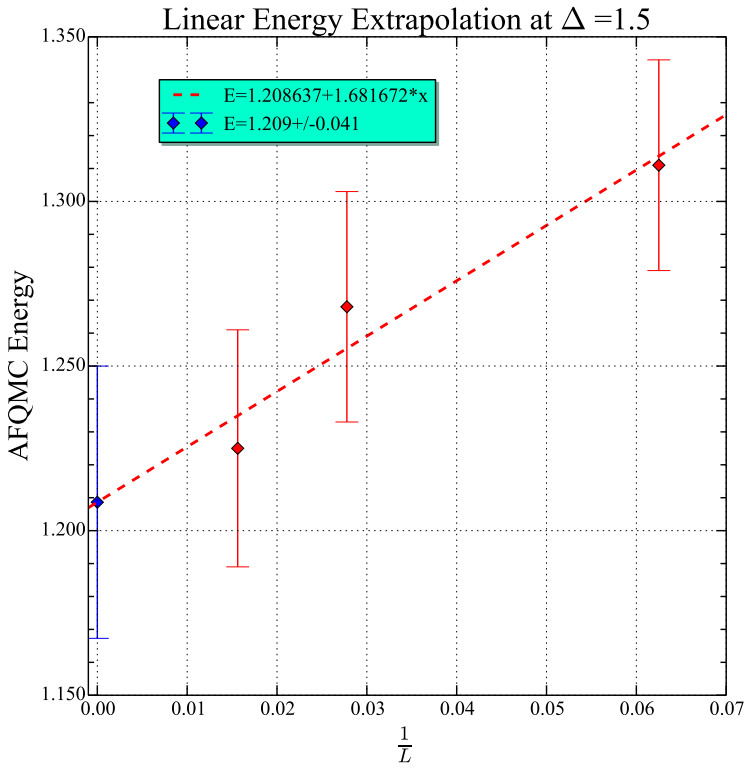

Figure 4.12: Charge gap extrapolation for the three-band Hubbard Kanamori model at $\Delta = 1.5$, $t = 1$, $U = 6$, $U_1 = U - 2J$, $U_2 = U - 3J$, and $J = 0.15U$ with an electron density of 4/3. 4×4, 6×6 and 8×8 lattices are used for extrapolation. The charge decomposition and GHF trial/initial wave functions are used within AFQMC calculations.

Chapter Five

Metal-Insulator and Magnetic Phase Transitions Study of Ca_2RuO_4 in the Zero-Temperature Limit

5.1 Introduction

Ever since the discovery of superconductivity within Sr_2RuO_4 [133], the first non-cuprate perovskite superconductor, the layered perovskite ruthenium oxides have been the subject of intense scrutiny. These explorations have revealed that ruthenium oxides, including the $Sr_{n+1}Ru_nO_{3n+1}$ and $Ca_{n+1}Ru_nO_{3n+1}$ series and mixtures thereof, exhibit a wide array of phases and exotic physical properties, including a variety of magnetic phases [19, 151], unconventional superconductivity [133], metal-insulator transitions (MIT) [150, 202], and unusual magnetoresistance [201]. It is believed that strong electron-electron interactions give rise to this diverse behavior and there are deep connections that can be made to the physics of the cuprates, which are isostructural with the ruthenates.

The compound Ca_2RuO_4 is one type of layered perovskite, which is a Mott insulator with antiferromagnetic (AFM) order at ambient pressure and temperatures below 112 K [15, 52, 151]. The insulating phase in Ca_2RuO_4, however, is suppressed upon increasing the temperature or pressure [150]: Ca_2RuO_4 is metallic at ambient pressure for temperatures above 357 K [6], and at room temperature for pressures above $\sim$0.5 GPa [150, 202]. At moderate pressures, Ca_2RuO_4 remains metallic down to 0 K [149]. Upon varying either the temperature or pressure, Ca_2RuO_4 also undergoes a structural transition, from a short c-axis layered perovskite (S-Pbca) to a long c-axis layered perovskite (L-Pbca) structure, which coincides with the MIT to the metallic phase. The lattice structure of Ca_2RuO_4 is therefore intimately tied to its phase behavior in a manner that is difficult to disentangle from experiments alone, making it a ripe target for computational analyses.

5.2 Methods

In this work, we study the phase diagram of Ca_2RuO_4 for various lattice structures in their ground states with the aim of understanding the link between Ca_2RuO_4's structure and phase behavior free of the complicating effects of temperature and pressure. We do so by means of Auxiliary Field Quantum Monte Carlo (AFQMC) and Dynamical Mean Field Theory (DMFT), two state-of-the-art electronic structure techniques especially capable of accurately treating many-electron correlation effects in realistic materials. Previous publications have studied the ground state properties of Ca_2RuO_4 using Density Functional Theory (DFT), in some case with $+U$ terms [9, 105], but such methods often struggle with handling the electron correlations. This work represents the first effort to apply AFQMC to realistic $4d$ materials as well as the first to obtain and compare DMFT and AFQMC phase diagrams of Ca_2RuO_4.

5.2.1 Model Hamiltonian

In order to represent Ca_2RuO_4, we generate a material-based, three-band Hubbard Hamiltonian from maximally localized Wannier functions (MLWF) using wannier90 [137, 200], which extracts the Fermi surface t_{2g}-derived bands. The electronic structure for a given lattice structure is calculated using the non-spin-polarized Generalized Gradient Approximation (GGA) [115, 116, 117, 118]. The projection from the DFT basis to the Wannier basis describing the t_{2g} manifold, together with the interaction parameters forms the model Hamiltonian. Our three-

band Hubbard-Kanamori Hamiltonian [80, 107] may be expressed as

$$\begin{aligned}\hat{H} = &\sum_{ij\nu\nu'\sigma} t_{ij}^{\nu\nu'} \hat{c}_{i\nu\sigma}^{\dagger} \hat{c}_{j\nu'\sigma} + U \sum_{i\nu} \hat{n}_{i\nu\uparrow} \hat{n}_{i\nu\downarrow} \\ &+ (U - 2J - J\delta_{\sigma\sigma'}) \sum\nolimits_{i,\nu\neq\nu',\sigma\sigma'} \hat{n}_{i\nu\sigma} \hat{n}_{i\nu'\sigma'} \\ &+ J \sum_{i,\nu\neq\nu'} (\hat{c}_{i\nu\uparrow}^{\dagger} \hat{c}_{i\nu'\downarrow}^{\dagger} \hat{c}_{i\nu\downarrow} \hat{c}_{i\nu'\uparrow} + \hat{c}_{i\nu\uparrow}^{\dagger} \hat{c}_{i\nu\downarrow}^{\dagger} \hat{c}_{i\nu'\downarrow} \hat{c}_{i\nu'\uparrow}).\end{aligned} \tag{5.1}$$

In the above, $\hat{c}_{i\nu\sigma}^{\dagger}$ creates an electron with spin σ in Wannier state ν at lattice site i and $\hat{n}_{i\nu\sigma}$ denotes the corresponding number operator. The first term of the Hamiltonian describes the hopping of electrons from site to site, the second describes intraorbital Coulomb repulsion, the third describes interorbital Coulomb repulsion, and the last contains electron pair-hopping and exchange contributions. Here, we set the direct and exchange screened Coulomb interaction parameters to $U = 2.3$ eV and $J = 0.35$ eV, respectively. These parameters were previously found to produce reliable representations of the properties and phase diagrams of perovskites including $CaRuO_3$, $SrRuO_3$, and $BaRuO_3$ [31, 33, 78]. The *ab initio* parameters $t_{ij}^{\nu\nu'}$ are hopping integrals that depend on the lattice structure. We use experimentally-determined atom positions as input structures (denoted by S/L for S-Pbca/L-Pbca structure) and study the phases of these structures at 295 K and ambient pressure (S-295K), 400 K at ambient pressure (L-400K) [15, 52], and room temperature at 1 GPa, 3 GPa, and 5 GPa of pressure [202] (L-1GPa, L-3GPa, and L-5GPa). Note that S-295K possesses an S-Pbca structure, while all of the other structures studied here possess an L-Pbca structure.

5.2.2 Auxiliary Field Quantum Monte Carlo

AFQMC is a quantum Monte Carlo technique with a long, successful history of treating Hubbard models [122, 239] that reconstructs a system's ground state wave function and related observables through an imaginary time projection that samples the space of non-orthogonal Slater determinants [235, 236]. AFQMC works directly at zero temperature and on finite systems, meaning that extrapolating to the thermodynamic limit is necessary for estimating bulk properties. In order to model Ca_2RuO_4 via the three-band Hubbard model described above, we employ the transforms, form of importance sampling, and phaseless approximation explicitly suited to handle three-band models detailed in Chapter 4. The techniques we used to determine the phases of Ca_2RuO_4 are detailed in the following.

5.2.2.1 Mapping the Ca_2RuO_4 Unit Cell to the HK Model

Ca_2RuO_4 is a layered perovskite with the *Pbc* space group [15, 52]. It is made of RuO_2 layers built from corner-sharing RuO_6 octahedra. The orbital and spin degrees of freedom of Ca_2RuO_4 fill 2/3 of a t_{2g}-manifold, which can be represented by a three-orbital HK model. As depicted in Figure 5.4, there are 4 Ru atoms in each unit cell, 2 within a top layer and 2 within a bottom layer. In the HK model, a Ca_2RuO_4 lattice with a 4×4×1 cell may thus be represented by 64 sites each containing 3 orbitals, leading to a total of 192 orbitals in AFQMC calculations. In the following study, we focus on the two-dimensional cell, which only contains two layers of Ru since the correlation between different layers is weak.

5.2.2.2 Antiferromagnetic Insulator State of the S-295K Structure

Below its Néel temperature of T_N=113 K, Ca_2RuO_4 is a Mott insulator that manifests AFM order [15]. We tested different trial wave functions and found that GHF wave functions not only accurately capture model energetics, but also naturally manifest the correct AFM spin order. In all subsequent calculation, we therefore built AFM order in the X direction (AFMX) for the top two Ru atoms and AFM order in the Y direction (AFMY) for the bottom two Ru atoms into our Generalized Hartree-Fock (GHF) wave functions (AFMXY). This results in complex trial wave functions, so we employ a charge decomposition on our positive J terms and constrain the phase problem in our simulations using the phaseless approximation.

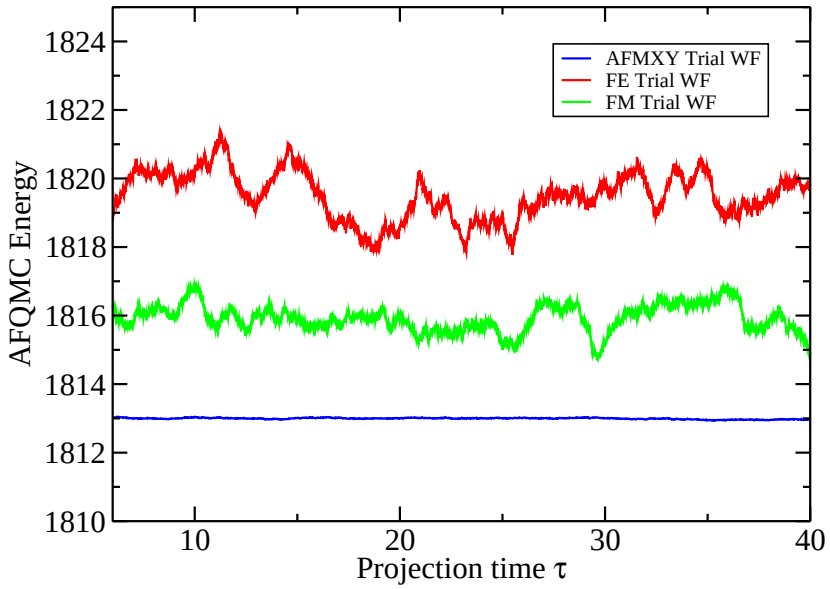

Figure 5.1: Ground state AFQMC energy obtained with different trial wave functions (Trial WF) for the 4x4x1, Ca_2RuO_4 model with the S-295K structure. The FE wave function is used as an initial wave function in call cases.

As an initial test, we compared our AFQMC results for a single $1 \times 1 \times 1$ unit cell to ED results. AFQMC simulations using an AFMXY trial wave function and a free electron (FE) initial wave function yielded a ground state energy of 113.484(2)

eV, which compares favorably with the ED result of 113.484257 eV. In comparison, AFQMC using AFMX-ordered trial wave functions in which AFM order in the X direction is imposed on all atoms yields an energy of 113.456(7) eV and AFQMC using AFMZ-ordered trial wave functions in which AFM order in the Z direction is imposed on all atoms yields an energy of 113.505(1) eV. AFMXY trial wave functions therefore yield the lowest AFQMC energies, which indicates that spin correlation between different layers is weak.

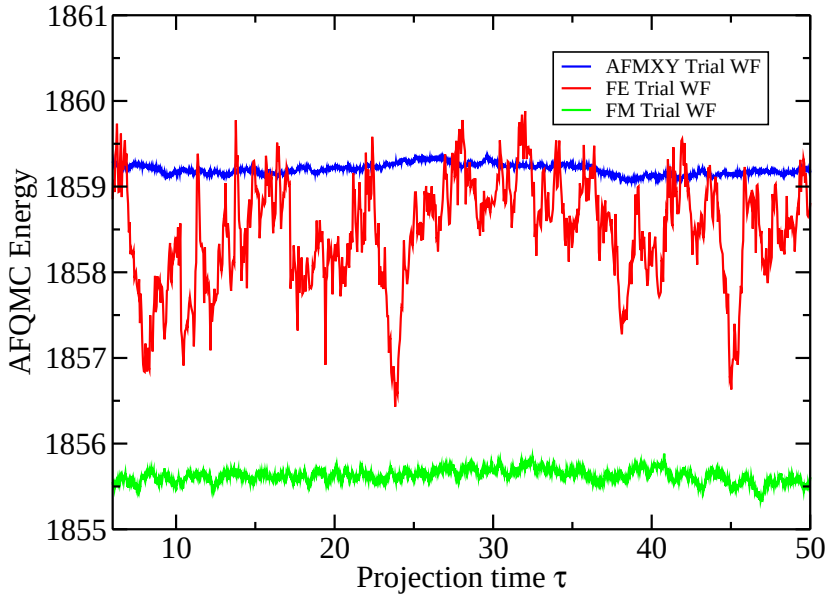

Figure 5.2: Ground state AFQMC energy obtained with different trial wave functions (Trial WF) for the 4x4x1, Ca_2RuO_4 model with the L-400K structure. The FE wave function is used as an initial wave function in call cases.

To determine the phases, various trial wave functions with different spin orders are imposed to obtain the AFQMC energy. The trial wave function that yields the lowest QMC energy is used to define the correct phase. For example, in Figure 5.1, calculations with free-electron, GHF with ferromagnetic (FM) order, and GHF with AFMXY order trial wave functions were performed and identified the AFMXY phase as the lowest energy phase based on the QMC energy procuded using the AFMXY trial wave function. Thus we concluded that the S-295K structure of Ca_2RuO_4

manifests AFM order. The determination that this phase is insulating is confirmed by the charge gap calculations that will be discussed later.

5.2.2.3 Ferromagnetic Metal State of the L-Pbca Structures

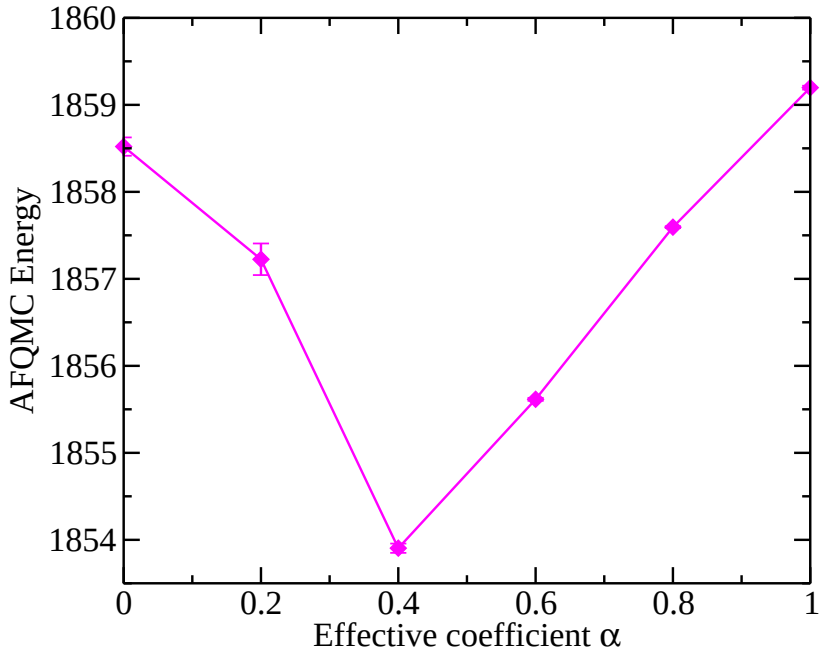

Figure 5.3: Ground state AFQMC energy obatined with various effective coefficients α that adjusts U/J (effective U/J, *i.e.*, $\alpha * U/J$, where $U = 2.3$, and $J = 0.35$) to generate trial wave functions for the 4x4x1, Ca_2RuO_4 model with the L-400K structure. The FE wave function is used as an initial wave function in call cases. Here the GHF solution at alpha = 0.2 is PM order. From this figure, we can determine that Ca_2RuO_4 with L-400K structure possesses FM order instead of PM order.

Similar calculations were conducted on the L-Pbca structures, and determined the correct phase for the different structures at high temperatures or pressures. For example, in the calculations performed on the L-400K structure shown in Figure 5.2, the AFQMC simulation finds that the trial wave function with FM order possesses the lowest QMC energy, which leads us to conclude that the L-400K structure has FM order. The sampling has the smallest energy fluctuation with FM order, which

is another sign that it captured the correct physics relative to the other trial wave functions.

Another way of tuning the quality of trial wave functions with FM order is to tune the effective coefficient α to adjust the effective U/J parameters (*i.e.*, $\alpha * U/J$) that are used to identify optimal GHF solutions. As illustrated in Figure 5.3, the lowest AFQMC energy was obtained by tuning effective U/J used in the GHF global minimum search. At the same time, the difference between FM order and PM order is determined by checking the magnetic order from both GHF calculations and AFQMC solutions.

5.2.3 Dynamical Mean Field Theory

DMFT works by self-consistently mapping a larger lattice model onto a smaller interacting impurity model embedded within a Fermi sea [59]. Since DMFT operates directly in the thermodynamic limit, but at finite temperature, an extrapolation to zero temperature must therefore be performed in order to acquire ground state information. The techniques used in this work are introduced in the following.

5.2.3.1 Simulation unit

Differing from the AFQMC calculations in which 4 Ru atoms are included in each unit cell, DMFT assumes the self-energy on each Ru site is symmetric under rotation of the octahedra following previous work [31, 33, 78], and therefore simplifies the impurity model to include a single Ru atom. This DMFT impurity model was solved using the hybridization expansion variant of Continuous-Time Quantum Monte Carlo

(CTQMC) [68, 114, 160] implemented in the Toolbox for Research on Interacting Quantum Systems (TRIQS) library [160, 188].

5.2.3.2 Antiferromagnetic Insulator State of the S-295K Structure

Since DMFT models our system using a single site impurity model, the assumption that the self-energy on the local axis between two nearest neighbour sites has AFM symmetry was made to study the AFM phase. Assume that site A and B are two nearest neighbour sites (for example, (0,0,0) and (0.5,0.5,0)), then we will have

$$S_A^\dagger \Sigma_{A,\sigma} S_A = S_B^\dagger \Sigma_{B,\overline{\sigma}} S_B, \tag{5.2}$$

where site A has the σ spin and site B has the opposite $\overline{\sigma}$ spin.

Two calculations at 60 K and 300 K were conducted repectively using the S-295K structure. It turns out that DMFT only shows AFM order at 60 K, which indicates the existence of a phase transition between 60 K and 300 K. The insulating phase may further be determined upon the orbital resolved spectral function at 60 K. This will be further discussed below.

5.2.3.3 Ferromagnetic Metal State of the L-Pbca Structures

In order to determine the metallic or insulating nature of the L-Pbca structures, orbital resolved spectral functions were calculated to see if there was a finite gap at the Fermi surface. The critical temperatue T_c at which a phase transition occurs was

estimated based on the mean field equation

$$m^2 = A\frac{H}{m} - B(T - T_c), \tag{5.3}$$

where m is magnetic moment, H is magnetic field strength, H/m is the inverse of magnetic susceptibility, and A, B are the coefficients. If we draw the plot m^2 vs $\frac{H}{m}$, we can see that when $T < T_c$, the intercept with y-axis is positive, and when $T > T_c$, the intercept with the y-axis is negative. Through this analysis we can directly estimate the T_c value by estimating where T crosses the y-axis.

However, in some instances for which it is hard for DMFT to reach sufficiently low temperatures, a simplified equation was employed:

$$\frac{H}{m} = \chi^{-1} = \frac{B}{A}\left(T - T_c\right), \tag{5.4}$$

where χ is the magnetic susceptibility. A plot of χ^{-1} vs T can be drawn and linearly extrpolated to estimate T_c at low temperatures using high temperature data.

5.3 Results and Discussion

With the parameterization and extrapolation techiniques in hand, we next turn to studying the structure-driven antiferromagnetic insulator (AFM-I) to ferromagnetic metal (FM-M) transition in Ca_2RuO_4 in the zero temperature limit. Upon distortion, Ca_2RuO_4's t_{2g}-manifold splits into non-degenerate states. The crystal-field splitting, $\Delta = \epsilon_{yz} - \epsilon_{xy}$, is generally larger in the S-Pbca structure than in L-Pbca structures. As can be seen from Table 5.1, for example, $\Delta = 0.23$ eV for the S-295K structure, while $\Delta = 0.10$ eV for the L-400K structure. As pressure is applied, the crystal-field

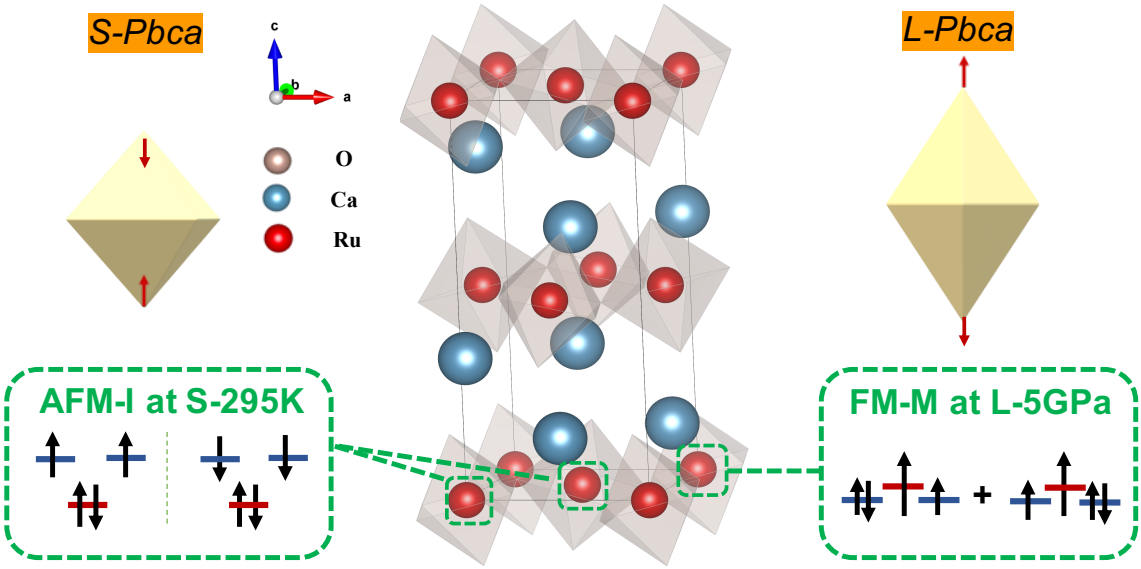

Figure 5.4: Crystal structure of Ca_2RuO_4. The primitive vectors $\vec{a}$, $\vec{b}$, and $\vec{c}$ are defined using orthorhombic notation. Calcium atoms are depicted in blue, oxygen atoms are depicted in grey, and ruthenium atoms are depicted in red. The lower left depicts the anti-ferromagnetic order found in this work at 295 K with a S-Pbca crystal structure where the xy band energy is lower than that of the yz and xz bands. The lower right depicts the ferromagnetic order found in this work at 5 GPa with an L-Pbca crystal structure in which the xy band energy is slightly higher than that of the yz and xz bands.

splitting decreases to $\Delta = 0.06$ eV for the L-1GPa structure and even a negative value of $\Delta = -0.02$ eV for the L-5GPa structure.

Table 5.1: The orbital spliting of the hopping matrix for various crystal structures.

	S-295K	L-400K	L-1GPa	L-3GPa	L-5GPa
xy	4.665	4.932	4.874	5.260	5.496
yz	4.893	5.029	4.930	5.271	5.478
xz	4.922	5.040	4.980	5.280	5.483
xy-yz	-0.228	-0.097	-0.056	-0.011	0.018
xz-yz	0.029	0.011	0.050	0.009	0.005

In the large splitting limit exhibited by the S-Pbca structure, the d_{xy} orbital is fully occupied and only two electrons occupy the d_{yz}/d_{xz} orbitals, which implies that S-Pbca physics can be described by a half-filled Hubbard model. Experiments demonstrate that Ca_2RuO_4 is an AFM-I with an S-Pbca structure at temperatures below 112 K [15, 52]. For the S-295K structure simulated in its ground state, both AFQMC and DMFT find AFM order within the d_{yz} and d_{xz} orbitals on nearest neighbor Ru atoms. This spin configuration is depicted on the left side of Figure 5.4. Since spontaneous symmetry breaking is not possible within a finite lattice, a spin-spin correlation function is calculated in AFQMC and indicates near full polarization (0.982(1)). We notice that the correlation function is negligible between different layers and only perform calculations on the two-dimensional layer (using up to a $4 \times 4 \times 1$ supercell) for simplification. DMFT calculations are conducted at 60 K and recover a fully polarized state and a very small imaginary self-energy, which indicates that the temperature employed was sufficiently small to yield 'ground state' quantities.

When the crystal-field splitting is small as for the L-Pbca structures, the t_{2g}-

manifold becomes partially filled, which can be described by a doped Hubbard model. Experimentally, Ca_2RuO_4 adopts an L-Pbca structure under moderate pressure and becomes a metal with FM order at temperatures below 10 K [149]. We find this same FM-M state for the L-5GPa structure in both AFQMC and DMFT simulations with the magnetic moment dominated by the spins on the d_{xy} orbital. Our speculation is that the d_{xy}-dominant FM-M state arises from the superposition of two degenerate states as shown on the right side of Figure 5.4. In order to determine the ground state magnetic order in AFQMC, we break the spin symmetry in the AFQMC trial wave function and compare the QMC energies of the different symmetry sectors. We find that the lowest energy state is indeed the d_{xy}-dominant FM-M state. To determine the order within DMFT, we apply an external magnetic field, H, and calculate the induced magnetization, m. Based on the mean field equation $m^2 = c_1 H/m - c_2(T - T_c)$, an extrapolation is made to determine the spontaneous magnetization. We find that a d_{xy}-dominant state also emerges at 60 K or below within DMFT.

In order to further examine the FM order underlying the L-5GPa structure, in Figure 5.6, we depict the magnetic moment distributions and orbital occupancies in the FM phase. DMFT calculations find 60% of the magnetic moment to be concentrated on the d_{xy} orbital, while AFQMC calculations find 68% with an uncertainty of 1.5%. Both algorithms agree that the FM order is dominated by spins on the d_{xy} orbital. We also checked the orbital-resolved density of state (DOS) from DFT and MLWF calculations of the L-5GPa structure. The d_{xy} orbital contribution to the DOS peaks closer to the Fermi level, while the d_{yz}/d_{xz} contributions peak further from it, a fact which explains the large moment on the d_{xy} orbital. The orbital occupancy is shifted by an average density of 4/3 in Figure 5.6(c). The density is slightly lower than average on the d_{xy} orbital and slightly higher than average on the d_{yz}/d_{xz} orbitals, which is caused by the negative crystal-field splitting. The

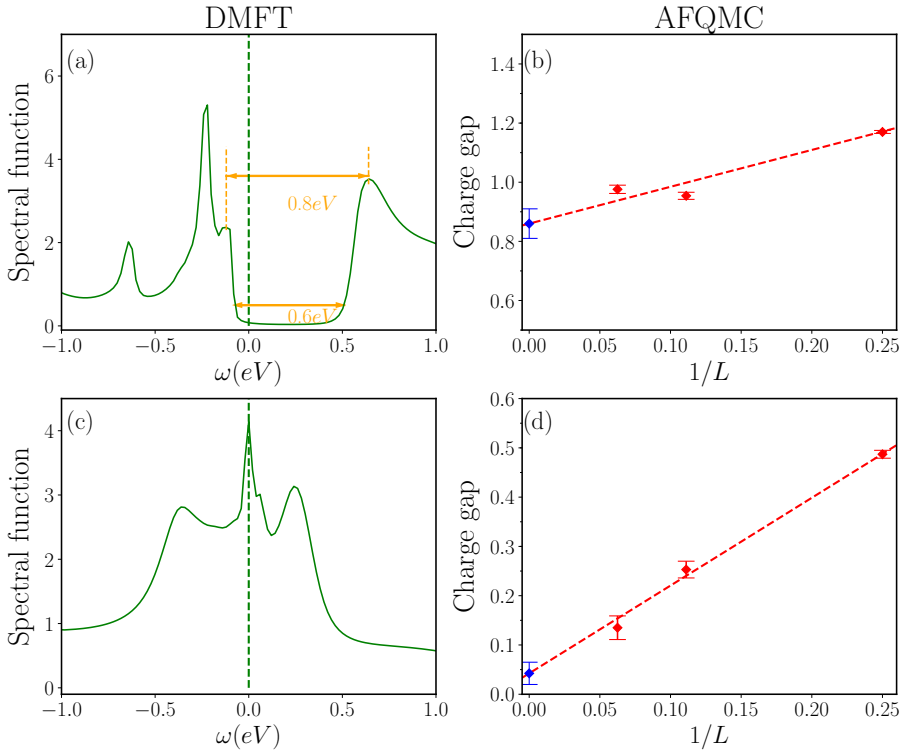

Figure 5.5: Comparison of the charge gap predictions from DMFT and AFQMC for the L-Pbca and S-Pbca structures. DMFT results are calculated at 60 K and AFQMC results are calculated at 0 K. (a) Spectral functions per Ru obtained using DMFT simulations with analytical continuation for the S-295K structure. (b) Extrapolation of the charge gap to the thermodynamic limit in AFQMC calculations of the S-295K structure. (c) Spectral functions per Ru obtained using DMFT simulations with analytical continuation for the L-5GPa structure. (d) Extrapolation of the charge gap to the thermodynamic limit in AFQMC calculations of the L-5GPa structure. In (b) and (d), the L on the x axis represents the number of unit cells used in the AFQMC simulations.

difference between the d_{xz} and d_{yz} occupancies is within the noise level in AFQMC, which indicates that the two methods give indeed more or less the same results.

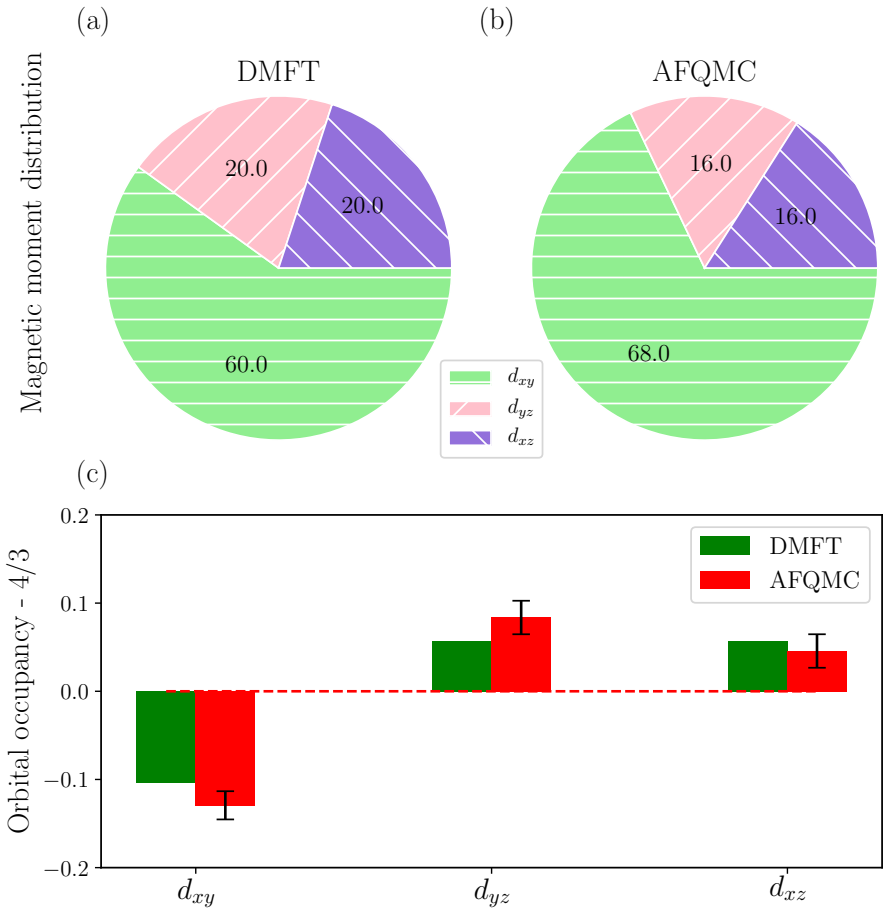

Figure 5.6: Comparison of magnetic moment distributions and orbital occupancies obtained by DMFT at 60 K and AFQMC at 0 K for the experimentally acquired L-Pbca L-5GPa structure. (a) Magnetic moment distributions from DMFT: 60% of the magnetic moment is in the d_{xy} band. (b) Magnetic moment distributions from AFQMC: 68% of the magnetic moment is in the d_{xy} band. (c) Orbital occupancies from DMFT and AFQMC: the y axis is shifted by an average density of 4/3. A smaller d_{xy} band occupancy results from a negative crystal-field splitting.

Having elucidated Ca_2RuO_4's magnetic order at low temperatures, we now turn to elucidating its insulating behavior. As mentioned in the Introduction, according to experiments, Ca_2RuO_4 is an insulator at temperatures below 357 K at ambient pressure and a metal at pressures above 0.5 GPa at ambient temperature [6, 150, 202]. To determine Ca_2RuO_4's insulating behavior, we examine its charge gap from DMFT

and AFQMC in Figure 5.5. The many-body spectral functions per Ru atom from DMFT plus analytical continuation are shown at 60 K for both the S-295K and L-5GPa structures. The S-295K structure exhibits a clear charge gap (∼0.6-0.8 eV), while the L-5GPa structure is gapless. For comparison, the charge gap was calculated in AFQMC using the formula $E_{N-1} + E_{N-1} - 2E_N$, *i.e.*, obtaining the lowest ground state energies for different numbers of particles, N, and calculating their difference. The charge gap was calculated for $2 \times 2 \times 1$, $3 \times 3 \times 1$, and $4 \times 4 \times 1$ supercells, and linear extrapolation was performed with respect to the inverse of the supercell size. A finite charge gap of 0.86 ± 0.05 eV was obtained for the S-295K structure, which confirmed its insulating character, whereas a charge gap of 0.01 ± 0.02 eV was obtained for the L-5GPa structure, which confirmed its metallic character. Note that the agreement in charge gaps we find between methods is only qualitative due to the methods' inherent approximations, including the influence of finite size effects in AFQMC and temperature in DMFT. From band structure calculations, the charge gap is an indirect gap. For a finite lattice, AFQMC is likely to overestimate a gap, while at finite temperatures, DMFT is likely to underestimate a gap. It was therefore expected that DMFT would yield a smaller charge gap than AFQMC.

The ground state phase diagram of Ca_2RuO_4 at various pressures is depicted in Figure 5.7. Both AFQMC and DMFT find the S-Pbca, S-295K structure to be an AFM-I, consistent with experimental findings [15, 52]. Both methods also find all of the L-Pbca structures studied, including the L-400K, L-1GPa, L-3GPa, and L-5GPa structures, to possess a metallic ground state and the L-5GPa structure to be in the FM-M state. Nevertheless, AFQMC and DMFT predict different magnetic properties for many of the L-Pbca structures. For the L-400K, L-1GPa, and L-3GPa structures, AFQMC predicts a FM-M state, while DMFT predicts a PM-M state. Interestingly, Ca_2RuO_4 was found to be in a mixed AFM-FM state at

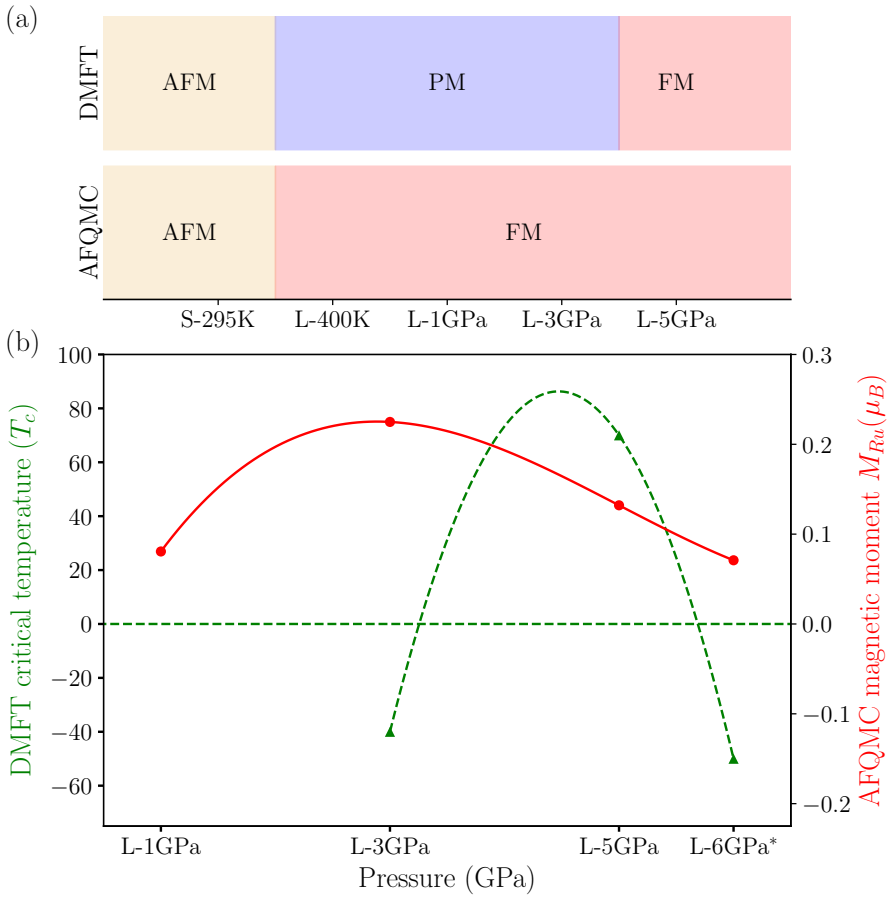

Figure 5.7: (a) Phase diagram of Ca_2RuO_4 for different lattice structures. Both DMFT and AFQMC predict the S-295K structure to be an AFM-I and the L-5GPa structure to be an FM-M. At intermediate pressures, both DMFT and AFQMC find Ca_2RuO_4 to be a metal, while DMFT predicts a PM-M and AFQMC predicts an FM-M state. (b) The red line depicts the ground state magnetic moments obtained using AFQMC as a function of pressure. The green line denotes the critical temperature obtained as a function of pressure with DMFT. Pressures at which there is no FM order are depicted as having negative critical temperatures. Note that the structure at $P = 6$ GPa shown in (b) is obtained by linear extrapolation of experimentally measured atom positions at $P = 1$ GPa and $P = 3$ GPa.

pressures smaller than 3 GPa [123]. The existence of a mixed state indicates small energy differences between the AFM and FM phases. While AFQMC remains able to successfully predict the experimentally observed magnetic order, this uncertainty may explain why DMFT struggles to do the same and instead predicts an unobserved PM phase. Above 5 GPa, experiments find FM order to be the most stable, in good agreement with our simulations. The critical temperature exhibits a non-monotonic behavior with pressure and peaks between 3-5 GPa in experiment [149]. We plot the critical temperature from DMFT as a function of pressure in Figure 5.7(b), which is dome-shaped with a peak around 5 GPa. We depict the critical temperature as being negative when DMFT does not recover a ferromagnetic state. To compare with DMFT results, we also determine the ground state magnetic moments as a function of pressure using AFQMC. The magnetic moments also exhibit a non-monotonic behavior, which indicates that FM order is favored at intermediate pressures. The maximum critical temperature is shifted to lower pressures in AFQMC, with AFQMC's peak instead occurring around 3 GPa.

5.4 Conclusions

In summary, we have employed two state-of-the-art electronic structure methods, AFQMC and DMFT, to elucidate the origins of the Ca_2RuO_4 phase diagram in the zero-temperature limit. We find that this material's magnetic and insulating transitions can overwhelmingly be explained by structural transitions between its S-Pbca and L-Pbca structures, which in turn influence the crystal-field splittings between and occupancies of its t_{2g} orbitals. Despite the different approximations and extrapolations used in the two theories described above, we find that both methods are in qualitative agreement regarding Ca_2RuO_4's structure-induced MIT. Both also

predict that the L-Pbca structure is accompanied by FM order dominated by the d_{xy} orbital at high pressures, while the S-Pbca structure is accompanied by AFM order dominated by the d_{xz} and d_{yz} orbitals at low pressures. Most importantly, despite their algorithmic limitations, our new multiband AFQMC methodology and DMFT only differ in their predictions of Ca_2RuO_4's magnetic ordering for L-Pbca structures at moderate pressures. For these structures, we find that AFQMC outperforms DMFT, correctly predicting the emergence of a ferromagnetic phase between ∼1-4 GPa also observed in experiment. Our work therefore paints a coherent picture of the microscopic, structural origins of Ca_2RuO_4's phase behavior, while also shedding light on the relative accuracy of AFQMC and DMFT for multiband materials.

Given our methods' conflicting results for Ca_2RuO_4's magnetic ordering between 1 and 5 GPa, high pressure diffraction studies that can eliminate any remaining ambiguity at these pressures would be particularly illuminating and enable methodologists to further improve their modeling techniques. The modeling employed here is also directly applicable to $Ca_{2-x}Sr_xRuO_4$ materials, strontium-doped versions of Ca_2RuO_4 that straddle the line between the zero-temperature Ca_2RuO_4, AFM-I studied here and the Sr_2RuO_4 superconductor [133]. Past works have shown that increasing x is analogous to increasing temperature or pressure in this work, leading to the evolution of a metal for large values of x [52, 152]. Nevertheless, $Ca_{2-x}Sr_xRuO_4$ exhibits a number of yet-to-be-explained exotic phases, including a metamagnetic phase that emerges for $0.2 < x < 0.5$ [152]. Beyond these specific applications, the methodologies employed here are quite general and ripe for application to the many 4- and $5d$ transition metal oxides whose complex interplay of spin-orbit coupling, exchange, and crystal-field effects have and continue to reveal unexpected physics. We look forward to the future use of these techniques to elucidate this perennially intriguing class of materials.

Chapter Six

Conclusions and Outlook

6.1 Overview

In this thesis, I have described several application-driven methodological developments for the ground state AFQMC algorithm, and their applications to weakly-bound, yet correlated molecules and strongly-correlated materials.

In Chapter 3, I demonstrated the power of AFQMC for capturing long-range, weak electron interactions. Dipole-bound anions are semi-stabilized by the long-range potential induced by the dipole moment of their corresponding neutral parent molecule. However, this interaction is challenging to model using traditional quantum chemistry theories. I demonstrated that QMC methods, here including DMC and AFQMC, can qualitatively describe this interaction, with the added advantage of predicting whether molecules can form dipole-bound anions in a cheaper way. Furthermore, I showed that energy differences can be efficiently obtained using a so-called correlated sampling scheme in which the auxiliary fields applied to two similar systems are kept the same to preserve similarities of the sampling paths between the two similar systems. These findings will enable more applications using stochastic methods to study much larger dipole-bound species, and shed light on more challenging systems like quadrupole-bound anions induced by much weaker long-range potentials.

In Chapter 4, I detailed a novel theoretical framework for treating the multi-band Hubbard Kanamori model using the AFQMC method. I discussed how to highly accurately capture Hund's physics by carefully combining discrete and continuous HS transformations, importance sampling that shifts the propagators, background subtraction, well-optimized trial wave functions that decrease the sampling variance, and the constrained path/phaseless approximations that control

the sign/phase problem. Illustrative results were presented for two-band and three-band toy models, for which impressive relative errors within 1% of the exact solution were achieved. These methodological development will provide more insights for researchers studying strongly correlated models and transition metal-containing materials, as well as for those seeking to develop more predictive many-body methods.

In Chapter 5, I presented one application of the Hubbard Kanamori scheme described in Chapter 4 to study $4d$ strongly-correlated real materials. I studied the low-temperature phase diagram of Ca_2RuO_4 for a range of layered perovskite structures at different temperatures and pressures. I determined the phase diagram by using trial wave functions with different spin orders, which helped me identify a metal-insulator transition driven by a structural transition from a long c-axis to a short c-axis perovskite accompanied by a ferromagnetic-antiferromagnetic transition. I determined the charge gap, orbital occupancy, and magnetic moment for each structure and showed that these values were consistent between AFQMC and DMFT. Our many-body simulations explain the electronic origin of the magnetic and metal-insulator transitions in Ca_2RuO_4, while also shedding light on the relative accuracy of AFQMC and DMFT. The success of studying the physics of $4d$ transition metal oxides at low temperatures using AFQMC enabled us to reach regions of the phase diagram that are extremely challenging to describe for DMFT.

6.2 Future Directions

In the future, I would like to continue the application-driven development of AFQMC.

A natural deeper exploration is the performance of correlated sampling AFQMC for treating larger systems. Currently, we only finished the benchmark study on small dipole-bound anions described here. The extension to much larger systems, like polycyclic aromatic hydrocarbons and long carbon-chains would be more appealing. Note that AFQMC is a wave function-based method that requires a reasonably accurate trial wave function to guarantee its accuracy. Assuming proper trial wave functions can be generated, there are many interesting weakly-bound molecules/clusters, such as solvated electron systems [199], that would also benefit from alternative theoretical treatments.

The methodologies developed for treating Hund's coupling are quite general and ripe for application to the many 4- and 5d transition metal oxides whose complex interplay of spin-orbit coupling, exchange, and crystal-field effects have and continue to reveal unexpected physics. Future explorations include but are not limited to negative J Hund's constant regions that few theoretical methods can describe, high-temperature superconductors, and a variety of transition metal oxides with Hund's physics. A key concern for this current algorithm is the lack of back-propagation to study the observables that do not commute with the Hamiltonian. Initial tests of back-propagation technique by Motta *et al* previously [147] showed poor performance on our Hubbard Kanamori model and require further investigation.

Besides employing models to study strongly-correlated solids popular in the condensed matter physics community, *ab initio* ways of studying heavy molecules containing lanthanide/actinide family elements with accurate treatment of significant spin-orbit coupling effects are desirable, have seen limited success so far. Explorations of such systems in AFQMC with favorable $O(N^3)$ scaling would substantially improve our understanding of the chemical properties of materials containing elements at the bottom of the periodic table.

Appendix A

Hubbard-Stratonovich Transformation of the *Ab Initio* Hamiltonian with Spin Symmetry

The most general *ab initio* Hamiltonian may be written as:

$$\begin{aligned}\hat{H} &= \hat{T} + \hat{V} \\ &= \sum_{\alpha} \sum_{ij}^{N} t_{ij}^{\alpha} \hat{c}_{i\alpha}^{\dagger} \hat{c}_{j\alpha} + \frac{1}{2} \sum_{\alpha,\beta} \sum_{i,j,k,l}^{N} V_{ijkl}^{\alpha\beta\beta\alpha} \hat{c}_{i\alpha}^{\dagger} \hat{c}_{j\beta}^{\dagger} \hat{c}_{k\beta} \hat{c}_{l\alpha}\end{aligned} \tag{A.1}$$

where N is the number of one-particle basis functions, α, β denotes the spin of the electron, and $\hat{c}_i^{\dagger}$ and $\hat{c}_i$ are the corresponding creation and annihilation operators for creating and destroying electrons in orbital i. The one-body matrix elements, t_{ij}^{α}, include all the one-body effects from the electron kinetic energy and the electron-nucleus interactions, while the two-body matrix elements, $V_{ijkl}^{\alpha\beta\beta\alpha}$, account for the electron-electron interactions.

Here the matrix elements can come from electron integrals expressed in terms of basis functions with spin symmetry, there would be no spin index in the Hamiltonian, which means:

$$t_{ij}^{\uparrow} = t_{ij}^{\downarrow}, \tag{A.2}$$

and

$$V_{ijkl}^{\uparrow\uparrow\uparrow\uparrow} = V_{ijkl}^{\downarrow\downarrow\downarrow\downarrow} = V_{ijkl}^{\uparrow\downarrow\downarrow\uparrow} = V_{ijkl}^{\downarrow\uparrow\uparrow\downarrow}. \tag{A.3}$$

The Hamiltonian can be simplified as:

$$\begin{aligned}
\hat{H} &= \hat{T} + \hat{V} \\
&= \sum_{\alpha} \sum_{ij}^{N} t_{ij} \hat{c}_{i\alpha}^{\dagger} \hat{c}_{j\alpha} + \frac{1}{2} \sum_{\alpha,\beta} \sum_{i,j,k,l}^{N} V_{ijkl} \hat{c}_{i\alpha}^{\dagger} \hat{c}_{j\beta}^{\dagger} \hat{c}_{k\beta} \hat{c}_{l\alpha} \\
&= \sum_{\alpha} \sum_{ij}^{N} t_{ij} \hat{c}_{i\alpha}^{\dagger} \hat{c}_{j\alpha} - \frac{1}{2} \sum_{\alpha,\beta} \sum_{i,j,k,l}^{N} V_{ijkl} \hat{c}_{i\alpha}^{\dagger} \hat{c}_{j\beta}^{\dagger} \hat{c}_{l\alpha} \hat{c}_{k\beta} \\
&= \sum_{\alpha} \sum_{ij}^{N} t_{ij} \hat{c}_{i\alpha}^{\dagger} \hat{c}_{j\alpha} - \frac{1}{2} \sum_{\alpha,\beta} \sum_{i,j,k,l}^{N} V_{ijkl} \hat{c}_{i\alpha}^{\dagger} (\delta_{jl}\delta_{\alpha\beta} - \hat{c}_{l\alpha} \hat{c}_{j\beta}^{\dagger}) \hat{c}_{k\beta} \\
&= \sum_{\alpha} \sum_{ij}^{N} t_{ij} \hat{c}_{i\alpha}^{\dagger} \hat{c}_{j\alpha} - \frac{1}{2} \sum_{\alpha} \sum_{i,j,k}^{N} V_{ijkj} \hat{c}_{i\alpha}^{\dagger} \hat{c}_{k\alpha} + \frac{1}{2} \sum_{\alpha,\beta} \sum_{i,j,k,l}^{N} V_{ijkl} \hat{c}_{i\alpha}^{\dagger} \hat{c}_{l\alpha} \hat{c}_{j\beta}^{\dagger} \hat{c}_{k\beta}
\end{aligned} \tag{A.4}$$

which can be further grouped into general one-body and two-body operators

$$\hat{H} = \hat{H}_1 + \hat{H}_2, \tag{A.5}$$

with

$$\hat{H}_1 = \sum_{\alpha} \sum_{ij}^{N} t_{ij} \hat{c}_{i\alpha}^{\dagger} \hat{c}_{j\alpha} - \frac{1}{2} \sum_{\alpha} \sum_{i,j,k}^{N} V_{ijkj} \hat{c}_{i\alpha}^{\dagger} \hat{c}_{k\alpha} = \sum_{\alpha} \sum_{ij} K_{ij} \hat{c}_{i\alpha}^{\dagger} \hat{c}_{j\alpha}, \tag{A.6}$$

and

$$\hat{H}_2 = \frac{1}{2} \sum_{\alpha,\beta} \sum_{i,j,k,l}^{N} V_{ijkl} \hat{c}_{i\alpha}^{\dagger} \hat{c}_{l\alpha} \hat{c}_{j\beta}^{\dagger} \hat{c}_{k\beta}. \tag{A.7}$$

To rewrite $\hat{H}_2$ as a sum of squares of one-body operators with the form

$$\hat{H}_2 = \frac{1}{2} \sum_{\gamma=1}^{N_\gamma} \lambda_\gamma \hat{v}_\gamma^2 \tag{A.8}$$

so that we can use the continuous Hubbard Stratonovich transformation $e^{-\Delta\tau \hat{A}^2/2} = \int dx \frac{1}{\sqrt{2\pi}} e^{-x^2/2} e^{x\sqrt{-\Delta\tau}\hat{A}}$, we recast V_{ijkl} in Equation A.7 in the form of a Hermitian

matrix by introducing the two combined indices $m = (i, l)$ and $n = (k, j)$: $\mathcal{V}_{mn} = \mathcal{V}_{(i,l),(k,j)} = V_{ijkl}$, with

$$\begin{aligned} \hat{a}_m &= \sum_{\alpha} \hat{c}^{\dagger}_{i\alpha} \hat{c}_{l\alpha} \\ \hat{a}_n &= \sum_{\beta} \hat{c}^{\dagger}_{j\beta} \hat{c}_{k\beta}. \end{aligned} \tag{A.9}$$

To realize this, one needs to make sure V_{ijkl} is Hermitian. With that in mind, we can prove that the way we grouped the indices m and n guarantees the Hermiticity

$$\begin{aligned} \mathcal{V}_{mn} &= \mathcal{V}_{(i,l),(k,j)} = V_{ijkl} \\ \mathcal{V}^{*}_{nm} &= \mathcal{V}_{(k,j),(i,l)} = V^{*}_{klij} = V_{ijkl}. \end{aligned} \tag{A.10}$$

With regrouping, the two-body operator becomes:

$$\hat{H}_2 = \sum_{mn} \mathcal{V}_{mn} \hat{a}_m \hat{a}_n. \tag{A.11}$$

There are a few ways to manipulate a general $\hat{H}_2$ into the form of Equation A.8.

1. One way is to diagonalize the Hermitian matrix $\mathcal{V}$ which can be written in the form of $\mathcal{V} = UDU^{\dagger}$, where U is a matrix whose columns are the eigenvectors of V and D is a diagonal matrix containing the corresponding eigenvalues D_γ. Here, we write out it in detail:

$$\mathcal{V}_{mn} = \sum_{\gamma} U_{m\gamma} D_\gamma U^{\dagger}_{\gamma n}, \tag{A.12}$$

and the two-body operator $\hat{H}_2$ can then be written as:

$$\begin{aligned}\hat{H}_2 &= \sum_{\gamma mn} U_{m\gamma}\hat{a}_m U^{\dagger}_{\gamma n}\hat{a}_n \\ &= \sum_{\gamma} D_\gamma \sum_m U_{m\gamma}\hat{a}_m \sum_n U^{\dagger}_{\gamma n}\hat{a}_n.\end{aligned} \tag{A.13}$$

For each eigenvalue D_γ, we assign

$$\hat{\rho}_\gamma = \sum_m U_{m\gamma}\hat{a}_m = \sum_{il\alpha} U^{\gamma}_{il}\hat{c}^{\dagger}_{i\alpha}\hat{c}_{l\alpha}. \tag{A.14}$$

Then, $\sum_n U^{\dagger}_{\gamma n}\hat{a}_n$ becomes

$$\sum_n U^{\dagger}_{\gamma n}\hat{a}_n = \sum_n U^{*}_{n\gamma}\hat{a}_n = \sum_{kj\beta} U^{\gamma *}_{kj}\hat{c}^{\dagger}_{j\beta}\hat{c}_{k\beta} = \sum_{kj\beta} U^{\gamma\dagger}_{jk}\hat{c}^{\dagger}_{j\beta}\hat{c}_{k\beta} = \hat{\rho}^{\dagger}_\gamma. \tag{A.15}$$

Looking further to the origin of $\hat{\rho}_\gamma$ and $\hat{\rho}^{\dagger}_\gamma$, consider the V_{ijkl} electron repulsion integrals, which may be expressed as

$$V_{ijkl} = \int d\vec{r}_1 d\vec{r}_2 \Psi^{*}_i(\vec{r}_1)\Psi_j(\vec{r}_1)\frac{1}{r_{12}}\Psi^{*}_k(\vec{r}_2)\Psi_l(\vec{r}_2). \tag{A.16}$$

If the wave function is real, these integrals have 8-fold symmetries,

$$V_{ijkl} = V_{lkji} = V_{klij} = V_{jilk} = V_{ijlk} = V_{klji} = V_{lkij} = V_{jikl}, \tag{A.17}$$

where the (i, j) indices for one electron can be freely changed to (j, i), and the same with the (k, l) indices. Then, we can easily prove that

$$\hat{\rho}^{\dagger}_\gamma = \sum_{il\alpha} U^{\gamma *}_{il}\hat{c}^{\dagger}_{l\alpha}\hat{c}_{i\alpha} = \sum_{il\alpha} U^{\gamma}_{li}\hat{c}^{\dagger}_{l\alpha}\hat{c}_{i\alpha} = \hat{\rho}_\gamma. \tag{A.18}$$

With this, we can easily write out that

$$\begin{aligned}\hat{H} &= \sum_{ij\alpha} K_{ij}\hat{c}^{\dagger}_{i\alpha}\hat{c}_{j\alpha} + \frac{1}{2}\sum_{\gamma} D_{\gamma}\hat{\rho}_{\gamma}\hat{\rho}^{\dagger}_{\gamma} \\ &= \sum_{ij\alpha} K_{ij}\hat{c}^{\dagger}_{i\alpha}\hat{c}_{j\alpha} + \frac{1}{2}\sum_{\gamma} D_{\gamma}\hat{\rho}^{2}_{\gamma}.\end{aligned} \tag{A.19}$$

Equation A.19 is the most popular formula we currently applied to quantum chemical problems. To use this, we have to guarantee that our Hamiltonian is Hermitian, and the orbitals/wave functions that generate the two-electron integrals are real.

However, this straightforward approach of diagonalizing the supermatrix $V_{m(i,l),n(k,j)}$ with dimensions N^2xN^2, where N is the number of molecular orbitals can exhibit potential computational and storage bottlenecks especially when applied to large systems. The direct diagonalization leads to a $O(N^6)$ scaling of computer time and $O(N^4)$ storage. The storage and transformation of two-electron integrals from the atomic orbital (AO) to the molecular orbital (MO) basis could also be a bottleneck.

2. The second way to recast $\hat{H}_2$ is to use the modified Cholesky decomposition. It was found that among all N^2 eigenvalues, only $O(N)$ eigenvalues have magnitudes greater than $\sim 10^{-8}E_h$ [163]. Modified Cholesky decomposition can iteratively find the necessary Cholesky vectors and substantially reduce the effort involved in two-electron integral manipulation.

   However, the regular Cholesky decomposition requires the matrix to be positive definite, when most of the two-electron integral matrix for quantum chemistry problems is only positively semidefinite. The decomposition of a positive semidefinite matrix does not have the stability of a procedure for strictly positive definite matrices, and the round off errors during the integral

calculations will increase with the dimension of the matrix.

Here, we write out the modified Cholesky decomposition method introduced in Reference [163] in a more detailed way.

The Cholesky representation of the two-electron integrals in the AO basis is given by

$$(\mu\nu|\lambda\sigma) \approx \sum_{J=1}^{N_{\mathrm{CD}}} L_{\mu\nu}^{J} L_{\lambda\sigma}^{J}, \tag{A.20}$$

where $L_{\mu\nu}^{J}$ is the decomposed Cholesky vectors, and N_{CD} is the number of Cholesky vectors. A single threshold parameter, δ, which determines the maximum error in the Cholesky-expanded supermatrix was employed to make sure that

$$\left|V_{pq} - V_{pq}^{N_{\mathrm{CD}}}\right| = \left|\Delta_{pq}^{N_{\mathrm{CD}}}\right| \leq \delta, \tag{A.21}$$

where $V_{pq}^{N_{\mathrm{CD}}}$ is the new Cholesky matrix, p is the (μ, ν) group, and q is the (λ, σ) group.

To iteratively obtain the Cholesky vectors, we first extract the diagonal elements $X = V_{pp} = (\mu\nu|\mu\nu)$. Based on the diagonal, we calculate the Cholesky vector at iteration J

$$L_{\mu\nu}^{J} = \left[\Delta_{[\lambda\sigma]_J,[\lambda\sigma]_J}^{(J-1)}\right]^{-1/2} \Delta_{\mu\nu,[\lambda\sigma]J}^{(J-1)}, \tag{A.22}$$

where $[\lambda\sigma]$ is the largest residual diagonal element at the $(J-1)th$ recursion. The residual matrix, $\Delta_{pq}^{N_{\mathrm{CD}}}$ is updated at Jth recursion

$$\Delta_{pq}^{N_{\mathrm{CD}}} = \Delta_{\mu\nu,\lambda\sigma}^{(J)} = (\mu v|\lambda\sigma) - \sum_{K=1}^{J} L_{\mu\nu}^{K} L_{\lambda\sigma}^{K} \tag{A.23}$$

until

$$\max_{\mu\nu}\left(\Delta_{\mu\nu,\mu\nu}^{N_{\mathrm{CD}}}\right) \leq \sqrt{\Delta_{\mu\nu,\mu\nu}^{(J)} \Delta_{\mu\nu,\mu\nu}^{(J)}} \leq \delta, \tag{A.24}$$

with the Cauchy-Schwarz inequality or the number of Cholesky vectors reaches the number of AO orbitals.

As we can see above, the prerequisite to use the Cholesky decomposition is that the V_{ijkl} have to be at least positive semidefinite, which may not be guaranteed for truncated or screened Hamiltonians. The Cholesky decomposition can dramatically reduce the computational and storage resources in AFQMC. Other relatively new techniques that further reduce the memory or computational resources such as interpolative separable density fitting and Hamiltonian symmetry considerations in AFQMC have been introduced in Reference [136, 148] and will not be discussed here.

Appendix B

Hubbard-Stratonovich Transformation of the *Ab Initio* Hamiltonian without Spin Symmetry

When spin symmetry is broken and there should be spin information contained in the *ab initio* Hamiltonian, which can be expressed as:

$$\begin{aligned}\hat{H} &= \hat{T} + \hat{V} \\ &= \sum_{\alpha\beta}\sum_{ij}^{N} t_{ij}^{\alpha\beta}\hat{c}_{i\alpha}^{\dagger}\hat{c}_{j\beta} + \frac{1}{2}\sum_{\alpha,\beta}\sum_{i,j,k,l}^{N} V_{ijkl}^{\alpha\beta\beta\alpha}\hat{c}_{i\alpha}^{\dagger}\hat{c}_{j\beta}^{\dagger}\hat{c}_{k\beta}\hat{c}_{l\alpha},\end{aligned} \tag{B.1}$$

where the $\hat{T}$ is the one-body electron kinetic energy and $\hat{V}$ is the two-body electron potential energy. To enable the Hubbard-Stratonovich (HS) transformation for the $\hat{V}$ term, it can be further reformulated as

$$\begin{aligned}\hat{V} &= \frac{1}{2}\sum_{\alpha,\beta}\sum_{i,j,k,l}^{N} V_{ijkl}^{\alpha\beta\beta\alpha}\hat{c}_{i\alpha}^{\dagger}\hat{c}_{j\beta}^{\dagger}\hat{c}_{k\beta}\hat{c}_{l\alpha} \\ &= -\frac{1}{2}\sum_{\alpha,\beta}\sum_{i,j,k,l}^{N} V_{ijkl}^{\alpha\beta\beta\alpha}\hat{c}_{i\alpha}^{\dagger}\hat{c}_{j\beta}^{\dagger}\hat{c}_{l\alpha}\hat{c}_{k\beta} \\ &= \frac{1}{2}\sum_{\alpha,\beta}\sum_{i,j,k,l}^{N} V_{ijkl}^{\alpha\beta\beta\alpha}\hat{c}_{i\alpha}^{\dagger}\hat{c}_{l\alpha}\hat{c}_{j\beta}^{\dagger}\hat{c}_{k\beta} - \frac{1}{2}\sum_{\alpha}\sum_{i,j}^{N}(\sum_{k}^{N} V_{ikkj}^{\alpha\alpha\alpha\alpha})\hat{c}_{i\alpha}^{\dagger}\hat{c}_{j\alpha} \\ &= \hat{H}_2 - \frac{1}{2}\sum_{\alpha}\sum_{i,j}^{N}(\sum_{k}^{N} V_{ikkj}^{\alpha\alpha\alpha\alpha})\hat{c}_{i\alpha}^{\dagger}\hat{c}_{j\alpha}.\end{aligned} \tag{B.2}$$

The second term in Equation B.2 is essentially a one-body operator which can be moved into the one-body operator. The final expression of the Hamiltonian becomes

$$\hat{H} = \hat{H}_1 + \hat{H}_2, \tag{B.3}$$

where

$$\hat{H}_1 = \sum_{\alpha,\beta}\sum_{ij}^{N} t_{ij}^{\alpha\beta}\hat{c}_{i\alpha}^{\dagger}\hat{c}_{j\beta} - \frac{1}{2}\sum_{\alpha}\sum_{i,j}^{N}(\sum_{k}^{N} V_{ikkj}^{\alpha\alpha\alpha\alpha})\hat{c}_{i\alpha}^{\dagger}\hat{c}_{j\alpha} = \sum_{\alpha,\beta}\sum_{ij}^{N} K_{ij}^{\alpha\beta}\hat{c}_{i\alpha}^{\dagger}\hat{c}_{j\beta} \tag{B.4}$$

and

$$\hat{H}_2 = \frac{1}{2}\sum_{\alpha,\beta}\sum_{i,j,k,l}^{N} V_{ijkl}^{\alpha\beta\beta\alpha}\hat{c}_{i\alpha}^{\dagger}\hat{c}_{l\alpha}\hat{c}_{j\beta}^{\dagger}\hat{c}_{k\beta}. \tag{B.5}$$

Following deductions similar to those presented in Appendix A using direct diagonalization, we can easily write out that

$$\begin{aligned}\hat{H} &= \sum_{ij\alpha} K_{ij}^{\alpha\beta}\hat{c}_{i\alpha}^{\dagger}\hat{c}_{j\beta} + \frac{1}{2}\sum_{\gamma} D_{\gamma}\hat{\rho}_{\gamma}\hat{\rho}_{\gamma}^{\dagger} \\ &= \sum_{ij\alpha} K_{ij}^{\alpha\beta}\hat{c}_{i\alpha}^{\dagger}\hat{c}_{j\beta} + \frac{1}{4}\sum_{\gamma} D_{\gamma}(\hat{\rho}_{\gamma}\hat{\rho}_{\gamma}^{\dagger} + \hat{\rho}_{\gamma}^{\dagger}\hat{\rho}_{\gamma}) \\ &= \sum_{ij\alpha} K_{ij}^{\alpha\beta}\hat{c}_{i\alpha}^{\dagger}\hat{c}_{j\beta} + \frac{1}{8}\sum_{\gamma} D_{\gamma}[(\hat{\rho}_{\gamma} + \hat{\rho}_{\gamma}^{\dagger})^2 - (\hat{\rho}_{\gamma} - \hat{\rho}_{\gamma}^{\dagger})^2]\end{aligned} \tag{B.6}$$

in the form of a square of one-body operators than can be further adapted for HS transformations.

Writing the Hamiltonian in this most general way and recasting the two-body supermatrix via direct diagonalization becomes necessary when studying heavy transition metal elements. In such cases, the wave functions may become complex that the 8-fold symmetry cannot be guaranteed. Spin-orbit coupling becomes significant which needs to be included. Truncation or reformulation of the basis could ease AFQMC sampling since it scales as $O(N^3)$ with the number of basis functions.

One example of the application of this formalism is to the study of actinide electronic structure and electrochemistry using AFQMC. The long-term storage and disposal of spent or wasted nuclear fuel present a major problem for the nuclear industry. Since the waste byproducts of the nuclear fuel cycle have radioactive half-lives of hundreds to thousands of years, it is important to understand how radioactive elements will interact with their environments if accidentally released.

For this purpose, the chemistry of uranium compounds is particularly important to understand and this is where accurate electronic structure simulations can provide key insights into transport properties and reaction barriers. Nevertheless, even the static electronic structure of compounds and materials comprised of f-shell elements, such as the lanthanides and actinides, remain computationally challenging to predict. These materials not only contain many strongly correlated electrons, but also manifest significant spin-orbit coupling (SOC), which complicate their modeling using conventional electronic structure methods. One potentially promising technique for handling such systems is AFQMC, which has been demonstrated to achieve chemical (kcal/mol) accuracy with a $O(N^3)$ computational cost. It's easier to include SOC using the current theoretical framework. This is ongoing research.

Appendix C

Generation of Generalized Hartree Fock Wave Functions for the Hubbard Kanamori Model

To find the best single determinant trial wave function, we use the Generalized Hartree Fock (GHF) method, which breaks spatial and spin symmetries. The GHF solution allows spin order in the x, y, and z directions, which can significantly reduce any constrained path approximation biases [122, 168]. The Hamiltonian used within our GHF calculations for this model is

$$\hat{H} = \hat{H}_t + \hat{H}_U + \hat{H}_{U_1} + \hat{H}_{U_2} + \hat{H}_J, \tag{C.1}$$

with

$$\hat{H}_t = \sum_{ij,\sigma\sigma'} t_{ij}^{\sigma\sigma'} \hat{c}_{i\sigma}^\dagger \hat{c}_{j\sigma'}, \tag{C.2}$$

$$\hat{H}_U = \sum_i [\, U^i \langle \hat{n}_{i\uparrow} \rangle \hat{n}_{i\downarrow} + U^i \hat{n}_{i\uparrow} \langle \hat{n}_{i\downarrow} \rangle, -U^i \langle \hat{c}_{i\uparrow}^\dagger \hat{c}_{i\downarrow} \rangle \hat{c}_{i\downarrow}^\dagger \hat{c}_{i\uparrow} - U^i \hat{c}_{i\uparrow}^\dagger \hat{c}_{i\downarrow} \langle \hat{c}_{i\downarrow}^\dagger \hat{c}_{i\uparrow} \rangle \,], \tag{C.3}$$

$$\begin{aligned} \hat{H}_{U_1} = \sum_{i<j} [\, & U_1^{ij} \hat{n}_{i\uparrow} \langle \hat{n}_{j\downarrow} \rangle + U_1^{ij} \langle \hat{n}_{i\uparrow} \rangle \hat{n}_{j\downarrow} - U_1^{ij} \langle \hat{c}_{i\uparrow}^\dagger \hat{c}_{j\downarrow} \rangle \hat{c}_{j\downarrow}^\dagger \hat{c}_{i\uparrow} - U_1^{ij} \hat{c}_{i\uparrow}^\dagger \hat{c}_{j\downarrow} \langle \hat{c}_{j\downarrow}^\dagger \hat{c}_{i\uparrow} \rangle \\ & + U_1^{ij} \hat{n}_{i\downarrow} \langle \hat{n}_{j\uparrow} \rangle + U_1^{ij} \langle \hat{n}_{i\downarrow} \rangle \hat{n}_{j\uparrow} - U_1^{ij} \langle \hat{c}_{i\downarrow}^\dagger \hat{c}_{j\uparrow} \rangle \hat{c}_{j\uparrow}^\dagger \hat{c}_{i\downarrow} - U_1^{ij} \hat{c}_{i\downarrow}^\dagger \hat{c}_{j\uparrow} \langle \hat{c}_{j\uparrow}^\dagger \hat{c}_{i\downarrow} \rangle \,], \end{aligned} \tag{C.4}$$

$$\begin{aligned} \hat{H}_{U_2} = \sum_{i<j} [\, & U_2^{ij} \hat{n}_{i\uparrow} \langle \hat{n}_{j\uparrow} \rangle + U_2^{ij} \langle \hat{n}_{i\uparrow} \rangle \hat{n}_{j\uparrow} - U_2^{ij} \hat{c}_{i\uparrow}^\dagger \hat{c}_{j\uparrow} \langle \hat{c}_{j\uparrow}^\dagger \hat{c}_{i\uparrow} \rangle - U_2^{ij} \langle \hat{c}_{i\uparrow}^\dagger \hat{c}_{j\uparrow} \rangle \hat{c}_{j\uparrow}^\dagger \hat{c}_{i\uparrow} \\ & + U_2^{ij} \hat{n}_{i\downarrow} \langle \hat{n}_{j\downarrow} \rangle + U_2^{ij} \langle \hat{n}_{i\downarrow} \rangle \hat{n}_{j\downarrow} - U_2^{ij} \hat{c}_{i\downarrow}^\dagger \hat{c}_{j\downarrow} \langle \hat{c}_{j\downarrow}^\dagger \hat{c}_{i\downarrow} \rangle - U_2^{ij} \langle \hat{c}_{i\downarrow}^\dagger \hat{c}_{j\downarrow} \rangle \hat{c}_{j\downarrow}^\dagger \hat{c}_{i\downarrow} \,], \end{aligned} \tag{C.5}$$

and

$$\begin{aligned}\hat{H}_J = \sum_{i<j} [\, & J^{ij}\hat{c}^\dagger_{i\uparrow}\hat{c}_{j\uparrow}\langle\hat{c}^\dagger_{j\downarrow}\hat{c}_{i\downarrow}\rangle + J^{ij}\langle\hat{c}^\dagger_{i\uparrow}\hat{c}_{j\uparrow}\rangle\hat{c}^\dagger_{j\downarrow}\hat{c}_{i\downarrow} - J^{ij}\hat{c}^\dagger_{i\uparrow}\hat{c}_{i\downarrow}\langle\hat{c}^\dagger_{j\downarrow}\hat{c}_{j\uparrow}\rangle - J^{ij}\langle\hat{c}^\dagger_{i\uparrow}\hat{c}_{i\downarrow}\rangle\hat{c}^\dagger_{j\downarrow}\hat{c}_{j\uparrow} \\ & + J^{ij}\hat{c}^\dagger_{i\uparrow}\hat{c}_{j\uparrow}\langle\hat{c}^\dagger_{i\downarrow}\hat{c}_{j\downarrow}\rangle + J^{ij}\langle\hat{c}^\dagger_{i\uparrow}\hat{c}_{j\uparrow}\rangle\hat{c}^\dagger_{i\downarrow}\hat{c}_{j\downarrow} - J^{ij}\hat{c}^\dagger_{i\uparrow}\hat{c}_{j\downarrow}\langle\hat{c}^\dagger_{i\downarrow}\hat{c}_{j\uparrow}\rangle - J^{ij}\langle\hat{c}^\dagger_{i\uparrow}\hat{c}_{j\downarrow}\rangle\hat{c}^\dagger_{i\downarrow}\hat{c}_{j\uparrow} \\ & + J^{ij}\hat{c}^\dagger_{j\uparrow}\hat{c}_{i\uparrow}\langle\hat{c}^\dagger_{i\downarrow}\hat{c}_{j\downarrow}\rangle + J^{ij}\langle\hat{c}^\dagger_{j\uparrow}\hat{c}_{i\uparrow}\rangle\hat{c}^\dagger_{i\downarrow}\hat{c}_{j\downarrow} - J^{ij}\hat{c}^\dagger_{j\uparrow}\hat{c}_{j\downarrow}\langle\hat{c}^\dagger_{i\downarrow}\hat{c}_{i\uparrow}\rangle - J^{ij}\langle\hat{c}^\dagger_{j\uparrow}\hat{c}_{j\downarrow}\rangle\hat{c}^\dagger_{i\downarrow}\hat{c}_{i\uparrow} \\ & + J^{ij}\hat{c}^\dagger_{j\uparrow}\hat{c}_{i\uparrow}\langle\hat{c}^\dagger_{j\downarrow}\hat{c}_{i\downarrow}\rangle + J^{ij}\langle\hat{c}^\dagger_{j\uparrow}\hat{c}_{i\uparrow}\rangle\hat{c}^\dagger_{j\downarrow}\hat{c}_{i\downarrow} - J^{ij}\hat{c}^\dagger_{j\uparrow}\hat{c}_{i\downarrow}\langle\hat{c}^\dagger_{j\downarrow}\hat{c}_{i\uparrow}\rangle - J^{ij}\langle\hat{c}^\dagger_{j\uparrow}\hat{c}_{i\downarrow}\rangle\hat{c}^\dagger_{j\downarrow}\hat{c}_{i\uparrow}\,]. \end{aligned} \tag{C.6}$$

Bibliography

[1] H. Abdoul-Carime and C. Desfrançois, *Electrons weakly bound to molecules by dipolar, quadrupolar or polarization forces*, Eur. Phys. J. D, 2 (1998), pp. 149–156.

[2] W. A. Al-Saidi, H. Krakauer, and S. Zhang, *Auxiliary-field quantum Monte Carlo study of first- and second-row post-d elements*, J. Chem. Phys., 125 (2006), p. 154110.

[3] W. A. Al-Saidi, H. Krakauer, and S. Zhang, *Auxiliary-field quantum Monte Carlo study of TiO and MnO molecules*, Phys. Rev. B, 73 (2006), p. 075103.

[4] W. A. Al-Saidi, H. Krakauer, and S. Zhang, *A study of H+H_2 and several H-bonded molecules by phaseless auxiliary-field quantum Monte Carlo with plane wave and Gaussian basis sets*, J. Chem. Phys., 126 (2007), p. 194105.

[5] W. A. Al-Saidi, S. Zhang, and H. Krakauer, *Auxiliary-field quantum Monte Carlo calculations of molecular systems with a Gaussian basis*, J. Chem. Phys., 124 (2006), p. 224101.

[6] C. S. Alexander, G. Cao, V. Dobrosavljevic, S. McCall, J. E. Crow, E. Lochner, and R. P. Guertin, *Destruction of the Mott insulating ground state of* Ca_2RuO_4 *by a structural transition*, Phys. Rev. B, 60 (1999), pp. R8422–R8425.

[7] J. B. Anderson, *A random-walk simulation of the Schrödinger equation:* H_3^+, J. Chem. Phys., 63 (1975), pp. 1499–1503.

[8] V. I. Anisimov, A. I. Poteryaev, M. A. Korotin, A. O. Anokhin, and G. Kotliar, *First-principles calculations of the electronic structure and spectra of strongly correlated systems: dynamical mean-field theory*, J. Phys.: Condens. Matter, 9 (1997), p. 7359.

[9] Anisimov, V. I., Nekrasov, I. A., Kondakov, D. E., Rice, T. M., and Sigrist, M., *Orbital-selective Mott-insulator transition in* $Ca_{2-x}Sr_xRuO_4$, Eur. Phys. J. B, 25 (2002), pp. 191–201.

[10] S. Ard, W. R. Garrett, R. N. Compton, L. Adamowicz, and S. G. Stepanian, *Rotational states of dipole-bound anions of hydrogen cyanide*, Chem. Phys. Lett., 473 (2009), pp. 223–226.

[11] R. N. Barnett, U. Landman, C. L. Cleveland, and J. Jortner, *Electron localization in water clusters. II. Surface and internal states*, J. Chem. Phys., 88 (1988), pp. 4429–4447.

[12] E. F. Belogolova, G. Liu, E. P. Doronina, S. M. Ciborowski, V. F. Sidorkin, and K. H. Bowen, *Dipole-bound anions of intramolecular complexes*, J. Phys. Chem. Lett, 9 (2018), pp. 1284–1289.

[13] E. Berg, S. Lederer, Y. Schattner, and S. Trebst, *Monte Carlo studies of quantum critical metals*, Annu. Rev. Condens. Matter Phys., 10 (2019), pp. 63–84.

[14] G. H. Booth, D. Cleland, A. Alavi, and D. P. Tew, *An explicitly correlated approach to basis set incompleteness in full configuration interaction quantum Monte Carlo*, J. Chem. Phys., 137 (2012), p. 164112.

[15] M. Braden, G. André, S. Nakatsuji, and Y. Maeno, *Crystal and magnetic structure of* Ca_2RuO_4 *: Magnetoelastic coupling and the metal-insulator transition*, Phys. Rev. B, 58 (1998), pp. 847–861.

[16] G. M. Buendia, *Comparative study of the discrete and the continuous Hubbard-Stratonovich transformation for a one-dimensional spinless fermion model*, Phys. Rev. B, 33 (1986), pp. 3519–3521.

[17] A. M. Buytendyk, A. M. Buonaugurio, S.-J. Xu, J. M. Nilles, K. H. Bowen, N. Kirnosov, and L. Adamowicz, *Computational and photoelectron spectroscopic study of the dipole-bound anions, indole*$(H_2O)^-_{1,2}$, J. Chem. Phys., 145 (2016), p. 024301.

[18] M. Calandra Buonaura and S. Sorella, *Numerical study of the two-dimensional Heisenberg model using a Green function Monte Carlo technique with a fixed number of walkers*, Phys. Rev. B, 57 (1998), pp. 11446–11456.

[19] G. Cao, S. McCall, J. Crow, and R. Guertin, *Observation of a metallic antiferromagnetic phase and metal to nonmetal transition in* $Ca_3Ru_2O_7$, Phys. Rev. Lett., 78 (1997), p. 1751.

[20] J. Carlson, S. Gandolfi, K. E. Schmidt, and S. Zhang, *Auxiliary-field quantum Monte Carlo method for strongly paired fermions*, Phys. Rev. A, 84 (2011), p. 061602.

[21] J. Carlson, J. E. Gubernatis, G. Ortiz, and S. Zhang, *Issues and observations on applications of the constrained-path Monte Carlo method to many-fermion systems*, Phys. Rev. B, 59 (1999), pp. 12788–12798.

[22] D. Ceperley, *The simulation of quantum systems with random walks: A new algorithm for charged systems*, J. Comput. Phys., 51 (1983), pp. 404 – 422.

[23] D. Ceperley, *Fermion nodes*, J. Stat. Phys., 63 (1991), p. 1237.

[24] T. Chachiyo and H. Chachiyo, *Understanding electron correlation energy through density functional theory*, arXiv:1811.00712, (2018).

[25] C.-C. Chang, B. M. Rubenstein, and M. A. Morales, *Auxiliary-field-based trial wave functions in quantum Monte Carlo calculations*, Phys. Rev. B, 94 (2016), p. 235144.

[26] C.-C. Chang and S. Zhang, *Spatially inhomogeneous phase in the two-dimensional repulsive Hubbard model*, Phys. Rev. B, 78 (2008), p. 165101.

[27] ——, *Spin and charge order in the doped hubbard model: Long-wavelength collective modes*, Phys. Rev. Lett., 104 (2010), p. 116402.

[28] R. Compton, F. Dunning, and P. Nordlander, *On the binding of electrons to CS_2: Possible role of quadrupole-bound states*, Chem. Phys. Lett., 253 (1996), pp. 8 – 12.

[29] R. N. Compton, H. S. C. Jr., C. Desfrançois, H. Abdoul-Carime, J. P. Schermann, J. H. Hendricks, S. A. Lyapustina, and K. H. Bowen, *On the binding of electrons to nitromethane: Dipole and valence bound anions*, J. Chem. Phys., 105 (1996), pp. 3472–3478.

[30] O. H. Crawford, *Bound states of a charged particle in a dipole field*, Proc. Phys. Soc., 91 (1967), p. 279.

[31] H. T. Dang and A. J. Millis, *Theory of ferromagnetism in vanadium-oxide based perovskites*, Phys. Rev. B, 87 (2013), p. 155127.

[32] H. T. Dang, J. Mravlje, A. Georges, and A. J. Millis, *Band structure and terahertz optical conductivity of transition metal oxides: Theory and application to* $CaRuO_3$, Phys. Rev. Lett., 115 (2015), p. 107003.

[33] ——, *Electronic correlations, magnetism, and Hund's rule coupling in the ruthenium perovskites $SrRuO_3$ and $CaRuO_3$*, Phys. Rev. B, 91 (2015), p. 195149.

[34] C. Desfrançois, *Determination of electron binding energies of ground-state dipole-bound molecular anions*, Phys. Rev. A, 51 (1995), pp. 3667–3675.

[35] C. Desfrançois, H. Abdoul-Carime, N. Khelifa, and J. P. Schermann, *From $\frac{1}{r}$ to $\frac{1}{r^2}$ potentials: Electron exchange between Rydberg atoms and polar molecules*, Phys. Rev. Lett., 73 (1994), pp. 2436–2439.

[36] C. Desfrançois, H. Abdoul-Carime, and J. P. Schermann, *Electron attachment to isolated nucleic acid bases*, J. Chem. Phys., 104 (1996), pp. 7792–7794.

[37] ——, *Ground state dipole-bound anions*, Int. J. Mod. Phys. B, 10 (1996), pp. 1339–1395.

[38] C. Desfrançois, S. Carles, and J. P. Schermann, *Weakly bound clusters of biological interest*, Chem. Rev., 100 (2000), pp. 3943–3962.

[39] C. Desfrançois, V. Périquet, Y. Bouteiller, and J. P. Schermann, *Valence and dipole binding of electrons to uracil*, J. Phys. Chem. A, 102 (1998), pp. 1274–1278.

[40] C. Desfrançois, V. Périquet, S. Carles, J. P. Schermann, and L. Adamowicz, *Neutral and negatively-charged formamide, N-methylformamide and dimethylformamide clusters*, Chem. Phys., 239 (1998), pp. 475 – 483.

[41] C. Desfrançois, V. Périquet, S. A. Lyapustina, T. P. Lippa, D. W. Robinson, K. H. Bowen, H. Nonaka, and R. N. Compton, *Electron binding to valence and multipole states of molecules: Nitrobenzene, para- and meta-dinitrobenzenes*, J. Chem. Phys., 111 (1999), pp. 4569–4576.

[42] C. E. H. Dessent, C. G. Bailey, and M. A. Johnson, *Dipole-bound excited states of the $I^-\cdot CH_3CN$ and $I^-\cdot(CH_3CN)_2$ ion-molecule complexes: Evidence for asymmetric solvation*, J. Chem. Phys., 103 (1995), pp. 2006–2015.

[43] N. D. Drummond and R. J. Needs, *Variance-minimization scheme for optimizing Jastrow factors*, Phys. Rev. B, 72 (2005), p. 085124.

[44] M. Dubecký, L. Mitas, and P. Jureçka, *Noncovalent interactions by quantum Monte Carlo*, Chem. Rev., 116 (2016), pp. 5188–5215.

[45] T. H. Dunning, *Gaussian basis sets for use in correlated molecular calculations. I. The atoms boron through neon and hydrogen*, J. Chem. Phys., 90 (1989), pp. 1007–1023.

[46] E. Fermi and E. Teller, *The capture of negative mesotrons in matter*, Phys. Rev., 72 (1947), pp. 399–408.

[47] C. Filippi and C. J. Umrigar, *Correlated sampling in quantum Monte Carlo: A route to forces*, Phys. Rev. B, 61 (2000), pp. R16291–R16294.

[48] C. Finch, R. Popple, P. Nordlander, and F. Dunning, *Formation of long-lived C_{60}^- ions in Rydberg atom-C_{60} collisions*, Chem. Phys. Lett., 244 (1995), pp. 345 – 349.

[49] R. C. Fortenberry and T. D. Crawford, *Theoretical prediction of new dipole-bound singlet states for anions of interstellar interest*, J. Chem. Phys., 134 (2011), p. 154304.

[50] W. M. C. Foulkes, L. Mitas, R. J. Needs, and G. Rajagopal, *Quantum Monte Carlo simulations of solids*, Rev. Mod. Phys., 73 (2001), pp. 33–83.

[51] E. Fradkin, S. A. Kivelson, M. J. Lawler, J. P. Eisenstein, and A. P. Mackenzie, *Nematic Fermi fluids in condensed matter physics*, Annu. Rev. Condens. Matter Phys., 1 (2010), pp. 153–178.

[52] O. Friedt, M. Braden, G. André, P. Adelmann, S. Nakatsuji, and Y. Maeno, *Structural and magnetic aspects of the metal-insulator transition in $Ca_{2-x}Sr_xRuO_4$*, Phys. Rev. B, 63 (2001), p. 174432.

[53] M. J. Frisch, M. Head-Gordon, and J. A. Pople, *A direct MP2 gradient method*, Chem. Phys. Lett., 166 (1990), pp. 275 – 280.

[54] ——, *Semi-direct algorithms for the MP2 energy and gradient*, Chem. Phys. Lett., 166 (1990), pp. 281 – 289.

[55] D. R. Garmer, *Extrapolation of the time-step bias in diffusion quantum Monte Carlo by a differential sampling technique*, J. Comput. Chem., 10, pp. 176–185.

[56] W. Garrett, *Critical binding of an electron to a non-stationary electric dipole*, Chem. Phys. Lett., 5 (1970), pp. 393 – 397.

[57] W. R. Garrett, *Critical binding of an electron to a rotationally excited dipolar system*, Phys. Rev. A, 3 (1971), pp. 961–972.

[58] W. R. Garrett, *Critical binding of electron-dipole rotor systems; electronically excited states*, J. Chem. Phys., 73 (1980), pp. 5721–5725.

[59] A. Georges, G. Kotliar, W. Krauth, and M. J. Rozenberg, *Dynamical mean-field theory of strongly correlated fermion systems and the limit of infinite dimensions*, Rev. Mod. Phys., 68 (1996), pp. 13–125.

[60] A. Georges, L. d. Medici, and J. Mravlje, *Strong correlations from Hund's coupling*, Annu. Rev. Condens. Matter Phys., 4 (2013), pp. 137–178.

[61] M. S. Gordon and M. W. Schmidt, *Chapter 41 - Advances in electronic structure theory: GAMESS a decade later*, in Theory and applications of computational chemistry, C. E. Dykstra, G. Frenking, K. S. Kim, and G. E. Scuseria, eds., Elsevier, Amsterdam, 2005, pp. 1167 – 1189.

[62] E. Gorelov, M. Karolak, T. O. Wehling, F. Lechermann, A. I. Lichtenstein, and E. Pavarini, *Nature of the Mott transition in* Ca_2RuO_4, Phys. Rev. Lett., 104 (2010), p. 226401.

[63] C. A. Gottlieb, T. C. Killian, P. Thaddeus, P. Botschwina, J. Flügge, and M. Oswald, *Structure of propadienylidene,* H_2CCC, J. Chem. Phys., 98 (1993), pp. 4478–4485.

[64] S. A. Grigera, R. S. Perry, A. J. Schofield, M. Chiao, S. R. Julian, G. G. Lonzarich, S. I. Ikeda, Y. Maeno, A. J. Millis, and A. P. Mackenzie, *Magnetic field-tuned quantum criticality in the metallic ruthenate* $Sr_3Ru_2O_7$, Science, 294 (2001), pp. 329–332.

[65] T. Gruber, K. Liao, T. Tsatsoulis, F. Hummel, and A. Grüneis, *Applying the coupled-cluster ansatz to solids and surfaces in the thermodynamic limit*, Phys. Rev. X, 8 (2018), p. 021043.

[66] J. Gubernatis, N. Kawashima, and P. Werner, *Quantum Monte Carlo methods: Algorithms for lattice models*, Cambridge University Press, 2016.

[67] J. Gukelberger, L. Huang, and P. Werner, *On the dangers of partial diagrammatic summations: Benchmarks for the two-dimensional Hubbard model in the weak-coupling regime*, Phys. Rev. B, 91 (2015), p. 235114.

[68] E. Gull, A. J. Millis, A. I. Lichtenstein, A. N. Rubtsov, M. Troyer, and P. Werner, *Continuous-time Monte Carlo methods for quantum impurity models*, Rev. Mod. Phys., 83 (2011), pp. 349–404.

[69] F. Güthe, M. Tulej, M. V. Pachkov, and J. P. Maier, *Photodetachment spectrum of l-$C_3H_2^-$: The role of dipole bound states for electron attachment in interstellar clouds*, ApJ, 555 (2001), p. 466.

[70] M. Gutowski, P. Skurski, A. I. Boldyrev, J. Simons, and K. D. Jordan, *Contribution of electron correlation to the stability of dipole-bound anionic states*, Phys. Rev. A, 54 (1996), pp. 1906–1909.

[71] M. Gutowski, P. Skurski, K. D. Jordan, and J. Simons, *Energies of dipole-bound anionic states*, Int. J. Quantum Chem, 64 (1997), pp. 183–191.

[72] G. L. Gutsev, P. Jena, and R. J. Bartlett, *Search for "quadrupole-bound" anions. I*, J. Chem. Phys., 111 (1999), pp. 504–511.

[73] G. L. Gutsev, M. Nooijen, and R. J. Bartlett, *Valence and excited dipole-bound states of polar diatomic anions: LiH^-, LiF^-, $LiCl^-$, NaH^-, NaF^-, $NaCl^-$, BeO^-, and MgO^-*, Chem. Phys. Lett., 276 (1997), pp. 13 – 19.

[74] G. L. Gutsev, A. L. Sobolewski, and L. Adamowicz, *A theoretical study on the structure of acetonitrile (CH_3CN) and its anion CH_3CN^-*, Chem. Phys., 196 (1995), pp. 1 – 11.

[75] N. I. Hammer, K. Diri, K. D. Jordan, C. Desfrançois, and R. N. Compton, *Dipole-bound anions of carbonyl, nitrile, and sulfoxide containing molecules*, J. Chem. Phys., 119 (2003), pp. 3650–3660.

[76] N. I. Hammer, R. J. Hinde, R. N. Compton, K. Diri, K. D. Jordan, D. Radisic, S. T. Stokes, and K. H. Bowen, *Dipole-bound anions of highly polar molecules: ethylene carbonate and vinylene carbonate*, J. Chem. Phys., 120 (2004), pp. 685–690.

[77] J. E. Han, M. Jarrell, and D. L. Cox, *Multiorbital Hubbard model in infinite dimensions: Quantum Monte Carlo calculation*, Phys. Rev. B, 58 (1998), pp. R4199–R4202.

[78] Q. Han, H. T. Dang, and A. J. Millis, *Ferromagnetism and correlation strength in cubic barium ruthenate in comparison to strontium and calcium ruthenate: A dynamical mean-field study*, Phys. Rev. B, 93 (2016), p. 155103.

[79] Q. Han and A. Millis, *Lattice energetics and correlation-driven metal-insulator transitions: The case of* Ca_2RuO_4, Phys. Rev. Lett., 121 (2018), p. 067601.

[80] H. Hao, B. M. Rubenstein, and H. Shi, *Auxiliary field quantum Monte Carlo for multiband Hubbard models: Controlling the sign and phase problems to capture Hund's physics*, Phys. Rev. B, 99 (2019), p. 235142.

[81] K. Haule and G. Kotliar, *Coherence–incoherence crossover in the normal state of iron oxypnictides and importance of Hund's rule coupling*, New J. Phys., 11 (2009), p. 025021.

[82] M. Head-Gordon, J. A. Pople, and M. J. Frisch, *MP2 energy evaluation by direct methods*, Chem. Phys. Lett., 153 (1988), pp. 503 – 506.

[83] W. Hehre, L. Radom, P. v. Schleyer, and J. Pople, *Ab initio molecular orbital theory*, John Wiley: New York, (1986).

[84] Held, K. and Vollhardt, D., *Microscopic conditions favoring itinerant ferromagnetism: Hund's rule coupling and orbital degeneracy**, Eur. Phys. J. B, 5 (1998), pp. 473–478.

[85] J. H. Hendricks, S. A. Lyapustina, H. L. de Clercq, and K. H. Bowen, *The dipole bound-to-covalent anion transformation in uracil*, J. Chem. Phys., 108 (1998), pp. 8–11.

[86] J. H. Hendricks, S. A. Lyapustina, H. L. de Clercq, J. T. Snodgrass, and K. H. Bowen, *Dipole bound, nucleic acid base anions studied via negative ion photoelectron spectroscopy*, J. Chem. Phys., 104 (1996), pp. 7788–7791.

[87] G. Hermann, V. Pohl, J. C. Tremblay, B. Paulus, H.-C. Hege, and A. Schild, *ORBKIT: A modular python toolbox for cross-platform postprocessing of quantum chemical wavefunction data*, J. Comput. Chem., 37, pp. 1511–1520.

[88] J. E. Hirsch, *Discrete Hubbard-Stratonovich transformation for fermion lattice models*, Phys. Rev. B, 28 (1983), pp. 4059–4061.

[89] ——, *Two-dimensional Hubbard model: Numerical simulation study*, Phys. Rev. B, 31 (1985), pp. 4403–4419.

[90] J. E. Hirsch and R. M. Fye, *Monte Carlo method for magnetic impurities in metals*, Phys. Rev. Lett., 56 (1986), pp. 2521–2524.

[91] P. Hoffman, *The man who only loved numbers: the story of Paul Erdös and the search for mathematical truth*, Hyperion, New York, 1998.

[92] P. Hohenberg and W. Kohn, *Inhomogeneous electron gas*, Phys. Rev., 136 (1964), p. B864.

[93] L. Hong-Tao, N. Chuan-Gang, H. Dao-Ling, and W. Lai-Sheng, *Vibrational spectroscopy of the dehydrogenated uracil radical by autodetachment of dipole-bound excited states of cold anions*, Angew. Chem. Int. Ed., 53, pp. 2464–2468.

[94] D.-L. Huang, H.-T. Liu, C.-G. Ning, and L.-S. Wang, *Vibrational state-selective autodetachment photoelectron spectroscopy from dipole-bound states of cold 2-hydroxyphenoxide: o-HO(C_6H_4)O^-*, J. Chem. Phys., 142 (2015), p. 124309.

[95] J. Hubbard, *Calculation of partition functions*, Phys. Rev. Lett., 3 (1959), pp. 77–78.

[96] J. Hubbard, *Electron correlations in narrow energy bands*, Proc. R. Soc. Lond. A, 276 (1963), pp. 238–257.

[97] W. Humphrey, A. Dalke, and K. Schulten, *VMD: Visual molecular dynamics*, J. Mol. Graphics, 14 (1996), pp. 33 – 38.

[98] S.-I. Ikeda, N. Shirakawa, H. Bando, and Y. Ootuka, *Orbital-degenerate paramagnetic metal Sr_2MoO_4: An electronic analogue to Sr_2RuO_4*, J. Phys. Soc. Jpn, 69 (2000), pp. 3162–3165.

[99] K. Inaba, A. Koga, S.-i. Suga, and N. Kawakami, *Finite-temperature Mott transitions in the multiorbital Hubbard model*, Phys. Rev. B, 72 (2005), p. 085112.

[100] S. Ishihara, M. Yamanaka, and N. Nagaosa, *Orbital liquid in perovskite transition-metal oxides*, Phys. Rev. B, 56 (1997), pp. 686–692.

[101] M. D. Johannes and I. I. Mazin, *Microscopic origin of magnetism and magnetic interactions in ferropnictides*, Phys. Rev. B, 79 (2009), p. 220510.

[102] K. D. Jordan and W. Luken, *Theoretical study of the binding of an electron to a molecular dipole: $LiCl^-$*, J. Chem. Phys., 64 (1976), pp. 2760–2766.

[103] K. D. Jordan and F. Wang, *Theory of dipole-bound anions*, Annu. Rev. Phys. Chem., 54 (2003), pp. 367–396.

[104] E. Josué Landinez Borda, J. A. Gomez, and M. A. Morales, *Non-orthogonal multi-slater determinant expansions in auxiliary field quantum Monte Carlo*, ArXiv e-prints, (2018).

[105] J. H. Jung, Z. Fang, J. P. He, Y. Kaneko, Y. Okimoto, and Y. Tokura, *Change of electronic structure in* Ca_2RuO_4 *induced by orbital ordering*, Phys. Rev. Lett., 91 (2003), p. 056403.

[106] Y. Kamihara, T. Watanabe, M. Hirano, and H. Hosono, *Iron-based layered superconductor $La[O_{1-x}F_x]FeAs$ (x= 0.05-0.12) with T_c= 26 K*, J. Am. Chem. Soc., 130 (2008), pp. 3296–3297.

[107] J. Kanamori, *Electron correlation and ferromagnetism of transition metals*, Prog. Theor. Phys., 30 (1963), pp. 275–289.

[108] R. A. Kendall, T. H. Dunning, and R. J. Harrison, *Electron affinities of the first-row atoms revisited. Systematic basis sets and wave functions*, J. Chem. Phys., 96 (1992), pp. 6796–6806.

[109] D. Khomskii and K. Kugel, *Orbital and magnetic structure of two-dimensional ferromagnets with Jahn-Teller ions*, Solid State Commun., 13 (1973), pp. 763 – 766.

[110] D. I. K. K.I. Kugel, *The Jahn-Teller effect and magnetism: Transition metal compounds*, SOV PHYS USPEKHI, 25 (1982), pp. 231 – 256.

[111] W. Kohn, *Electronic structure of matter–wave functions and density functionals*, Rev. Mod. Phys, 71 (1999), pp. 1253–1266.

[112] W. Kohn and L. J. Sham, *Self-consistent equations including exchange and correlation effects*, Phys. Rev., 140 (1965), p. A1133.

[113] G. Koster, L. Klein, W. Siemons, G. Rijnders, J. S. Dodge, C.-B. Eom, D. H. A. Blank, and M. R. Beasley, *Structure, physical properties, and applications of* $SrRuO_3$ *thin films*, Rev. Mod. Phys., 84 (2012), pp. 253–298.

[114] G. Kotliar, S. Y. Savrasov, K. Haule, V. S. Oudovenko, O. Parcollet, and C. A. Marianetti, *Electronic structure calculations with dynamical mean-field theory*, Rev. Mod. Phys., 78 (2006), pp. 865–951.

[115] G. Kresse and J. Furthmüller, *Efficiency of ab-initio total energy calculations for metals and semiconductors using a plane-wave basis set*, Comput. Mat. Sci., 6 (1996), p. 15.

[116] ——, *Efficient iterative schemes for ab initio total-energy calculations using a plane-wave basis set*, Phys. Rev. B, 54 (1996), pp. 11169–11186.

[117] G. Kresse and J. Hafner, *Ab initio molecular dynamics for liquid metals*, Phys. Rev. B, 47 (1993), pp. 558–561.

[118] G. Kresse and D. Joubert, *From ultrasoft pseudopotentials to the projector augmented-wave method*, Phys. Rev. B, 59 (1999), pp. 1758–1775.

[119] J. Kuneš, A. V. Lukoyanov, V. I. Anisimov, R. T. Scalettar, and W. E. Pickett, *Collapse of magnetic moment drives the Mott transition in MnO*, Nat. Mater., 7 (2008), p. 198. Article.

[120] M. S. Laad, L. Craco, and E. Müller-Hartmann, *Orbital-selective insulator-metal transition in* V_2O_3 *under external pressure*, Phys. Rev. B, 73 (2006), p. 045109.

[121] M. Larsson, W. D. Geppert, and G. Nyman, *Ion chemistry in space*, Rep. Prog. Phys., 75 (2012), p. 066901.

[122] J. P. F. LeBlanc, A. E. Antipov, F. Becca, I. W. Bulik, G. K.-L. Chan, C.-M. Chung, Y. Deng, M. Ferrero, T. M. Henderson, C. A. Jiménez-Hoyos, E. Kozik, X.-W. Liu, A. J. Millis, N. V. Prokof'ev, M. Qin, G. E. Scuseria, H. Shi, B. V. Svistunov, L. F. Tocchio, I. S. Tupitsyn, S. R. White, S. Zhang, B.-X. Zheng, Z. Zhu, and E. Gull, *Solutions of the two-dimensional Hubbard model: Benchmarks and results from a wide range of numerical algorithms*, Phys. Rev. X, 5 (2015), p. 041041.

[123] P. Lebre Alireza, S. Barakat, A.-M. Cumberlidge, G. Lonzarich, F. Nakamura, and Y. Maeno, *Developments on susceptibility and magnetization measurements under high hydrostatic pressure*, J. Phys. Soc. Jpn., 76 (2007), pp. 216–218.

[124] E. H. Lieb and F. Y. Wu, *Absence of Mott transition in an exact solution of the short-range, one-band model in one dimension*, Phys. Rev. Lett., 20 (1968), pp. 1445–1448.

[125] A. Liebsch and H. Ishida, *Subband filling and Mott transition in* $Ca_{2-x}Sr_xRuO_4$, Phys. Rev. Lett., 98 (2007), p. 216403.

[126] Y. Liu, M. Cho, and B. Rubenstein, *Ab Initio finite temperature auxiliary field quantum Monte Carlo*, J. Chem. Theory Comput., 14 (2018), pp. 4722–4732.

[127] E. Y. Loh, J. E. Gubernatis, R. T. Scalettar, S. R. White, D. J. Scalapino, and R. L. Sugar, *Sign problem in the numerical simulation of many-electron systems*, Phys. Rev. B, 41 (1990), pp. 9301–9307.

[128] P.-O. Löwdin, *Correlation problem in many-electron quantum mechanics I. Review of different approaches and discussion of some current ideas*, Adv. Chem. Phys., (1958), pp. 207–322.

[129] K. R. Lykke, R. D. Mead, and W. C. Lineberger, *Observation of dipole-bound states of negative ions*, Phys. Rev. Lett., 52 (1984), pp. 2221–2224.

[130] J. Lynn, I. Tews, S. Gandolfi, and A. Lovato, *Quantum Monte Carlo methods in nuclear physics: Recent advances*, arXiv:1901.04868, (2019).

[131] C. Lyon-Caen and M. Cyrot, *High-temperature expansion in the degenerate Hubbard model*, J. Phys. C: Solid State Phys., 8 (1975), p. 2091.

[132] A. P. Mackenzie and Y. Maeno, *The superconductivity of* Sr_2RuO_4 *and the physics of spin-triplet pairing*, Rev. Mod. Phys., 75 (2003), pp. 657–712.

[133] Y. Maeno, H. Hashimoto, K. Yoshida, S. Nishizaki, T. Fujita, J. Bednorz, and F. Lichtenberg, *Superconductivity in a layered perovskite without copper*, Nature, 372 (1994), p. 532.

[134] Y. Maeno, S. Nakatsuji, and S. Ikeda, *Metal-insulator transitions in layered ruthenates*, Mater. Sci. Eng., B, 63 (1999), pp. 70 – 75.

[135] J. P. Maier, G. A. H. Walker, D. A. Bohlender, F. J. Mazzotti, R. Raghunandan, J. Fulara, I. Garkusha, and A. Nagy, *Identification of* H_2CCC *as a diffuse interstellar band carrier*, ApJ, 726 (2011), p. 41.

[136] F. D. Malone, S. Zhang, and M. A. Morales, *Overcoming the memory bottleneck in auxiliary field quantum Monte Carlo simulations with interpolative separable density fitting*, J. Chem. Theory Comput., 15 (2019), pp. 256–264.

[137] N. Marzari and D. Vanderbilt, *Maximally localized generalized Wannier functions for composite energy bands*, Phys. Rev. B, 56 (1997), pp. 12847–12865.

[138] B. J. McCall, T. Oka, J. Thorburn, L. M. Hobbs, and D. G. York, *A critical examination of the l-*$C_3H_2^-$ *Spectrum and the diffuse interstellar bands*, ApJL, 567 (2002), p. L145.

[139] N. Metropolis and S. Ulam, *The Monte Carlo method*, J. Am. Stat. Assoc., 44 (1949), pp. 335–341.

[140] W. Metzner and D. Vollhardt, *Correlated lattice fermions in $d = \infty$ dimensions*, Phys. Rev. Lett., 62 (1989), pp. 324–327.

[141] C. Møller and M. S. Plesset, *Note on an approximation treatment for many-electron systems*, Phys. Rev., 46 (1934), pp. 618–622.

[142] K. Momma and F. Izumi, *VESTA3 for three-dimensional visualization of crystal, volumetric and morphology data*, J. Appl. Crystallogr., 44 (2011), pp. 1272–1276.

[143] M. A. Morales, J. McMinis, B. K. Clark, J. Kim, and G. E. Scuseria, *Multideterminant wave functions in quantum Monte Carlo*, J. Chem. Theory Comput., 8 (2012), pp. 2181–2188.

[144] Y. Motome and M. Imada, *A quantum Monte Carlo method and its applications to multi-orbital Hubbard models*, J. Phys. Soc. Jpn, 66 (1997), pp. 1872–1875.

[145] ——, *Numerical study for the ground state of multi-orbital Hubbard models*, J. Phys. Soc. Jpn, 67 (1998), pp. 3199–3215.

[146] M. Motta and S. Zhang, *Ab initio computations of molecular systems by the auxiliary-field quantum Monte Carlo method*, Wiley Interdisciplinary Reviews: Computational Molecular Science, 8, p. e1364.

[147] ——, *Computation of ground-state properties in molecular systems: Back-propagation with auxiliary-field quantum Monte Carlo*, J. Chem. Theory Comput., 13 (2017), pp. 5367–5378.

[148] M. Motta, S. Zhang, and G. K. Chan, *Hamiltonian symmetries in auxiliary-field quantum Monte Carlo calculations for electronic structure*, arXiv:1905.00511, (2019).

[149] F. Nakamura, *Pressure-induced Mott transition and related novel quantum phenomena in Ca_2RuO_4*, J. Phys. Soc. Jpn., 76 (2007), pp. 96–99.

[150] F. Nakamura, T. Goko, M. Ito, T. Fujita, S. Nakatsuji, H. Fukazawa, Y. Maeno, P. Alireza, D. Forsythe, and S. R. Julian, *From Mott insulator to ferromagnetic metal: A pressure study of* Ca_2RuO_4, Phys. Rev. B, 65 (2002), p. 220402.

[151] S. Nakatsuji, S.-i. Ikeda, and Y. Maeno, Ca_2RuO_4 : *New Mott insulators of layered ruthenate*, J. Phys. Soc. Jpn., 66 (1997), pp. 1868–1871.

[152] S. Nakatsuji and Y. Maeno, *Quasi-two-dimensional Mott transition system* $Ca_{2-x}Sr_xRuO_4$, Phys. Rev. Lett., 84 (2000), pp. 2666–2669.

[153] R. J. Needs, M. D. Towler, N. D. Drummond, and P. L. Ríos, *Continuum variational and diffusion quantum Monte Carlo calculations*, J. Phys.: Condens. Matter, 22 (2010), p. 023201.

[154] R. D. Nelson Jr, D. R. Lide Jr, and A. A. Maryott, *Selected values of electric dipole moments for molecules in the gas phase*, tech. rep., National Standard Reference Data System, 1967.

[155] E. Neuscamman, T. Yanai, and G. K.-L. Chan, *A review of canonical transformation theory*, Int. Rev. Phys. Chem., 29 (2010), pp. 231–271.

[156] Y. Nomura, S. Sakai, M. Capone, and R. Arita, *Unified understanding of superconductivity and Mott transition in alkali-doped fullerides from first principles*, Sci. Adv., 1 (2015).

[157] Y. Nomura, S. Sakai, M. Capone, and R. Arita, *Exotic s-wave superconductivity in alkali-doped fullerides*, J. Phys.: Condens. Matter, 28 (2016), p. 153001.

[158] M. Nooijen and R. J. Bartlett, *Equation of motion coupled cluster method for electron attachment*, J. Chem. Phys., 102 (1995), pp. 3629–3647.

[159] N. M. O'Boyle, A. L. Tenderholt, and K. M. Langner, *cclib: A library for package-independent computational chemistry algorithms*, J. Comput. Chem., 29, pp. 839–845.

[160] O. Parcollet, M. Ferrero, T. Ayral, H. Hafermann, I. Krivenko, L. Messio, and P. Seth, *TRIQS: A toolbox for research on interacting quantum systems*, Comput. Phys. Commun., 196 (2015), pp. 398 – 415.

[161] F. R. Petruzielo, J. Toulouse, and C. J. Umrigar, *Approaching chemical accuracy with quantum Monte Carlo*, J. Chem. Phys., 136 (2012), p. 124116.

[162] W. Purwanto, W. A. Al-Saidi, H. Krakauer, and S. Zhang, *Eliminating spin contamination in auxiliary-field quantum Monte Carlo: Realistic potential energy curve of F_2*, J. Chem. Phys., 128 (2008), p. 114309.

[163] W. Purwanto, H. Krakauer, Y. Virgus, and S. Zhang, *Assessing weak hydrogen binding on Ca^+ centers: An accurate many-body study with large basis sets*, J. Chem. Phys., 135 (2011), p. 164105.

[164] W. Purwanto and S. Zhang, *Quantum Monte Carlo method for the ground state of many-boson systems*, Phys. Rev. E, 70 (2004), p. 056702.

[165] ——, *Correlation effects in the ground state of trapped atomic Bose gases*, Phys. Rev. A, 72 (2005), p. 053610.

[166] W. Purwanto, S. Zhang, and H. Krakauer, *Excited state calculations using phaseless auxiliary-field quantum Monte Carlo: Potential energy curves of low-lying C_2 singlet states*, J. Chem. Phys., 130 (2009), p. 094107.

[167] W. Purwanto, S. Zhang, and H. Krakauer, *An auxiliary-field quantum Monte Carlo study of the chromium dimer*, J. Chem. Phys., 142 (2015), p. 064302.

[168] M. Qin, H. Shi, and S. Zhang, *Numerical results on the short-range spin correlation functions in the ground state of the two-dimensional Hubbard model*, Phys. Rev. B, 96 (2017), p. 075156.

[169] K. Raghavachari, G. W. Trucks, J. A. Pople, and M. Head-Gordon, *A fifth-order perturbation comparison of electron correlation theories*, Chem. Phys. Lett., 157 (1989), pp. 479 – 483.

[170] C. Riplinger and F. Neese, *An efficient and near linear scaling pair natural orbital based local coupled cluster method*, J. Chem. Phys., 138 (2013), p. 034106.

[171] N. Rom, D. Charutz, and D. Neuhauser, *Shifted-contour auxiliary-field Monte Carlo: Circumventing the sign difficulty for electronic-structure calculations*, Chem. Phys. Lett., 270 (1997), pp. 382 – 386.

[172] N. Rom, E. Fattal, A. K. Gupta, E. A. Carter, and D. Neuhauser, *Shifted-contour auxiliary-field Monte Carlo for molecular electronic structure*, J. Chem. Phys, 109 (1998), pp. 8241–8248.

[173] S. Rombouts, K. Heyde, and N. Jachowicz, *A discrete Hubbard-Stratonovich decomposition for general, fermionic two-body interactions*, Phys. Lett. A, 242 (1998), pp. 271 – 276.

[174] L. M. Roth, *Simple narrow-band model of ferromagnetism due to intra-atomic exchange*, Phys. Rev., 149 (1966), pp. 306–308.

[175] B. Rubenstein, *Introduction to the variational Monte Carlo method in quantum chemistry and physics*, in Variational methods in molecular modeling, J. Wu, ed., Molecular modeling and simulations (applications and perspectives), Springer, 2017.

[176] A. N. Rubtsov, V. V. Savkin, and A. I. Lichtenstein, *Continuous-time quantum Monte Carlo method for fermions*, Phys. Rev. B, 72 (2005), p. 035122.

[177] S. Saebo and J. Almöf, *Avoiding the integral storage bottleneck in LCAO calculations of electron correlation*, Chem. Phys. Lett., 154 (1989), pp. 83 – 89.

[178] M. Saitow, U. Becker, C. Riplinger, E. F. Valeev, and F. Neese, *A new near-linear scaling, efficient and accurate, open-shell domain-based local pair natural orbital coupled cluster singles and doubles theory*, J. Chem. Phys., 146 (2017), p. 164105.

[179] S. Sakai, R. Arita, and H. Aoki, *Numerical algorithm for the double-orbital Hubbard model: Hund-coupled pairing symmetry in the doped case*, Phys. Rev. B, 70 (2004), p. 172504.

[180] S. Sakai, R. Arita, K. Held, and H. Aoki, *Quantum Monte Carlo study for multiorbital systems with preserved spin and orbital rotational symmetries*, Phys. Rev. B, 74 (2006), p. 155102.

[181] C. Sarasola, J. E. Fowler, and J. M. Ugalde, *Critical conditions for stable dipole-bound dianions*, J. Chem. Phys., 110 (1999), pp. 11717–11719.

[182] P. J. Sarre, *The diffuse interstellar bands: A dipole-bound state hypothesis*, Mon. Not. R. Astron. Soc., 313 (2000), pp. L14–L16.

[183] P. J. Sarre, *The diffuse interstellar bands: A major problem in astronomical spectroscopy*, J. Mol. Spectrosc., 238 (2006), pp. 1 – 10.

[184] D. J. Scalapino, *Numerical studies of the 2D Hubbard model*, Springer New York, New York, NY, 2007, pp. 495–526.

[185] F. Schautz, F. Buda, and C. Filippi, *Excitations in photoactive molecules from quantum Monte Carlo*, J. Chem. Phys., 121 (2004), pp. 5836–5844.

[186] F. Schautz and C. Filippi, *Optimized Jastrow-Slater wave functions for ground and excited states: Application to the lowest states of ethene*, J. Chem. Phys., 120 (2004), pp. 10931–10941.

[187] M. W. Schmidt, K. K. Baldridge, J. A. Boatz, S. T. Elbert, M. S. Gordon, J. H. Jensen, S. Koseki, N. Matsunaga, K. A. Nguyen, S. Su, T. L. Windus, M. Dupuis, and J. A. Montgomery, *General atomic and molecular electronic structure system*, J. Comput. Chem., 14, pp. 1347–1363.

[188] P. Seth, I. Krivenko, M. Ferrero, and O. Parcollet, *TRIQS/CTHYB: A continuous-time quantum Monte Carlo hybridisation expansion solver for quantum impurity problems*, Comput. Phys. Commun., 200 (2016), pp. 274 – 284.

[189] J. Shee, B. Rudshteyn, E. J. Arthur, S. Zhang, D. R. Reichman, and R. A. Friesner, *On achieving high accuracy in quantum chemical calculations of 3d transition metal-containing systems: A comparison of auxiliary-field quantum Monte Carlo with coupled cluster, density functional theory, and experiment for diatomic molecules*, J. Chem. Theory Comput., 15 (2019), pp. 2346–2358.

[190] J. Shee, S. Zhang, D. R. Reichman, and R. A. Friesner, *Chemical transformations approaching chemical accuracy via correlated sampling in auxiliary-field quantum Monte Carlo*, J. Chem. Theory Comput., 13 (2017), pp. 2667–2680.

[191] H. Shi, S. Chiesa, and S. Zhang, *Ground-state properties of strongly interacting Fermi gases in two dimensions*, Phys. Rev. A, 92 (2015), p. 033603.

[192] H. Shi and S. Zhang, *Symmetry in auxiliary-field quantum Monte Carlo calculations*, Phys. Rev. B, 88 (2013), p. 125132.

[193] ——, *Many-body computations by stochastic sampling in Hartree-Fock-Bogoliubov space*, Phys. Rev. B, 95 (2017), p. 045144.

[194] Q. Si, R. Yu, and E. Abrahams, *High-temperature superconductivity in iron pnictides and chalcogenides*, Nat. Rev. Mater., 1 (2016), pp. 16017 EP –. Review Article.

[195] J. Simons, *Molecular anions*, J. Phys. Chem. A, 112 (2008), pp. 6401–6511.

[196] P. Skurski, M. Gutowski, and J. Simons, *Mixed valence/dipole-bound dianions*, J. Chem. Phys., 111 (1999), pp. 9469–9474.

[197] P. Skurski and J. Simons, *A dipole-bound dianion*, J. Chem. Phys., 112 (2000), pp. 6563–6570.

[198] T. Sommerfeld, K. M. Dreux, and R. Joshi, *Excess electrons bound to molecular systems with a vanishing dipole but large molecular quadrupole*, J. Phys. Chem. A, 118 (2014), pp. 7320–7329.

[199] T. Sommerfeld and K. D. Jordan, *Electron binding motifs of $(H2O)_n^-$ clusters*, J. Am. Chem. Soc., 128 (2006), pp. 5828–5833.

[200] I. Souza, N. Marzari, and D. Vanderbilt, *Maximally localized Wannier functions for entangled energy bands*, Phys. Rev. B, 65 (2001), p. 035109.

[201] C. Sow, S. Yonezawa, S. Kitamura, T. Oka, K. Kuroki, F. Nakamura, and Y. Maeno, *Current-induced strong diamagnetism in the Mott insulator Ca_2RuO_4*, Science, 358 (2017), pp. 1084–1087.

[202] P. Steffens, O. Friedt, P. Alireza, W. G. Marshall, W. Schmidt, F. Nakamura, S. Nakatsuji, Y. Maeno, R. Lengsdorf, M. M. Abd-Elmeguid, and M. Braden, *High-pressure diffraction studies on* Ca_2RuO_4, Phys. Rev. B, 72 (2005), p. 094104.

[203] M. Suewattana, W. Purwanto, S. Zhang, H. Krakauer, and E. J. Walter, *Phaseless auxiliary-field quantum Monte Carlo calculations with plane waves and pseudopotentials: Applications to atoms and molecules*, Phys. Rev. B, 75 (2007), p. 245123.

[204] S. Sugano, Y. Tanabe, and H. Kamimura, *Multiplets of transition-metal ions in crystals*, New York: Academic, 1970.

[205] L. Sun, X.-J. Chen, J. Guo, P. Gao, Q.-Z. Huang, H. Wang, M. Fang, X. Chen, G. Chen, Q. Wu, C. Zhang, D. Gu, X. Dong, L. Wang, K. Yang, A. Li, X. Dai, H.-k. Mao, and Z. Zhao, *Re-emerging superconductivity at 48 kelvin in iron chalcogenides*, Nature, 483 (2012), pp. 67 EP –.

[206] D. Sutter, C. G. Fatuzzo, S. Moser, M. Kim, R. Fittipaldi, A. Vecchione, V. Granata, Y. Sassa, F. Cossalter, G. Gatti, M. Grioni, H. M. Røznnow, N. C. Plumb, C. E. Matt, M. Shi, M. Hoesch, T. K. Kim, T.-R. Chang, H.-T. Jeng, C. Jozwiak, A. Bostwick, E. Rotenberg, A. Georges, T. Neupert, and J. Chang, *Hallmarks of Hunds coupling in the Mott insulator Ca_2RuO_4*, Nat. Commun., 8 (2017), p. 15176.

[207] M. Suzuki, *Relationship between d-dimensional quantal spin systems and (d+1)-dimensional Ising systems: Equivalence, critical exponents and systematic approximants of the partition function and spin correlations*, Prog. Theor. Phys., 56 (1976), pp. 1454–1469.

[208] A. Szabo and N. Ostlund, *Modern quantum chemistry: Introduction to advanced electronic structure theory*, Dover Books on Chemistry, Dover Publications, 1989.

[209] D. Thouless, *Stability conditions and nuclear rotations in the Hartree-Fock theory*, Nucl. Phys., 21 (1960), pp. 225 – 232.

[210] J. Toulouse, R. Assaraf, and C. J. Umrigar, *Chapter fifteen - Introduction to the variational and diffusion Monte Carlo methods*, in Electron correlation in molecules - ab initio beyond Gaussian quantum chemistry, P. E. Hoggan and T. Ozdogan, eds., vol. 73 of Advances in quantum chemistry, Academic Press, 2016, pp. 285 – 314.

[211] C. Traynor and J. Anderson, *Parallel Monte Carlo calculations to determine energy differences among similar molecular structures*, Chem. Phys. Lett., 147 (1988), pp. 389 – 394.

[212] H. F. Trotter, *On the product of semi-groups of operators*, Proc. Am. Math. Soc., 10 (1959), pp. 545–551.

[213] M. Tulej, D. A. Kirkwood, M. Pachkov, and J. P. Maier, *Gas-phase electronic transitions of carbon chain anions coinciding with diffuse interstellar bands*, ApJL, 506 (1998), p. L69.

[214] J. E. Turner, V. E. Anderson, and K. Fox, *Ground-state energy eigenvalues and eigenfunctions for an electron in an electric-dipole field*, Phys. Rev., 174 (1968), pp. 81–89.

[215] C. Umrigar, M. Nightingale, and K. Runge, *A diffusion Monte Carlo algorithm with very small time-step errors*, J. Chem. Phys., 99 (1993), pp. 2865–2890.

[216] M. Valiev, E. Bylaska, N. Govind, K. Kowalski, T. Straatsma, H. V. Dam, D. Wang, J. Nieplocha, E. Apra, T. Windus, and W. de Jong, *NWChem: A comprehensive and scalable open-source solution for large scale molecular simulations*, Comput. Phys. Commun., 181 (2010), pp. 1477 – 1489.

[217] Y. Virgus, W. Purwanto, H. Krakauer, and S. Zhang, *Stability, energetics, and magnetic states of cobalt adatoms on graphene*, Phys. Rev. Lett., 113 (2014), p. 175502.

[218] V. K. Voora, L. S. Cederbaum, and K. D. Jordan, *Existence of a correlation bound s-type anion state of C_{60}*, J. Phys. Chem. Lett, 4 (2013), pp. 849–853.

[219] V. K. Voora and K. D. Jordan, *Nonvalence correlation-bound anion states of polycyclic aromatic hydrocarbons*, J. Phys. Chem. Lett, 6 (2015), pp. 3994–3997.

[220] V. K. Voora, A. Kairalapova, T. Sommerfeld, and K. D. Jordan, *Theoretical approaches for treating non-valence correlation-bound anions*, J. Chem. Phys., 147 (2017), p. 214114.

[221] J. Vrbik, D. A. Legare, and S. M. Rothstein, *Infinitesimal differential diffusion quantum Monte Carlo: Diatomic molecular properties*, J. Chem. Phys., 92 (1990), pp. 1221–1227.

[222] F.-F. Wang, M. J. Deible, and K. D. Jordan, *Benchmark study of the interaction energy for an $(H_2O)_{16}$ cluster: Quantum Monte Carlo and complete basis set limit MP2 results*, J. Phys. Chem. A, 117 (2013), pp. 7606–7611.

[223] L.-S. Wang, C.-F. Ding, X.-B. Wang, and S. E. Barlow, *Photodetachment photoelectron spectroscopy of multiply charged anions using electrospray ionization*, Rev. Sci. Instrum., 70 (1999), pp. 1957–1966.

[224] T. Watanabe, H. Yanagi, T. Kamiya, Y. Kamihara, H. Hiramatsu, M. Hirano, and H. Hosono, *Nickel-based oxyphosphide superconductor with a layered crystal structure, LaNiOP*, Inorg. Chem., 46 (2007), pp. 7719–7721.

[225] P. Werner, E. Gull, M. Troyer, and A. J. Millis, *Spin freezing transition and non-Fermi-liquid self-energy in a three-orbital model*, Phys. Rev. Lett., 101 (2008), p. 166405.

[226] S. Wilson, *Electron correlation in molecules.*, Clarendon Press: Oxford, (1984).

[227] J. Xu and K. D. Jordan, *Application of the diffusion Monte Carlo method to the binding of excess electrons to water clusters*, J. Phys. Chem. A, 114 (2010), pp. 1364–1366.

[228] Y. Yao, J. Liu, C. Liu, W. Lu, C. Wang, and K. Ho, *Efficient and accurate treatment of electron correlations with Correlation Matrix Renormalization theory*, Sci. Rep., 5 (2015), p. 13478.

[229] D. Yarkony, *Modern electronic structure theory*, World Scientific: Singapore, 1995.

[230] Z. P. Yin, K. Haule, and G. Kotliar, *Kinetic frustration and the nature of the magnetic and paramagnetic states in iron pnictides and iron chalcogenides*, Nat. Mater., 10 (2011), pp. 932 EP –.

[231] K. Yokoyama, G. W. Leach, J. B. Kim, W. C. Lineberger, A. I. Boldyrev, and M. Gutowski, *Autodetachment spectroscopy and dynamics of vibrationally excited dipole-bound states of H_2CCC^-*, J. Chem. Phys., 105 (1996), pp. 10706–10718.

[232] A. Zen, J. G. Brandenburg, J. Klimeš, A. Tkatchenko, D. Alfè, and A. Michaelides, *Fast and accurate quantum Monte Carlo for molecular crystals*, Proc. Natl. Acad. Sci., (2018).

[233] S. Zhang, *Finite-temperature Monte Carlo calculations for systems with fermions*, Phys. Rev. Lett., 83 (1999), pp. 2777–2780.

[234] ——, *Theoretical methods for strongly correlated electron systems*, Springer-Verlag, 2003, ch. Quantum Monte Carlo Methods for Strongly Correlated Electron Systems.

[235] ——, *Auxiliary-field quantum Monte Carlo for correlated electron systems*, Verlag, 2013, ch. Emergent Phenomena in Correlated Matter: Modeling and Simulation.

[236] S. Zhang, J. Carlson, and J. E. Gubernatis, *Constrained path Monte Carlo method for fermion ground states*, Phys. Rev. B, 55 (1997), pp. 7464–7477.

[237] S. Zhang and H. Krakauer, *Quantum monte carlo method using phase-free random walks with slater determinants*, Phys. Rev. Lett., 90 (2003), p. 136401.

[238] Y. Zhang, P. M. Weber, and H. Jónsson, *Self-interaction corrected functional calculations of a dipole-bound molecular anion*, J. Phys. Chem. Lett, 7 (2016), pp. 2068–2073.

[239] B.-X. Zheng, C.-M. Chung, P. Corboz, G. Ehlers, M.-P. Qin, R. M. Noack, H. Shi, S. R. White, S. Zhang, and G. K.-L. Chan, *Stripe order in the underdoped region of the two-dimensional Hubbard model*, Science, 358 (2017), pp. 1155–1160.

[240] G.-Z. Zhu, Y. Liu, and L.-S. Wang, *Observation of excited quadrupole-bound states in cold anions*, Phys. Rev. Lett., 119 (2017), p. 023002.